UC Santa Barbara

UC Santa Barbara Electronic Theses and Dissertations

Title

Modelling Zika Virus Infections Using Human Stem Cell Derived Retinal Organoids

Permalink

https://escholarship.org/uc/item/96k526jn

Author

Proctor, Duncan

Publication Date

2024

Peer reviewed|Thesis/dissertation

eScholarship.org Powered by the California Digital Library
University of California

UNIVERSITY OF CALIFORNIA

Santa Barbara

Modelling Zika Virus Infections Using Human Stem Cell Derived Retinal Organoids

A dissertation submitted in partial satisfaction of the

requirements for the degree Doctor of Philosophy

in Molecular, Cellular and Developmental Biology

by

Duncan Alexander Proctor

Committee in charge:

Professor Dennis Clegg, Co-Chair

Carolina Arias, PhD, Chan Zuckerberg BioHub, Co-Chair

Professor Kathleen Foltz

Professor Stuart Feinstein

Diego Acosta-Alvear, PhD, Altos Labs

September 2024

The dissertation of Duncan Alexander Proctor is approved.

_____

Diego Acosta-Alvear

_____

Stuart Feinstein

_____

Kathleen Foltz

_____

Carolina Arias, Co-Chair

_____

Dennis Clegg, Co-Chair

April 2024

Modelling Zika Virus Infections Using Human Stem Cell Derived Retinal Organoids

Copyright © 2024

by

Duncan Alexander Proctor

ACKNOWLEDGEMENTS

This rollercoaster of a dissertation would not have been possible without the unmeasurable support of my family, friends, peers, and mentors. Foremost, I extend my sincerest appreciation to advisors Carolina Arias and Dennis Clegg for embarking on this journey and co-advising me. Their passion for science and curiosity-based research will remain a cornerstone for my career, wherever that journey will take me. Their collective patience and independent expertise provided the environment for this thesis to grow and blossom into what it is today.

I express my deepest gratitude to my thesis committee, Diego Acosta-Alvear, Stuart Feinstein, and Kathy Foltz, for their unwavering encouragement through all the challenges and successes in school and life during my tenure at UCSB. Their selflessness through their lives and career transitions is beyond anything I could have asked for.

My gratitude also extends to all my friends and lab mates in graduate school. As my thesis is the intersection between labs, I received more than one fantastic lab family. Thank you to the past and present members of the Clegg, Arias, and Acosta-Alvear labs. Your insight, expertise, and debates drove the maturation of this dissertation. I will be eternally grateful for the early morning coffee runs, for sneaking out in the afternoon for boba, and for the late-night talks discussing the meaning of the universe at the microscope. I acknowledge and appreciate the contributions of all individuals involved in this research endeavor. Thanks to

Zachary Aralis, whose contribution to all our single-cell RNA sequencing work is immeasurable. To Joseph Melgoza, thank you for all your help in establishing new immunohistology methods and for the passion that carried us through complex antigens. And to Vignesh Nadar, Mohamed Faynus, and Mika Katsura for training me in retinal organoid differentiation, your patience with my perpetual questions, and your generosity in providing organoids.

Special thanks go out to the myriad individuals whose contributions, though perhaps unseen, have left an indelible mark on this work. They extend to the faculty and staff in the Molecular Cellular and Developmental Biology department at UC Santa Barbara, who have shown immense empathy and care for everyone around them and whose dedication is integral to our successes. I want to thank Ben Lopez, the director of the NRI-MCDB Microscopy Facility, and the past and present directors of the Laboratory of Stem Cell Biology and Engineering, including Cassidy Arnold, Mika Katsura, and Susanne Meyer.

Lastly, I am profoundly grateful for all my family, friends, and loved ones from all stages of life who have supported me throughout this process. To my parents, words cannot express my appreciation for the love and compassion you extend to me daily. Without you, none of this would have been possible. To my brothers, William, Connor, and sister-in-law Svati: you've had my back through all the highs and lows. Spending time with you helped ground me, keep my perspective, and foster creativity outside the lab. I appreciate the encouragement from my grandma

Marilyn, who has been calling me “doctor” for months already. To those nearest and dearest to my heart, thank you for taking on the primary burden of the day-to-day challenges, being one of my biggest supporters, and for the love, patience, and tenderness that you have continually shown me.

This work is dedicated to the memory of my grandparents, Jennie, Pete, and Richard, whose belief in me was instrumental in my success.

Without the encouragement, love, and direction from the totality of my peers, mentors, family, and friends, I wouldn’t be the person or scientist that I am today.

Vita of Duncan Proctor

April 2024

Education

Bachelor of Arts in Biology, College of Creative Studies, University of California, Santa Barbara, June 2017

Doctor of Philosophy in Molecular, Cellular, and Developmental Biology, University of California, Santa Barbara, April 2024 (expected)

Publications and Manuscripts

Human Adipose Stem Cells Increase Growth Factor Release from Fibrin Clots. Siegal K, Clevenger T, Clegg D, Proctor D, Proctor C; 2018, *Journal of Arthroscopy*.

Digital quantification of neurite outgrowth and retraction by phase-contrast microscopy: A tau perspective. Cook B, Proctor D, Bromberg R, LaPointe N, Feinstein SC, Wilson L; 2017. Methods in Cell Biology, 217-228.

Differential Morphological and Biochemical Recovery from Chemotherapy Induced Peripheral Neuropathy Following Paclitaxel, Ixabepilone or Eribulin Treatment in Mouse Sciatic Nerves. Cook BM, Benbow SJ, Proctor DA, Wozniak KM, Slusher BS, Littlefield BA, Wilson L, Jordan MA, Feinstein SC; 2018, *Neurotoxicity Research*.

A Fast and Accessible Method for the Isolation of RNA, DNA, and Protein to Facilitate the Detection of SARS-CoV-2. Ponce-Rojas JC, Costello MS, Proctor DA, Kosik KS, Wilson MZ, Arias C, Acosta-Alvear D.; 2021, *Journal of Clinical Microbiology*.

CRISPR Interference Efficiently Silences Latent and Lytic Viral Genes in Kaposi's Sarcoma-Associated Herpesvirus-Infected Cells. Brackett K, Mungale A, Lopez-Isidro M, Proctor DA, Najarro G, Arias C.; 2021, *Viruses*.

Microcarrier-Based Culture of Human Pluripotent Stem-Cell-Derived Retinal Pigmented Epithelium. Faynus MA, Bailey JK, Pennington BO, Katsura M, Proctor DA, Yeh AK, Menon S, Choi DG, Lebkowski JS, Johnson LV, et al; 2022, *Bioengineering*.

Infection of Retinal Organoids Induces a Bystander Restriction Factors for Zika Virus that is not Conserved for HSV1. Proctor D, Aralis Z, Melgoza J, Faynus M, Katsura M, Nadar V, Dangerfield K, Clegg D, Arias C; *Manuscript in Preparation*

Awards, Grants, Fellowships

- Undergraduate Research and Creative Activities Grant, 2016
- Summer Undergraduate Research Fellowship, 2016
- Reagents Fellowship, 2017
- Wilcox Family Fellowship, 2023

Presentations

Mesenchymal Stem Cells and Bone Marrow Concentrate Proliferate and Synthesize Matrix on a Synthetic Scaffold. Proctor D, Hembrooke T, Saed-Nejad F, Ratcliffe A, Proctor C; Poster presentation at the Tissue Engineering and Regenerative Medicine Internatonal Society conference, Houston, 2011

Neurotoxic Mechanisms of Microtubule Targeting Agents: Implications for Chemotherapy Induced Peripheral Neuropathy. Proctor D, Cook B, Feinstein S; Poster presentation at the Undergraduate Research Colloquium, University of California, Santa Barbara, 2016

Rapid Morphological and Biochemical Recovery from Effects of Chemotherapy Microtubule Targeting Agents in Peripheral Neuropathy. Proctor D, Cook B, Feinstein S; College of Creative Studies, University of California, Santa Barbara, October 2016

Fibrin Clot Formation Highly Concentrates Platelets. Proctor D, Siegel K, Clegg D, Proctor C; Tissue Engineering and Regenerative Medicine International Society conference, San Diego, California, December 2016

Shedding Light on Ocular Zika Viral Infections. Duncan Proctor, Joseph Melgoza, Kyla Dangerfield, Vignesh Nadar, Dennis Clegg, Carolina Arias; Poster at the MCDB-BMSE Departmental Retreat, University of California Santa Barbara, Santa Barbara, California, October 2019

Impacts of Zika Virus on Retinal Development. Zach Aralis, Joseph Melgoza, Dennis O. Clegg, Carolina Arias; Lightning Talk Presentation for the MCDB-BMSE Departmental Retreat, University of California Santa Barbara, Santa Barbara, California, October 2020

Harnessing Retinal Organoids to Study Zika Virus in the Eye. Duncan Proctor, Zach Aralis, Joseph Melgoza, Dennis O. Clegg, Carolina Arias; Poster at the Organoids as Tools for Fundamental Discovery and Translation Keystone Symposia, Keystone, Colorado, April 2022

Field of Study

Major Fields: Virology and Stem Cell Biology

- Investigating wildebeest herd patterning in migration with Dr. Douglas McCauley, Department of Ecology, Evolution, and Marine Biology, University of California, Santa Barbara
- Investigating the effect of chemotherapeutics on nerves in multiple models with Dr. Brett Cook and Professor Stuart Feinstein, Department of Molecular, Cellular, and Developmental Biology, University of California, Santa Barbara
- Investigating Zika virus infection in stem cell derived retinal organoids and pigmented epithelium with Dr. Carolina Arias and Dr. Dennis Clegg Department of Molecular, Cellular, and Developmental Biology, University of California, Santa Barbara

Outreach

- Molecular Biology Techniques Outreach, South Coast Montessori Elementary School of Santa Barbara, May 2019
- CCS Alumni Biology Seminar Series (C-BASS) Inaugural Panel, November 25, 2020
- CCS Bio Colloquium Alumni Speaker – 2021, 2022

ABSTRACT

Modelling Zika Virus Infections Using Human Stem Cell Derived Retinal Organoids

by

Duncan Alexander Proctor

Zika virus (ZIKV), a mosquito-borne flavivirus, causes severe congenital eye disease. However, the molecular mechanisms underlying retinal pathologies are largely unknown in human modeling. This dissertation explores the mechanisms of viral pathogenesis in the retina using stem cell-derived retinal organoids (ROs) as a model for Zika virus (ZIKV) and other retinal-targeting herpes simplex virus 1 (HSV1) infections. Utilizing immature ROs, we elucidate specific impacts of early trimester ZIKV infections on retinal progenitor and ganglion cells, demonstrating significant disruptions to organoid growth and health. Our findings underscore the critical role of the AXL receptor in mediating retinal ZIKV infection, suggesting its potential as a therapeutic target. Conversely, modeling with mature ROs reveals the

rapid and destructive pathogenesis of HSV1, highlighting the vulnerability of photoreceptor and Müller glial cells to adult retinal necrotizing infections.

Further, through single-cell RNA sequencing (scRNA-seq), we reveal distinct cellular responses to ZIKV and HSV1, including unique gene expression patterns associated with cellular stress responses and interferon signaling. Specifically, our work details the modulation of the unfolded protein response (UPR) by ZIKV infection and identifies key pharmacological targets for inhibiting viral replication and enhancing cell viability. Additionally, we demonstrate the potent antiviral effects of interferon-alpha and beta in ZIKV-infected ROs, emphasizing the importance of bystander immune stimulation. Our findings provide a nuanced understanding of retinal viral infections, offering novel insights into the highly complex cellular and molecular underpinnings of ZIKV pathogenesis in the retina and underscoring the value of retinal organoids as a model system for studying infectious diseases.

TABLE OF CONTENTS

MODELLING ZIKA VIRUS INFECTIONS USING HUMAN STEM CELL DERIVED RETINAL ORGANOIDS I

ACKNOWLEDGEMENTS v

VITA OF DUNCAN PROCTOR VIII

ABSTRACT XI

TABLE OF CONTENTS XIII

CHAPTER 1. INTRODUCTION 1

I. Zika Virus Origin and Spread 1

II. Clinical Manifestations of ZIKV 4

III. Zika Virus Structure, Establishment, and Life Cycle 12

IV. The Retina 23

V. ZIKV Receptors: the TAM Family 42

VI. Neural Modeling of Zika Virus 46

VII. Single Cell RNA Sequencing 68

CHAPTER 2. HUMAN STEM CELL-DERIVED RETINAL ORGANOIDS RECAPITULATE ZIKA AND HSV1 PATHOPHYSIOLOGY 75

Summary 75

Introduction 75

Results 78

Discussion 85

Figures 92

CHAPTER 3. 5' AND 3' SINGLE CELL RNA SEQUENCING ILLUMINATES DIFFERENTIAL MECHANISMS BETWEEN ZIKA AND HSV1 INFECTIONS 107

Summary 107

Introduction *107*

Results *109*

Discussion *112*

Figures *118*

CHAPTER 4. MODULATION OF STRESS RESPONSE NETWORKS UNDERMINES ZIKA REPLICATION AND INFECTIONS IN RETINAL STEM CELL MODELING 123

Summary *123*

Introduction *123*

Results *130*

Discussion *135*

Figures *145*

CHAPTER 5. TYPE I INTERFERON ALPHA AND BETA AMELIORATE ZIKA INFECTIONS IN RETINAL ORGANOIDS 151

Summary *151*

Introduction *151*

Results *155*

Discussion *158*

Figures *166*

CHAPTER 6. CONCLUDING REMARKS 170

CHAPTER 7. MATERIALS AND METHODS 176

CITATIONS ..... **ERROR! BOOKMARK NOT DEFINED.**

Chapter 1. Introduction

I. Zika Virus Origin and Spread

Overview of Zika Virus

Zika virus (ZIKV) was initially isolated in Uganda in 1947, followed by the first documented human case in 1952, expanding through sporadic outbreaks in Asia and eventually into the Americas [1]. Although specific incidences suggest that ZIKV was present in the Americas before this point, ZIKV did not enter the world's spotlight until the ZIKV epidemic in the Americas started with the first official case of ZIKV congenital abnormalities in Northeastern Brazil in 2015 [2]. ZIKV can infect adults directly or infants from in-utero transmission. After transmission, the incubation period is 3-12 days (with the onset of half in the first seven days) [3]. Adult infections are primarily asymptomatic or cause non-specific symptoms, dubbed acquired Zika infections (AZI). For congenital cases, symptom severity increases dramatically the earlier into a pregnancy the mother is infected with ZIKV. Transmission to the baby is from in-utero vertical transmission from the mother, causing congenital malformations. The specific pattern of physical and neurological congenital malformations is termed congenital Zika syndrome (CZS) [4].

Transmission Vectors of Zika Virus

Historically, the primary vector for ZIKV was through the bites of carrier mosquitos, *Aedes aegypti* and *Aedes albopictus*, or from blood-to-blood transfer, as would occur by transfusions or transplants from infected individuals. Uniquely,

although less frequent than classic mechanisms, the American strains of ZIKV have expanded routes of infection, being the first flavivirus transmissible through sexual contact [5-7]. Modeling and clinical reporting support different potential infection routes as viral persistence is maintained in breast milk, urine, and saliva [5, 8]. Although the number of ZIKV cases remains low, the emergence of new transmission vectors and the expansion of tissue reservoirs in the American epidemic emphasize the need to study viral evolution before future large-scale outbreaks.

The Zika Virus Epidemic in the Americas

Although the first officially confirmed case in the Americas was in May 2015, phylogenetic studies suggest it was present in a few isolated cases extending back to 2011 [2, 8]. In 2015, infections skyrocketed in Brazil, rapidly expanding beyond Brazil and throughout the Americas, with cases in over 50 countries and territories [8]. Subsequently, there was a surge in ZIKV-related publications, from only 89 from 1952-2013, dramatically increasing to 12,020 from 2014-2023 (**Fig 1a**) [9]. A shift in ZIKV pathology and transmission vectors underlies the rapid expansion of ZIKV across Brazil, which quickly overtook that of other flaviviruses, surpassing the entire established range of Dengue (DENV). Other factors may be in play as, unlike DENV, which is somewhat restricted by low Northern population density in combination with climatic barriers in the South, ZIKV was transmitting in regions with a high density of a highly mobile, entirely naïve population compounded with increased infection from optimal conditions for mosquitos and the independent transmission routes and after the initial surge of 847,643 cases in the Americas

from 2015 to 2017, precipitating only 190,882 cases from 2018 to 2023 as the epidemic ramped down (**Fig 1b**) [8, 10]. This trend is similar for the United States (**Fig 1c**) and California (**Fig 1d**) [11, 12]. Although lower, the perseverance of case counts maintains a foothold for future outbreaks. That risk is increased as Aedes mosquito ranges expand away from the equator and into new population-dense regions with minimal immunity [13].

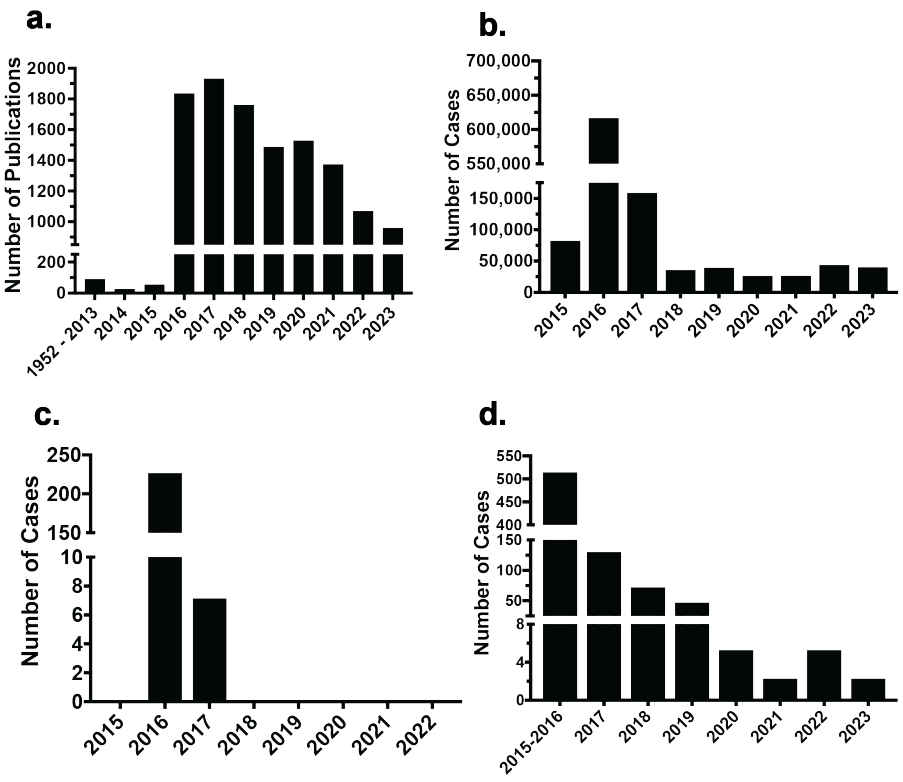


Figure 1. Dramatic increases in the number of Zika virus publications and reported case numbers since the epidemiological onset in 2015.

a. Number of publications Zika virus publication from 1952 to 2023 [9]. **b-d.** Number of Zika cases reported in the Americas (**b**) [10], the United States (**c**) [12], or California (**d**) [11]. Publications numbers resulting from “Zika virus” from the NCBI database. See text.

II. Clinical Manifestations of ZIKV

ZIKV infections can either directly infect adults or can be indirectly transferred in utero through infections in pregnant mothers, causing congenital disabilities. In adults, for the most part, infections cause minor, non-specific symptoms of viral infections or are entirely asymptomatic. Congenital infections, especially in the first trimester, lead to more severe outcomes, including neurological and physical malformations. The specifics of each are further discussed in the subsequent sub-sections.

Acquired Zika Infections

Acquired Zika Infection (AZI) is any Zika infection that does not result from vertical transmission from mother to child. A significant challenge for tracking and combatting the expansion of ZIKV, especially early in the epidemic, was the weak, non-specific symptom set or the complete lack of symptom presentation in up to 80% of all AZI cases, including in mothers [14]. Most symptomatic AZI patients have mild symptoms, including a low-grade fever, if any, headaches, rashes, joint pain, and conjunctivitis (amongst other ocular manifestations) that resolve in less than a week. However, more severe complications occasionally arise [7, 15, 16]. Most adult AZI cases recover without significant complications, as only around 3% of adults require hospitalization (based on 2,382 confirmed or probable US cases). Although children can get acquired infections, AZI primarily manifests in adults, which could be attributed to milder symptom presentation or quicker resolution in children as is typical of other viral infections (including human immunodeficiency

virus (HIV-1), hepatitis B (HVB), cytomegalovirus (CMV), and severe acute respiratory syndrome coronavirus 2 (SARS-CoV-2) [15, 17-21]. Severe neurological symptoms underly most AZI deaths are from causing Guillen-Barre Syndrome, a peripheral nervous system autoimmune disorder, amongst other neuroinflammatory diseases that can be lethal [22]. As mentioned previously, although primarily mild, ZIKV can target the eye in AZI cases.

Ocular Manifestations of Acquired Zika Infection (AZI)

Although not as severe as the ophthalmic complications during development, cases of AZI have been reported to target the eye in adults with non-specific symptoms typical of viral infections in the eye. Ocular symptoms manifest in ~20% of AZI cases, with median onset delayed one week from initial systematic viremia detection. The typical symptomology in ocular AZI cases includes conjunctivitis, acute maculopathy, and uveitis in one or both eyes [4, 23, 24]. As was the transmission case from tears, ZIKV is detected in the eye's fluids, including tears (beyond acute infection sera clearance) and conjunctival swabs [25, 26]. AZI patients reported initial vision changes and visual field defects in more severe ocular cases, although all cases have complete regression and vision recovery [27].

Even though most ocular-AZI infections are acute, the potential long-term retinal degeneration remains unknown. Notably, a small percentage of all arboviral infections lead to untreatable, lifelong visual impairment, suggesting that the same may occur in future ZIKV epidemics (262. Zaidi, 2018). Other viral infections lend further support, such as those by human herpesvirus-6A (HHV-6A), Epstein-Barr virus (EBV), and human cytomegalovirus (CMV), amongst others, underly retinal

degeneration in humans or rodent modeling [28-30]. Healthy RPE is critical for proper visual transduction by supporting rod and cone photoreceptors. Severe cases of ocular-AZI include protracted lesions to and disorganization of the uniform RPE monolayer in the outer macula and iridocyclitis [31]. As seen in age-related macular degeneration, RPE dysfunction is associated with progressive retinal degenerative diseases leading to PR death and blindness [32]. Although rare, a ZIKV-infected immunocompromised patient developed persistent retinal lesions extending over five months [31]. Indirectly, hypertensive iridocyclitis, a symptom of AZI, has been reported in cases of CMV and Rubella as a precursor for causing slow-progressing retinitis [33]. The potential for AZI to cause long-term ocular defects is highlighted by high levels of viral particles persisting in immune-privileged areas after systematic clearance [34].

Other than uveitis, the cellular tropism is consistent between acquired and congenital cases, with acquired infections targeting the macula iris, optic nerve, and ocular-muscular tissues [4, 24, 31].

Congenital Zika Syndrome (CZS)

In-utero ZIKV infections manifest in a set of hallmark physical and neurological consequences that are exceedingly severe compared to those in AZI. The specific hallmarks of CZS include (i) severe microcephaly with a partially collapsed skull; (ii) decreased brain tissue with particular patterns of brain damage; (iii) damage to the back of the eye; (iv) restriction of joint movement and (v) excessive muscle tone restricting body movement after birth [35]. The risk of infection for pregnant mothers depends on high regional variability in sampling, ruralness, environment, or

mosquito presence. A 36-month follow-up study of a small sample of US births by the US Zika Pregnancy and Infant Registry (USZPIR) found that 5.4% (122/2248) of live births had laboratory evidence of confirmed or possible Zika virus infections. Reports throughout the Americas vary from 4.1-36.6% [36-40].

CZS severity increases the earlier in pregnancy the mother is infected with ZIKV, as infections primarily in the first trimester are associated with the most severe CZS cases that reach term. If infections are early enough, they can result in implantation failure and miscarriage in 4-9% of suspected cases [38]. Overall, in a 36-month follow-up review by the U.S. Zika Pregnancy and Infant Registry (USZPIR), 9% (11/122) infants with CZS or 0.9% (20/2248; 11 with and 9 without CZS) of all live births with laboratory evidence of confirmed or possible Zika virus infections lead to death [36]. Similarly, unique manifestations and variability related to the timing of infection support a multifactorial mechanism, including immune activation, disrupted neuro-and-retinogenesis, cell death, and altered morphogen signaling. As with the significant hallmarks, the symptoms within ocular manifestations of CZS are physical, with changing ocular structures, and neurological in visual disruptions.

Microcephaly in CZS

One of the significant symptoms of CZS is microcephaly, or a reduction in head circumference (HC) for the age and sex at birth, and an underlying decrease in brain size. For CZS, definite cases of microcephaly are defined by an HC that is less than the third percentile (or not reported) from live births within the first two weeks after birth or at the time of pregnancy termination. The incidence of

microcephaly within confirmed CZS cases is highly variable, between 1% to 55%, although most support a lower range between 2.3-5% [37-43]. Inconsistent reporting of late-stage infections is a likely contributor to the variability. For non-ZIKV-related cases, microcephaly can occur after birth if subsequent brain development or head growth is slowed. However, there are no current reports of this from infections immediately before delivery, as expected from the limited clinical studies surrounding late-stage infections. Case-by-case variability based on head size does not predict the long-term persistence of neurological manifestations—seizures, vision, hearing, or developmental disabilities—that vary based on cumulative brain disruptions [35]. The earliest retinal development follows similar timing, precursor cell types, and mechanisms utilized in brain development, suggesting conservation disruptions underlying both.

Ocular Manifestations of Congenital Zika Infection (CZS)

A significant subset of CZS symptoms affects the eye and visual transduction pathway, primarily targeting the posterior segment of the eye. Still, defects to the anterior segment and oculomotor function occur. Ocular developmental consequences are unique to the ZIKV epidemic in the Americas. Broadly, the ocular structures targeted are the retina, optic nerve, and retinal vesicles [4, 23, 24]. Clinical manifestations commonly include macular damage to RPE, like focal pigmentary mottling and chorioretinal atrophy, highlighted by ocular coherence tomography (OCT) imaging of retinal tissue in infants [15, 24]. Clinical manifestations, such as hypoplasia (underdevelopment), cupping, and atrophy, often occur in the optic nerve. Other reported cases include other retinal lesions

including hypopigmentation, vascular tortuosity, abnormal vessel termination, amongst others), congenital glaucoma, iris coloboma, microphthalmia, cataracts, lens subluxation, and intraocular calcifications [4, 23, 24, 35]. Although less common, ZIKV can target oculomotor tissues, causing impairments that include loss of pupillary responses, strabismus or misalignment of the eyes, and nystagmus [4, 24]. The diversity of structures impacted by infection supports initial infections in upstream early and intermediately differentiated retinal precursors with other compounding factors due to the high order of complexity in retinogenesis.

A significant driver of microcephaly is caused by altered neurogenesis waves leading to the depletion of neural progenitor cells (NPCs) required for proper cortical expansion [44]. In the developmental cascade, retinal precursor cells (RPCs) are downstream of earlier neural precursor cells (NPCs) that are disrupted in microcephaly, implicating RPCs as the driver for the prominence of retinal manifestations resulting from infants infected in the first trimester [24, 45]. As with disrupted progenitor-genesis in microcephaly, cases of microphthalmia indicate that a similar mechanism is at play. The impact of RPCs can disrupt proper vision in many ways as minor alterations early could result in disruption in the highly organized and accurately connected retina that is required for proper phototransduction through the retina onto the optic nerve and, ultimately, the brain that must be conducive for higher-order visual processing [46]. Therefore, visual impairment can arise from either developmental deficit targeting retinal structures involved in phototransduction or visual processing in the brain.

Investigations focused on visual function and long-term ocular health have faced challenges due to the rapid decline in case numbers and lack of follow-up studies [47]. Expansive reviews of clinical reports find that structural defects occur in about 23% (from 21-55%) of pregnancies with suspected or confirmed in-utero exposure to ZIKV; however, regional discrepancies muddle the total number of confirmed cases, mainly from variability in the sampling method [27, 36]. Focusing only on microcephalic cases determines closer to a 50% (and up to 75%) pervasiveness of ocular defects associated with microcephaly [4, 23, 24]. Within a cohort of 95 cases of infants with suspected CZS that received ophthalmologic evaluations, only 12/95 (13%) presented with microcephaly, and from those 12, 50% (6/15) had ocular manifestations representing only 20% (6/32) of total such infants [24, 33]. Alternatively, in a 36-month follow-up of the 122 infants born with CZS from the USZPIR, (28/122) 23% had eye symptoms, with (10/28) 36% with only eye symptoms. As a specific example, a follow-up investigation on infants that had tested positive for ZIKV found that 100% of the infants (31/ 31) had some form of visual impairment, with 97% being under a visual-developmental milestone for their age group [36]. Although visual transduction was affected for those infants, less than half (14/32) had structural defects in the eye. Broadly, the structural defects were either in the eye itself targeted the posterior of the eye, especially the macula, and the optic nerve, with limited anterior symptom presentation [23, 27, 47]. Even when structural integrity is maintained, the high incidence of vision increases the necessity of studying how ZIKV impacts the eyes and retinal neurons. Although

retroactive studies initially understand the incidence of ocular symptoms, few follow up on those later in life.

For further reviews on Zika virus in the eye and clinical ophthalmic complications, refer to de Paula Freitas et al., *Current Opinion in Ophthalmology*, 2017; Marquezan et al., *Survey of Ophthalmology*, 2018; Ventura CV, Ventura LO, *Pediatrics*, 2018

Long-Term Consequences of CZS

Limited long-term follow-ups are attempting to correct vision-impacting CZS cases, and those focus on infants with milder, nonstructural disrupting symptoms. Early identification of symptomology and non-surgical correction lead to visual improvements. In this study, the primary candidates for correction presented hypoaccommodation, or the inability to maintain proper visual acuity, impacting 81% of the ocular CZS cases—of those, 100% had visual responses in at least one eye below normal without corrective spectacles. Visual responses remained low even with specific, over-corrective lenses; however, 62% had immediate binocular visual improvements. In 38% of the cases, there were improvements in only one eye with no immediate binocular visual improvement. Surprisingly, in 7 cases with no visual response pre-glasses, the vision was restored with glasses immediately [27].

Furthermore, for all monocular optic nerve and retinal pathologies, 23.5% of the eyes improved with glasses (23.5% had structural abnormalities, and 38.3% were normal) [27]. Promisingly for future flare-ups, although still significantly more challenging in rural communities, the combination of comprehensive, multi-disciplinary ophthalmic examinations (including tests for highly manifesting

symptoms like retinoscopies and cycloplegic refraction) with early correction can improve visual acuity in children with CZS. In summation, the discrepancies between microcephaly and ocular manifestations highlight visual screening as a better predictor of CZS than head circumference during future ZIKV flare-ups, as initially proposed by Zin et al. in 2017 [48].

III. Zika Virus Structure, Establishment, and Life Cycle

Zika Virus Specifications and Structure

Zika Virus (ZIKV) is an 11 kb positive-sense single-stranded (ss) RNA virus in the flavivirus genus, which includes others such as Dengue and West Nile (1. De Paula Freitas, 2017; 53. Christian, 2019). ZIKV replication occurs as a polyprotein with one long open reading frame (ORF) encoding three structural and seven (NS) nonstructural proteins. The ORF is ~10 kb comprised of ~100 nucleotides (ntd) residing on the 5' untranslated region (UTR) and ~420 ntd on the 3' UTR. The ORF encodes the polyprotein precursor that, with host proteases, is critical for processing the resulting polyprotein into all ten viral proteins [49, 50]. The seven nonstructural proteins are NS1, NS2A, NS2B, NS3, NS4A, NS4B, and NS5, contributing to pathologies, immune evasion, and replication [49, 51]. Crucially, NS proteins are heavily relied on for successful replication by facilitating the hijacking of cellular machinery and for facilitating genome replication and polyprotein processing. The three structural proteins, the capsid (C), pre-membrane (PrM), and envelope (E), together form the overall virion structure and are involved mainly with viral pathology. The icosahedral ZIKV capsid comprises the C protein surrounded by a

host membrane-derived lipid bilayer. M and E proteins support the C protein and capsid formation by anchoring viral particles to the host cell's outer membrane by forming transmembrane helices. The E protein is also crucial for cell binding and membrane fusion for cellular entry. Generally, the E-protein-dependent mechanism of fusion that ultimately results in viral entry requires mediation through a few classes of specific host receptors for proper clathrin-mediated endocytosis and entry. After replication, functional ZIKV particles are released into the extracellular space after replication and maturation [49].

Zika Virus Life Cycle

Zika Virus Receptors

Briefly, the implicated ZIKV receptors are primarily αvβ3 integrins, C-type lectin receptors, and phosphatidylserine receptors of the *TAM family of related RTKs, including *AXL, *TYRO3, *MERTK, CD209/DC-SIGN, and TIM1 (HAVCR1) [49, 52]. The diversity of potential entry receptors and infected tissues could be attributed to the array of structurally distinct virions characteristic of flavivirus replication [49]. ZIKV infection by TAM receptors is through apoptotic mimicry, triggering endocytosis in phagocytic cells by harnessing their physiological function for the recognition of apoptotic cells by imitating the negatively charged lipids of apoptotic cells [53]. After entry, a coordinated series of events and host proteins are required for replication and maturation. A comprehensive investigation of receptor expression in the eye is presented in section IV. Review of the Eye.

Zika Virus Life Cycle

Autophagic Pathways

The life cycle of ZIKV is heavily dependent on endo-and-exocytosis. During normal autophagy, after activation of receptors by conventional methods or, in the case of ZIKV infection, the clathrin coat of clathrin-mediated endocytosis is recruited through the AP2 complex leading to plasma membrane invaginations resulting in intracellular vesicles that mature with trafficking along the actin-microtubule networks with Rab GTPases. During maturation, removing the clathrin coat allows the fusion of early endosomes. Within endosomes, during vesicle maturation, there is a gradual pH decrease from proton pumps and acidic vesicle fusion, with early endosomes holding an even lower pH. Conventionally, the endosomal cargo is sorted for degradation by multivesicular bodies and late endosomes into lysosomes, or it can be recycled either at the cell surface, by exosomes, or in the trans-Golgi network. During the degrative pathway, the pH gradually decreases through late endosomes with further lysosome acidification. Viruses, like ZIKV, harness the tightly controlled pH microenvironment for optimal fusion based on pH, membrane composition, and cellular protease activity.

Furthermore, acidic microenvironments are commonly required before fusion for viral endocytosis [54]. As the viral life cycle is highly dependent on all these pathways, ZIKV induces autophagy to expedite replication and overall virus production, likely by increasing the incidence of optimal conditions [55]. Usually, lysosomes degrade extracellular material internalized by endocytosis or intracellular components sequestered by autophagy [56]. ZIKV harnesses these pathways for successful amplification. The Zika virus life cycle is shown in **Figure 2**.

Zika Virus Entry and Trafficking

After recognizing and binding receptors, ZIKV enters cells through clathrin-mediated endocytosis and is internalized for replication. ZIKV relies on the diffusion of viral particles into clathrin pits through either stochastic turnover of binding factors or from clathrin-pit priming by the transport of virus-receptor complexes through preexisting clathrin-coated pits primed at the PM [53, 54, 57]. When bound, the clathrin-coated pit invaginates to encapsulate the viral particle before closure and excision through dynamin mediation [53]. After entry, as in normal endosomal trafficking, the maturation of ZIKV-containing endocytes into late endocytes allows fusion between viral and endosomal membranes. With maturation, the acidification of the endosomal microenvironment causes an irreversible conformational shift in protein E, playing a critical role in membrane fusion and the release of intracellular genetic material, discharging ZIKV RNA into the cytoplasm, furthering subsequent replication and translation [53, 54]. Alternatively, endosomal trafficking can take ZIKV-containing vesicles to the ER, resulting in ER budding and the creation of immune-privileged viral replication factories [53], which are critical for all aspects of ZIKV replication.

Zika Virus Replication and Folding

Infection progression can take two routes once new (+) RNAs are synthesized: (1) recruitment for further rounds of translation and replication or (2) incorporation into virions, which is the focus of the rest of the section. Briefly, virion incorporation triggers their assembly on the ER that, after replication and folding,

travels through the secretory pathway, utilizing pH decreases for final maturation before release into the extracellular space [58]. The formation of internal replication factories requires ER morphogenesis through the exploitation of the biochemical properties of the ER [53]. As negatively charged lipids are restricted to the internal plasma membrane, the loop surface of ZIKV has specific localized charges throughout. The inner region has positive and negative charges, whereas both distal ends have negative charges, all facilitating replication factory formation [53, 59]. The spatial segregation of viral replication factories is multifactorial as it would allow the concentration of metabolites for RNA replication in tandem with protecting them by, in essence, hiding viral RNA from cytosolic RNA/dsRNA sensors and cellular nucleases. After establishing viral replication factories, as seen by a high density of dsRNA, the cytoskeleton network critical for trafficking viral particles to the ER during infection is heavily disrupted. That disruption can reach the point of dramatic microtubule displacement and a tightly linked network surrounding and caging the nucleus itself [60]. These replication factories are indispensable for the ZIKV life cycle.

All stages of ZIKV replication rely on the membranous environment within ER-budded viral replication factories coupled to RNA and protein synthesis and virion assembly [57]. This coupling initiates the assembly process through the C protein associating with newly synthesized RNA genomes, producing hallmark flaviviral dsRNA intermediates [57, 60]. Furthermore, nonstructural proteins play critical roles in replication. For instance, NS5 is integral for flaviviral RNA genome replication. The N-terminal contains a methyltransferase that adds the 5' RNA cap

connected to an RNA-dependent polymerase connected by a short-linker. The 5' cap dually supports polyprotein translation and suppression of host innate immune responses [50]. Immature virions arise by budding from the ER initiated by the immature prM/E heterodimer after initiation by the encapsidation of viral RNA [57]. After budding, the immature virions must be further processed and complete maturation before a successful release.

ZIKV Particle Maturation and Release

Following the initial budding of immature virions, amongst other modifications, they gain a carbohydrate addition, allowing further processing through the trans-Golgi network, where the prM portion gets glycosylated. As those new ZIKV particles assemble in the ER, they exhibit a spiny surface resulting from 180 prM-E heterodimers unified into 60 trimeric projections. During maturation, the components of the spiny surface are reorganized into 90 dimers. This structural reorganization exposes the prM cleavage site, allowing the removal of the prM protein from the dissociation of prM-E heterodimers by the host protease furin [53, 57, 61]. After the dissociation of prM-E heterodimers, the pr peptide and M protein cleave the E proteins, helping with virion maturation[53, 57]. The glycosylated "pr" portion remains associated with the viral particle until immediately before virion release. Subsequently, maturing virions are released into the extracellular space through the exocytosis pathways, priming the viral particles for further maturation and final release [57]. The culmination of flaviviral maturation (from C, prM, and E to C, M, and E) occurring during the final exocytosis is trademarked by the 90 homodimers of E and M in fully mature particles getting closely packed into an

icosahedral shell but still without the fully dissociated pr portion yet [53]. This process reaches critical mass late in infection when viral release begins to lyse cells; they exhibit vacuolization in conjunction with microtubule disassembly. Final exocytosis happens in tandem with forming a pore-like opening that allows unfettered cytosolic exit from newly synthesized positive-strand ZIKV RNA, furthering virion formation or protein synthesis. Those ER pores are associated with a high density of virions, further demonstrating the spatial segregation required for viral replication (similar to DENV and other flaviviruses) [60]. Although the direct mechanism surrounding the final release of ZIKV virions to the extracellular space remains elusive, successful ZIKV replication and maturation are imperative for proper release.

Within different contexts, there is support for a few probable pathways for the final ZIKV release. The most direct mechanism for release would be from fusion to the PM, as supported by the assembly and maturation in luminal regions of membranous compartments. Unlike with entry, this method is clathrin-independent, further emphasizing potential alternative pathways for release [58]. ZIKV release by PM fusion can occur in either larger vesicles containing multiple virions or smaller, single-virion-containing vesicles that can remain stand-alone or independently protected within the larger vesicles. There are a few possible mechanisms for PM binding and the release of larger vesiculated viral particles. Firstly, larger vesicles rely on both ER and Golgi membrane utilization as Golgi proteins are redistributed into replicative membranes, potentially facilitating PM delivery. Secondly, multiple virions are contained within those larger vesicles, characteristic of secretory

autophagy. One advantage is that vesiculation preservation in released particles would maintain the insulation of viral particles from the immune response or other antiviral pathways as occurs in replication factories. Although larger vesicles have advantages, single particle release dominates total ZIKV release. How the larger vesiculated virion clusters are repackaged into individual particles remains unknown. Still, the massive exodus of ZIKV particles is reminiscent of the large wave of secretory vesicles distinct to trans-Golgi-dependent secretory granule-related pathways [58]. Ultimately, fully matured particles are exocytosed and released from the host cell, allowing the further dissemination and reinfection of ZIKV in other cells [57].

The diversity of viral particle packaging creates heterogeneous flaviviral phenotypes. High particle diversity is likely necessary for apoptotic mimicry and multimodal entry through the implicated receptor classes in the diverse cell types susceptible to ZIKV. Substantial evidence supports an inefficient prM cleavage in some infectious particles released, exposing cells to mature and immature viral particles. Viral particle heterogeneity is conserved for DENV and WNV caused by a mutation to an amino acid (AA) in the prM cleavage site, reducing cleavage efficiency and causing receptor shifting, specifically to DC-SIGN. Similarly, supporting the diversity of cell types infected and respective variability in receptor expression between them, ZIKV may also use prM as an entry cofactor because infectivity has been linked to a mutation of a single AA in the prM region [53, 57, 61]. With a massive intracellular viral load during infection, the highly complex process for ZIKV replication is not as tightly controlled as expected. Decreased

regulation leads to the improper replication and maturation of some ZIKV particles, supporting the diversity of receptors utilized for the multitude of cell types that ZIKV targets.

pH Dependence for the ZIKV Life Cycle

Multiple stages of the ZIKV life cycle depend on pH, including the release of viral genetic material, structural rearrangement, and maturation. Viruses can harness host cells' tightly controlled pH microenvironments for optimal fusion, membrane composition, and cellular protease activity. Furthermore, before fusion, an acidic microenvironment is commonly required for viral endocytosis as the initial binding and host-cell fusion depends on the viral membrane's pH. Early in trafficking, there is a gradual pH decrease during vesicle maturation from proton pumps and acidic vesicle fusion, with early endosomes maintaining a pH of ~6.3-6.8. Endosomal cargo is either sorted for degradation by multivesicular bodies and late endosomes to lysosomes or can be recycled at the cell surface, exosomes, or the trans-Golgi network. During the degrative pathway, the pH decreases from ~6 to 4.8 in late endosomes and down to 4.5 in lysosomes [54]. Additionally, the acidic endosomal environment triggers an irreversible conformational change in protein E to the final, lowest-energy conformation of E, leading to membrane fusion and release of viral genetic material and further replication and translation processes [53, 56]. The pH dependence for ZIKV entry and ER trafficking is also conserved through later stages of the life cycle.

Once established in viral replication factories, the ER's neutral pH supports immature particles' trimeric projections [53]. The overall Golgi network has two sub-

compartments, the cis-and-trans-Golgi, with decreasing pHs along the cis-trans axis from 6.7 to 6.0 in each respective compartment [62]. Once they begin budding from the ER and entering the trans-Golgi network, that decrease in pH is crucial for shifting prM-E heterodimers to trimeric projections during the new particle assembly process, allowing furin cleavage [53, 57, 61]. After pr portion cleavage and maintained association until the final ZIKV release, the neutral pH of the extracellular medium results in its dissociation [53]. Although ultimately overwhelming the cell, the process of ZIKV replication and overall life cycle is highly complex, requiring the manipulation of a comprehensive amount of host processes with a high level of coordination and dependency on specific environmental shifts, like pH.

Zika Viral Protein Localization

Subcellular localization of individual ZIKV proteins is crucial for understanding viral infection and successful replication, with the potential for identifying therapeutic interventions. In general, localizations are in regions expected based on the life cycle, but different methods have identified slightly variable localizations of specific proteins depending on the context of the assays. Molecular cloning experiments investigating individual ZIKV protein expression demonstrate primary ZIKV distributions amongst the ER, Golgi apparatus, endosomes, lysosomes, autophagosomes, and nucleus. Indicative of viral replication, proximity-dependent biotin-identification labeling, and FLAG-IP with couple mass spectrometry reveal ZIKV interactions surrounding protein processing, vesicle trafficking, RNA processing, and lipid metabolism. Although the expression

profiles may shift when co-expressed with other ZIKV proteins, single cloning strategies highlight initial localizations. The capsid localizes to the nucleus and Golgi. Golgi localization also occurs for NS2B and NS4A. Lastly, ER localization (determined with calreticulin) co-staining supports localization for the envelope, prM, and NS2A [63].

Interestingly, the localization changes when multiple viral proteins are expressed in tandem. NS5 with a nuclear localization sequence (NLS) interacts with ZIKV NS3-helicase during viral replication at the ER, although the single expression forms puncta in the nucleus. Similarly, NS3 localizes to the mitochondria when expressed alone but changes to an ER localization in the presence of NS2B. In other wild-type modeling strategies, viral proteins target the nucleus. The capsid interacts with multiple nucleolar proteins, and NS5 targets and disrupts nuclear Cajal bodies. Within those same contexts, several viral proteins (prM, Env, NS2A, NS2B, NS4A, and NS4B) interact with various ER proteins. Generally, as the complexity increases, the localization within more complex contexts follows those expected for replication at viral replication factories in the ER [63]. A detailed understanding of these complex changes and interactions is crucial for developing therapies mitigating ZIKV replication.

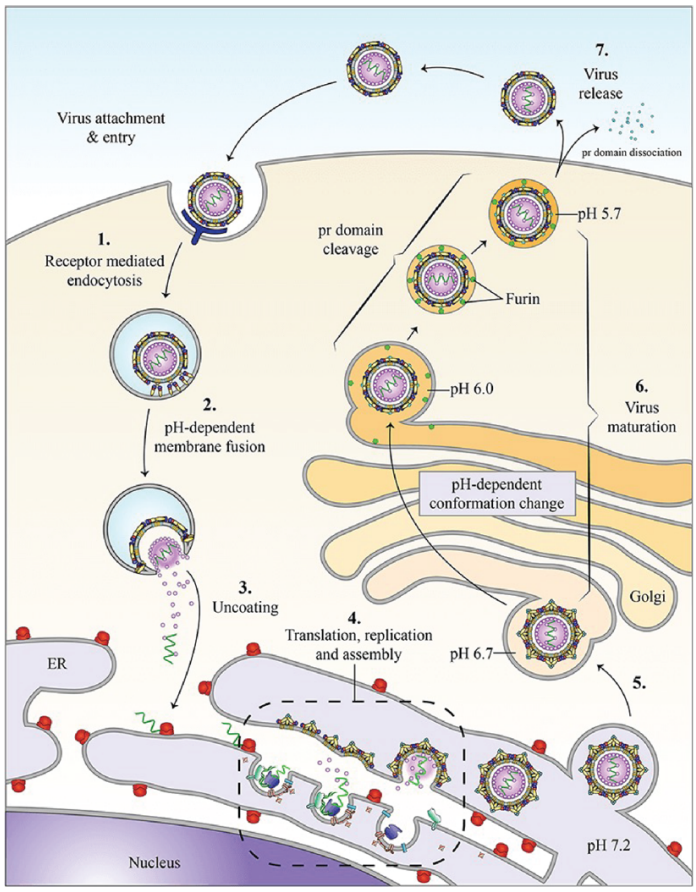


Figure 2. Zika virus life cycle.
The process of Zika virus replication from attachment and entry to viral maturation and release. Note the many pH-dependent steps. See text for further details. (Figure from the Richard J. Kunh Lab, *Department of Biological Sciences*, Purdue University [64]).

IV. The Retina

Retinal Structure and Organization

Congenital ZIKV infections affect eye development and vision, implicating infection targeting multiple cell types in the retina that need to be organized into a high level of overall structure to maintain retinal integrity, functions, and proper signaling (**Figure 3 a-f**). Specifically, the retina is composed of 10 distinct cell types functioning in various roles for the overall health of the retina, summarized into

supporting overall ocular structure and for the 3 major roles in phototransduction mentioned in detail below phototransduction initiation, complex integration of the binary input signals requiring multiple types of retinal neurons (RNs), and perpetuation of phototransduction to the brain. Briefly, phototransduction is initiated by the 2 types of photoreceptors (PR), rods (**a**) and cones (**b**). From PRs, as signals transverse the retina, they are regulated by horizontal cells (HC) (**c**). From the HCs, signals are integrated through amacrine cells (AC) (**d**) to multiple bipolar cells (BC) (**e**) before passing to retinal ganglion cells (RGC) (**f**). Once the RGCs receive those integrated signals, they are transmitted through the long RGC axons comprising the optic nerve (ON) to the brain [65].

The focusing of light from the lens onto the retina and, by proxy, amplifies the destructive UV radiation. The light and UV damage is received by PRs that become heavily damaged by taking the brunt of the harm. To combat this, PRs have distinct outer segments (OS) that are constantly turned over, avoiding long-term dysfunction from accumulating permanent DNA mutations. Two non-neuronal cell types, retinal pigment epithelium (RPE) (**g**) and Müller glial cells (MGC, **h**), are responsible for PR OS processing and the maintenance of overall retinal health. The RPE comprises heavily pigmented cells lying directly beneath the PRs at the back of the eye, which is integral in supporting PRs and sustaining the photosensitivity of the retina. In addition to the critical role of phagocytosing the damaged OS, pigmentation of RPE scatters some of the direct light, amongst other functions [65]. Alternatively, MGCs with distinct functions are responsible for sustaining the health of the rest of the retinal neurons through phagocytosing apoptotic cells and other cellular debris.

Together, these cell types function harmoniously within the high order of structure for maintaining proper retinal function.

Retinal Neurons Involved in Phototransduction

Photoreceptors

As the initiators of phototransduction, the specific localizations, ratios, and unique properties of rods and cones are critical for high visual acuity. Rods comprise 95% of the photoreceptors in the retina, whereas the remaining 5% are cones. Rods are localized to the peripheral retina and are highly sensitive to light while lacking the ability for color distinction. The increased light sensitivity is utilized primarily for visual transduction in low-light conditions, creating a black-and-white spectrum for greyscale night vision. Conversely, cones have decreased light sensitivity during high light conditions during the daytime, but from a heightened sensitivity to red, green, and blue light are utilized for color vision. RGB detection is from different ratios of the three independent types of cones: red-sensing (64%), green-sensing (32%), or blue-sensing (2%). Red and green specific cells localize directly in the fovea in a ratio of 2:1, whereas blue light-detecting cones are in the surrounding macula. The high density at the central retina supports proper spatial acuity from 2-distinct point processing in the brain. As expected from the low cones-to-rod ratio, the synaptic connectivity of macular cones to RGCs is 1:1, unlike the highly abundant rods with a 3:1 ratio critical for resolving background from low-light conditions. Compared to rods, the lower ratio of synaptic connectivity in the less prevalent cones causes them to contribute more to overall visual processing in the

brain. In addition to differing PR ratios and localizations in the retina, cones and rods have distinct properties supporting night or day vision. During constant light exposure, rod cells become saturated, requiring a refractory recovery period, unlike cone cells that rapidly adapt to light. That difference in response to light exposure is supported by the membrane current recovery time, as rods can take up to 20 minutes, which is about 60,000 times slower than the cone recovery of about 20ms [66]. Furthermore, in addition to differing connection ratios, the transmission of the chemical signals between PRs to RGCs is unique between rods and cones. The distinct properties and localizations of rods and cones are utilized for the independent diurnal visual rhythms.

Retinal Ganglion Cells

Retinal ganglion cells (RGCs) are the primary cell type comprising the optic nerve (ON) functioning to connect and transmit signals from the retina to the brain. RGCs have long axonal projections that converge at the optic disk, leaving the eye. As the optic disk is critical for allowing RGC axons to leave the eye, it is devoid of PRs, thus creating a blind spot in vision. Additionally, it is critical that before passing through the lamina cribosa and into the brain, RGC axons traversing the retina remain unmyelinated to avoid obstructing incoming light.

About 20 distinct RGC cell types function harmonically to process and transmit visual input. In addition to traditional photoreceptors for light sensation, a small proportion of a subtype of RGCs (1-2%) are light-sensitive through a closely related melanopsin mechanism as canonical PRs. Melanopsin is a G-protein peptide neuromodulator that helps in transmitting image-forming information. These

light-sensitive RGCs have an independent, non-imaging-forming role in circadian rhythm, melatonin modulation, and pupil dilation. The primary function of the other types of RGCs is to integrate excitatory and inhibitory inputs from the intermediate neurons ACs and BCs [66]. Specifically, the BC to RGC connections are the primary and most direct transduction method between PRs and RGCs [67]. Alternatively, the collation of RGCs and ACs creates on-off centers, allowing the tracking and interpretation of small objects moving from afar [66]. Overall, RGCs are critical in integrating and transmitting visual signals to the brain, with a photosensitive subtype that is key for modulating light-responsive pathways.

Amacrine Cells (ACs)

ACs are intermediate neurons critical for integrating the photonic inputs from PRs and can be either excitatory or inhibitory due to unique gap junctions. AC's inhibitory function is by releasing the inhibitory neurotransmitters GABA or glycine. Although they release inhibitory neurotransmitters, the unique gap junctions and pre-or-post synaptic outputs allow opposite roles, as presynaptic ACs inhibit BC terminals, whereas postsynaptic ACs inhibit RGC dendrites. Per the varied RGC types and functions, ACs have more diversity in functions, serving utilitarian roles supporting the myriad of RGC types and functions. Specifically, the 20 unique types of RGCs promote over 42 different types of ACs. Of the 42, they function in independent units acting as microcircuits for fine-tuning the retina by resolving the intermediate shades and the directional movement of light. Each type is organized into distinct groups based on the proximity between ACs: wide field, medium field, and narrow field ACs [66, 68]. Wide field ACs help with horizontal signal integration,

although less well understood, medium field ACs help with vertical integration. Lastly, narrow-field ACs extending through multiple layers significantly contribute to vertical transmission. Overall, the organization and diversity of AC types and functions are critical for proper signal integration and propagation from PRs to RGCs.

Bipolar Cells

Bipolar cells (BCs) extend through the retina as second-order long-projection neurons that, rotated to a vertical orientation, are also crucial for receiving and relaying signals between PRs and RGCs, thus bridging the outer PR layer with the IPL. By stratifying 5 independent regions of the IPL, BCs form the initial building blocks for vision from the initial binary inputs from connections to multiple PRs. In response to light, those building blocks carry out diverse functions, such as the chromatic composition, polarity, contrast, and temporal profiles of vision.

Although there are 13 types of BCs, they can be categorized into 2 groups: rod and cone bipolar cells. Within those groups, they can be independently organized into ON or OFF BCs based on whether they depolarize or hyperpolarize in response to light. Rod BCs only contain ON BCs, whereas cone BCs function as both. With higher sensitivity for vision at night, rod cells require the quantitative analysis of the binary inputs achieved from photonic striking; therefore, only ON BCs are required. Alternatively, cone BCs require both ON-and-OFF BCs to differentiate nuances from the incoming photons qualitatively to the different classes of cone cells in daytime vision and the other primary functions of the retina (i.e.,

color, movement, and fine details). Diversity in BC function and IPL stratification are required for the visual building blocks to deconvolute visual inputs properly [66].

Horizontal Cells

Horizontal cells (HCs), next in the cascade, have specialized functions for signal integration and propagation between BCs and PRs and supporting adjustments during changes in light conditions (both high and low). As the name suggests, HC projections extended horizontally with widespread and diffuse projections extending to neighboring cells. HCs have a robust expression at the outer retina, with their cell bodies localized in the inner nuclear layer. Contact of HC with the OPL is critical for structuring the spatial receptive field by conveying visual stimuli's transmission polarity, spectral sensitivity, and speed. HCs, such as GABAergic interneurons, have an inhibitory effect on BC input and rods and cones. Although contested in the field, they may utilize an alternative mechanism of inhibition through the regulation of synaptic cleft pH. HC sheathing of BCs is critical for signal integration between ON BCs and basal dendrites of OFF cone BCs. That lateral inhibitory effect of HCs amplifies the ON-OFF centers of the surrounding BCs and, through that antagonization of the original signaling inputs, increases contrast enhancement through two-point differentiation [66].

Non-Neuronal Retinal Cell Types

Although most of the cells in the retina are neuronal, functioning as the primary cells for phototransduction and vision, they require other non-neuronal cell types to support them and for the overall structure of the retina. The major non-

neuronal cell types of the retina are MGCs and RPE. Specifically, MGCs support neurons and regulate the extracellular space, and the RPE supports PRs and maintains the immune privilege of the eye by comprising the outer blood-retinal barrier [69, 70].

Müller Glial Cells (MGCs)

MGCs reside in the OLM of the retina, extending into and creating the retina's ILM. Thus, their supporting role connects inner PR segments and basement membrane cells. The ILM is formed by the fusion of lateral contacting enlarged foot-like processes, or boutons, of MGC axons [66]. MGCs also are critical for supporting and maintaining the structure of the retina and the metabolic and homeostatic environment of retinal neurons.

One of the primary roles of MGCs is for the physical characteristics of the retina. MGCs act as the glue of the retina, filling the space between retinal neurons, functioning to buffer the embedded neurons from physical damage, and as a scaffold supporting neuritic growth and plasticity. It was recently discovered that by guiding light through the inner retina, MGCs facilitate image propagation and the spatial distribution of light patterns. When there are changes in the osmotic pressure of the retina, as occurs during periods of intense neuronal firing, MGCs mitigate the physical impact by altering the extracellular space volume to relieve the pressure. Other than RGCs, where it is lethal, MGCs are the only retinal cell type capable of cell cycle reentry, de-differentiation, and successful expansion into a neural progenitor pool [69, 71]. During pathological conditions like light damage, MGC-derived neural progenitors allow the regeneration of lost PRs. Their

regenerative capacity supports a potential mechanism during developmental ZIKV infections with retinal neuron or photoreceptor loss, where a subset of neural progenitors could arise from MGCs to replace the damaged or lost neuronal cells [69].

In conjunction with physical roles, MGCs are critical for directly supporting and maintaining the retina's chemical environment and metabolic state. MGCs are activated by almost all pathogenic stimuli, and they help mitigate damage to retinal neurons (RGCs, BCs, and PRs) by secreting select neurotransmitters and pro-inflammatory cytokines and chemokines, specifically via BDNF, CNTF, FGF, IGF, NGF, NT-3 and 4, GDNF, LIF, and PEDF [72]. MGCs are directly involved in the nutrient and oxidative regulation of PRs. Briefly, utilizing glutamate and GABA uptake supports neuronal excitation while mitigating oxidative stress. When PRs undergo metabolic stress, as with the circadian rhythm's typical light and dark cycles, other substrates are produced to support them. The rapid uptake of NTs plays another role in the synaptic regulation of inner retinal neurons by removing and containing extracellular glutamate from synaptic clefts after excitatory firing, reducing the toxic effects of glutamate on retinal neuron health [69]. Lastly, in addition to retinal neurons, MGCs support the RPE. MGCs regulate the tightness of the blood-retinal barrier and neurovascular coupling and assist in minimizing light scattering in the inner retinal space [69, 73]. In summary, MGCs play critical supporting roles for the retina through chemical modulation, physical support, and facilitating inner retinal immune privilege.

Retinal Pigment Epithelium

The retinal pigment epithelium (RPE) is a cobblestone monolayer of pigmented cells located at the outermost layer of the retina, behind the PRs, and connected to the Bruch's membrane and choroid. RPE support is crucial for proper vision and the retina, specifically the PRs, through various physical and metabolic functions. They have multiple roles directly supporting vision, including light absorption, transport of nutrients and ions, retinoid cycling, GF secretion, and phagocytosis of PR outer segments [70]. The RPE is heavily melanated, appearing dark brown. The crystalline structure of melanin helps light diffusion and absorption of scattered light. In combination with lipofuscin, melanin is critical for reducing UV damage to internal neurons and the retina. To carry out its supportive functions, the RPE is highly metabolically active. Within the retina is an accumulation of damaging reactive oxygen species (ROS) from the constant photooxidation of light stimulations that is severely reduced through the complex metabolic systems within RPE. Some of the components RPE utilizes for combatting and scavenging ROS are a high level of antioxidants (like superoxide dismutase) and melanosome participation. The structure and basolateral polarization of the RPE are critical for functioning. During the normal visual cycle of PRs, their OS is easily damaged by light, amongst other mechanisms, requiring a constant OS turnover and renewal. The apical microvilli extending to the PRs OS are utilized for OS phagocytosis, and basal folding increases the surface area for nutrient exchange, supporting PR function. RPE binds the PR OS primarily through recognition and endocytosis by the TAM family of receptors. This aspect is fascinating because the TAM receptors

are implicated in ZIKV entry [74]. The role of the TAM receptors in RPE function, a major target of ZIKV, may contribute to visual manifestations of CZS.

Physically, RPE supports the retina by creating the inner blood-retinal barrier (BRB). The inner BRB is maintained through the tight gap junctions created by ZO-1, occluding, and claudin. BRB integrity is required to tightly control the movement of substances between the retina and choroidal bloodstream while restricting widescale immune activation and maintaining the eye's immune privilege. Retinal health requires tight regulation of transport to remove waste into and transport other nutrients, water, and electrolytes out of the bloodstream. There is a lack of blood vessels in the eye itself. Therefore, primary transport is through the RPE directly into the underlying, highly vascularized choroid. Amongst others, regulation, facilitation, and transport in RPE between the inside and outside of the retinal barrier utilize specific mechanisms, including membrane pumps, endocytosis, and passive diffusion [74]. The multifunctional supportive roles of RPE are essential for PR function, highlighted by PR loss from RPE dysfunction in age-related blindness [70]. Together with metabolic support, the RPE helps the entire retina by forming the inner BRB and acting as the primary site of waste removal and nutrient exchange.

Phototransduction

The primary role of the retina is to carry out phototransduction, or the conversion of light stimuli to chemical signals that are transmitted to the brain for visual processing (**Figure 3 I-III**). Proper phototransduction uses cell types in multiple retina layers, including rods and cone photoreceptors (PR), retinal ganglion

(RGCs), bipolar (BP), horizontal (HC), and amacrine cells (AC). Initially, light enters through the dome-shaped cornea, helping focus it through the pupil and lens onto the back of the retina. As the light enters the retina, PRs receive it, and phototransduction is initiated by converting the binary light inputs into electrical signals that can be transmitted to the brain (**I. Initiation**). Unlike most other types of neurons, PRs start in a depolarized state, with open calcium-gated channels allowing the constant release of glutamate. Upon the absorption of a photon of light, the inner segment membrane hyperpolarizes, causing changes in NT release. Breaking a double bond from photonic stimulation induces a conformational shift in the rods, converting 11-cis-retinol into all-trans-retinol. A series of conformational changes to the G-protein coupled receptor Rhodopsin, culminating in an activated state, metarhodopsin II, stimulates transduction while transforming to the inactive form metarhodopsin III. This cascade decreases the cGMP concentration, ultimately hyperpolarizing the PR. Spent, inactive components from the initiation cascade are then transported to other cell types to be recycled and re-isomerized. Specifically, the RPE is utilized for this. After initiation at PRs, those chemical signals are transmitted to RGCs, in concert with other retinal neurons, for proper integration (**II. Integration**) and, ultimately, transmission through long RGC axons extending through the optic nerve to the brain (**III. Transmission**), where they create the images required for vision in the visual cortex [75]. Although the significant stages of phototransduction can be simplified to a key series of steps, it requires synergism of the highly specialized functions of all the retinal cell types. Thus, damage to the retina can be debilitating. For example, viruses (such as ZIKV) can disrupt the

retina's function in the intermediate and late stages of infection by disrupting the function of multiple cell types.

Human Neural and Retinal Development

Human Neural Development

New neurons arise from neural precursor cells (NPCs) undergoing direct or indirect neurogenesis. Early in mammalian cerebral cortex development, NPCs (apical progenitors) at the luminal surface of the telencephalon (rostral neural tube) undergo direct neurogenesis that generates neurons that migrate basally [76]. Later in developmental progression, the progenitor population expands via indirect neurogenesis, where NPCs give rise to subsequent intermediate progenitors (IPs, basal progenitors) [77]. Basal progenitors and outer radial glia divide symmetrically, allowing neuronal population amplification by forming two identical daughter cells or two immature neurons [76]. Indirect neurogenesis is critical for proper cortex size and correlates with hyperpolarization of apical progenitor cells (**Figure 4**) [76, 77]. Retinal expansion arises from 2 waves of neurogenesis (early and late) [78, 79]. In microcephaly in CZS, in addition to cell death, improper cortical development arises from a shift from indirect to direct neurogenesis [44]. As retinogenesis loosely follows two major waves, ZIKV-induced progenitor alterations underly microphthalmia and other macrostructural changes.

Early Human Retinal Developmental Signaling

Retinal Development

Retinal development is highly complex and protracted, requiring specific multifactorial timing for proper retinogenesis, making it exceptionally sensitive to insult, including viral infections. The most severe retinal consequences in humans result from early trimester infections that can alter or damage proper retinal development [80, 81]. Due to the complexity, retinal development has the highest metabolic expense of any tissue and requires a large oxygen delivery into the inner and outer retina from independent sources [82]. Retinal development occurs predominately between week 3-4 to week 32 but extends through the first year of life [80, 81].

Ocular tissues are derived from progenitor sources in the neuroectoderm, surface ectoderm, and periocular mesenchyme (POM, neural crest-derived). Early stages of eye field establishment at the anterior end of the neural plate are characterized by subdivisions orchestrated by retinoic acid signaling with specific expression patterns of BMP antagonists, FGF, and Wnt signaling. After neural tube formation and closure by embryonic day (ED) 22, the early eye field establishes the two bilateral eye primordia from neural cells within the optic groove, initiating the earliest ocular precursor structures. Within a few days, the eye primordia bud from the developing forebrain forms optic vesicles (ED24) that expand outward towards the surface ectoderm (SE) [80, 81]. As the optic vesicle contacts the surface ectoderm, Shh, TGF-B, and FGF signaling establishes distinct regions of the neuroepithelium as prospective RPE, NR, and optic stalk (OS) [80, 83].

By ED32, the OV has developed into the optic cup and the optic stalk, and the lens placode has established from dividing lens progenitors (previously derived

from a transient population of cells at the pre-placodal region of the surface ectoderm) [80, 81, 83-86]. The lens placode continues to differentiate, and morphogenic events during optic cup formation provide space for the lens pit and future lens development (ED33) [80, 83]. The lens continues to develop into the lens vesicle at fetal week (FW) 6, undergoing primary lens fiber formation from elongation of the posterior segment. Subsequently, secondary lens fibers form the clear part of the lens from the anterior segment, accounting for most of the lens bulk [86]. From the optic cup, the outermost region that encounters the SE becomes the prospective RPE, and the inner portion becomes the NR with an intermediate marginal zone (MZ) between them. The MZ is invaded by the inter-photoreceptor matrix (IPM) that is critical for RPE maturation and development that, by fetal week (FW6), has established the cuboidal RPE precursors that pigment as they continue to mature through FW10. The MZ becomes the future ciliary body, whereas the NR differentiates to form the remaining seven retinal cell types around FW26 (described below). Lastly, the OS forms a small optic nerve (ON) by FW 7 that, by FW8, becomes invaded by nerve fiber bundles, has organized, striated nuclear arrangements, and becomes sheathed [83-86].

Differentiation of the inner NR forms the seven remaining retinal cell types: RGCs, PR (cone and rod), HCs, ACs, MGCs, and BCs. Multipotent retinal progenitor cells (RPCs) form the remaining retinal cell types from asymmetric divisions of radial progenitor cells. Cell cycle phase and exit occur in distinct localizations as progenitors undergo nuclear migration during cell cycle phases where mitosis occurs on the apical side, and DNA synthesis occurs basally. Like

neurogenesis, early RPCs produce one terminally differentiated post-mitotic cell while maintaining the renewal of RPC populations. Late retinogenesis results in two terminally differentiated cells without self-renewal, causing the depletion of progenitor populations. The progenitors undergo nuclear migration within distinct phases of exit from the cell cycle, with apical mitosis and basal DNA synthesis [83].

Distinct Phases of Human Retinal Development and Expansion

Remaining retinal development occurs in two overlapping phases that can be loosely split into an early and late phase, like neurogenesis (**Figure 5**). Differentiation in the early phase starts with the differentiation of RGCs, then cone PRs, HC, and ACs before a late phase with rod PRs, MGCs, and finally BCs form (exact timing of structural organization discussed further in the next paragraph) [87]. For early-born RNs, progenitors can orient within the retina by moving along the radial axis (apical-basal) or by tangential migration perpendicular to the radial axis [83]. The tangential, early-born migration is similar to how early neurons of direct neurogenesis move, in general, compared to those arising later in brain development from indirect neurogenesis [76].

The inner NR differentiates to form the seven major cell types in distinct, overlapping patterns. First, early PR development is disorganized, with cone PR establishing at EW10 before rods at EW12. Although still disorganized, by EW 18, the RPE monolayer is well-defined with strong PR expression. Significant RN development occurs at EW18 as a disorganized GCL forms with an associated nerve fiber layer (NFL). Towards the end of EW18, the inner limiting membrane (ILM) is established at the base of MGC [88]. During EW19, the organization

continues with PR nuclei and cell bodies in the outer nuclear layer now facing toward the OPL [28, 89]. Around the same time, the outer and inner plexiform layers form as the future site for PR synaptic terminals and the MG basal lamina, respectively. At EW20, choroid development progresses with Bruch's membrane forming as the innermost choroid layer, and blood exchange starts to occur as choroidal capillaries meet the basement layering of RPE. During EW20, the inner nuclear layer begins to form from the cell bodies and nuclei of three neuronal cells: bipolar cells, horizontal cells, and amacrine cells, which are fully organized and established by EW24. The PR layer continues developing and organizing as apical PR projections align during EW21, and the PR outer segments (POS) fully align at EW28. Lastly, during EW32, the outer limiting membrane forms at the base of PRs, providing structural support to the retina [28].

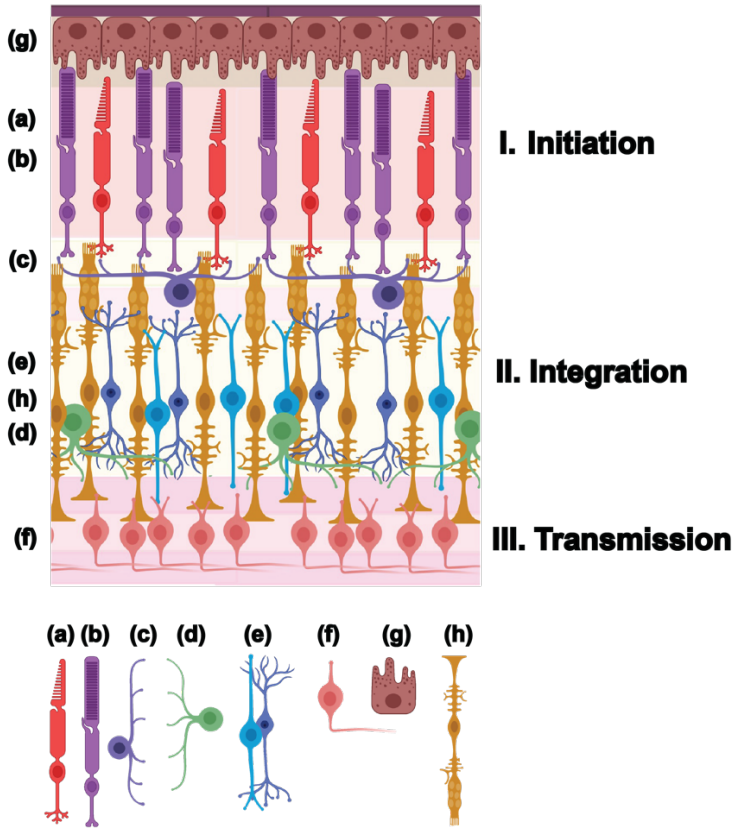


Figure 3. Human Retinal Structure and Phototransduction. The human retina is comprised of 6 neuronal and 2 non-neuronal cell types that function in concert for vision. **I. Initiation** of phototransdutction is with photoreceptors the light primary light sensing cells of the retina. They are classified as (**a**) highly sensitive rods used for nighttime vision and (**b**) cones responsible for diurnal color vision. **II. Integration** of visual stimuli into meaningful outputs involves deconvolution though retinal interneurons including (**c**) horizontal (**d**) amacrine, and (**e**) bipolar cells. **III. Transmission**. After integration, visual signals are transmitted through the long (**f**) retinal ganglion axons creating the optic nerve into the visual cortex. The two non-neuronal cell types play critical roles for supporting the retina. (**g**) The retinal pigment epithelium (RPE) is imperative for photoreceptor health and abrogating phototoxicity. (**h**) Müller glia cells support interneurons by physically by acting as a scaffold and regulating the chemical environment during neuronal firing. (Created in BioRender).

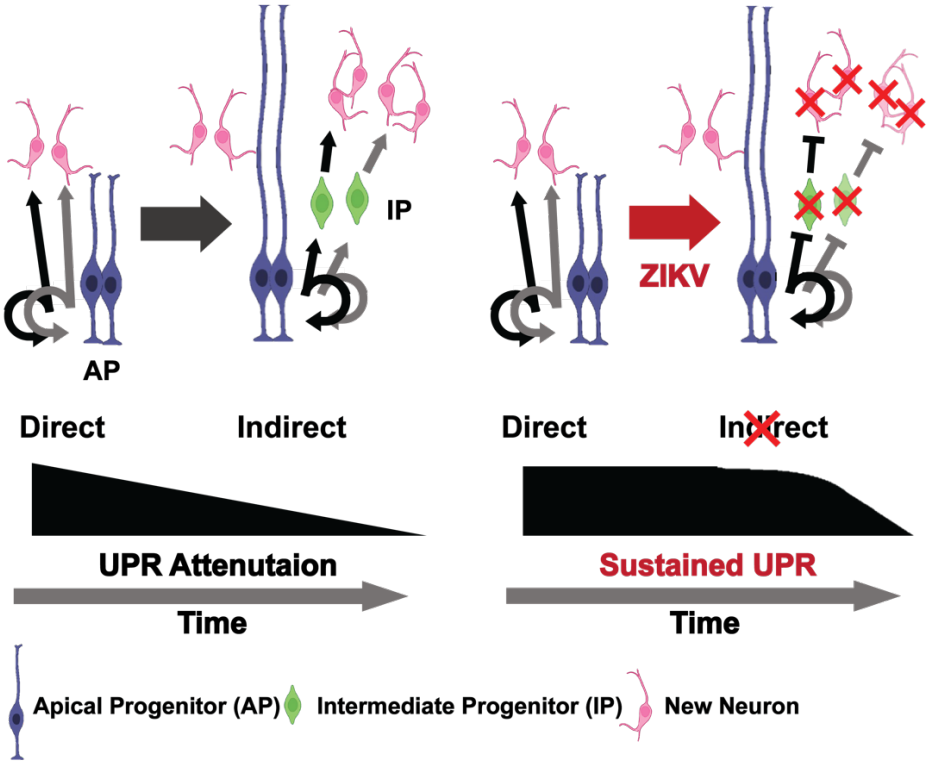


Figure 4. Model of how disrupted neurogenic UPR activity from ZIKV infection underlies microcephaly. Proper corticogenesis follows distinct phases of neurogenesis—early direct and later indirect neurogenesis—that are temporally regulated for proper corticogenesis (left). Directly differentiated neurons result from the asymmetrical division of apical progenitors. Subsequently, indirect neurogenesis results from the expansion of neural progenitors into intermediate progenitor populations before developing into projection neurons. Gradual attenuation of UPR signaling is indispensable for the transition from direct-to-indirect neurogenesis. (Right) During Zika viral infections high UPR activity persists, that, by restricting the neurogenesis transition undermines intermediate progenitor expansion, ultimately resulting in microcephaly. (Adapted from Alfano et al., *Front Cell Neurosci* 2019 [76]. Created in BioRender).

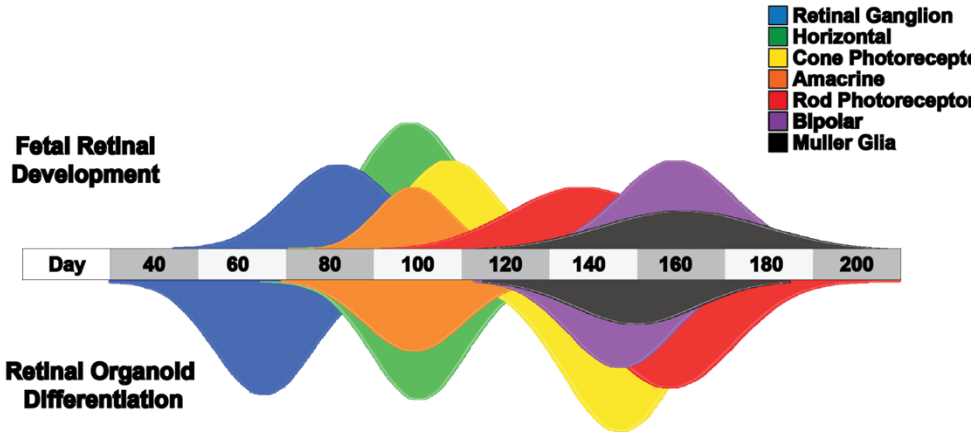


Figure 5. A schematic diagram of human retinal cell type generation and retinal organoid differentiation during in vivo development. Scaling follows days post conception (top) or differentiation day (bottom). Adapted from Kim et al., *Stem Cell Reports* 2023 and adjusted based on cited works in text.

V. ZIKV Receptors: the TAM Family

TAM Receptor Family

The TAM family (TYRO3, AXL, and MERTK) of receptors are receptor tyrosine kinases that maintain fundamental functions in multiple tissues. Structurally, TAM receptors have conserved kinase domains with extracellular domains with adhesion-like properties [90]. They contain a single-pass trans-membrane domain coupled to a competent protein-tyrosine kinase. Extracellularly, the structural modules for the TAM ectodomains are standard to other RTKs have a unique two-plus-two combination that mediates ligand binding through immunoglobulin-related domains [91, 92]. Proper TAM ligand requires binding through the specific cofactors Growth arrest specific factor 6 (Gas6) and Protein S

(Pros1). Characteristic of the numerous TAM functions, Gas6 and Pros1 have differential affinities to each receptor: Gas6 can bind all 3 TAMs having the highest affinity for AXL, whereas TYRO3 and MERTK are mainly targeted by Pros1 (Pros1 does not activate AXL). Usual downstream TAM signaling activates either the phosphoinositide 3 kinase (PI3K)/AKT pathway or cytokine receptor signaling via JAK/STAT, which, when activated, has a more vigorous response dominating PI3/AKT signaling [92]. Although uncommon, the TAM receptors and their ligands can have promiscuous heterodimerization. However, those events are poorly understood and likely lead to unknown noncanonical outputs with niche biological functions [91].

The TAM family of receptors has widespread expression throughout multiple tissues, most notably in reproductive, immune, and CNS. The TAMs provide trophic support for cell growth and proper immune system preservation [93]. Specifically, the primary role of TAM signaling, with their ligands Gas6 and Protein S, is utilized for phagocytosis of apoptotic cells and other fundamental cellular properties, including proliferation, survival, adhesion, migration, stabilization of clotting, and inflammatory cytokine release [90, 91]. Furthermore, although not essential for embryonic development, RTKs like TAMs have essential regulatory roles in developing and maturing nervous, vascular, reproductive, and immune systems, including ocular development (consistent with the regions targeted by ZIKV) [91, 94]. Thus, understanding TAM expression patterns is critical in contextualizing ZIKV infections, especially in the eye.

TAM Receptor Expression in the Eye

Retinodevelopmental TAM Expression

Ocular symptoms of CZS result from infections during developmental timing, making it critical to understand TAM expression for the susceptibility and targets of ZIKV. In developing retinas of human fetal samples at GW 10 and 12, IHC and single-cell RNA sequencing identified AXL expression in retinal progenitor cells on the neural retina with high expression in the neighboring ciliary marginal zone [94]. Although there is limited primary literature on TAM expression in human retinal and organoid samples, other modeling identifies strong candidate cell types requiring future investigation.

TAM Expression in the Retina

Within the retina are diverse expression patterns of the TAM receptors within unique cell types. Strong candidates for ZIKV binding can be distilled by interrogating single-cell profiling experiments with primary human fetal retinas and comparing those against retinal organoids [95, 96]. The Lukowski et al., *EMBO J.* 2019 database encompasses the pooling of 2 single-cell sequencing analyses from all cell types in the human neural retina from 12 donor eyes. The second dataset from Cowan et al., *Cell* 2020 included the separation of cell types between foveal and peripheral regions (combined into a single retinal dataset for analysis) from human primary retinas between developmental week 7-to-20, for peripheral n = 6 eyes (n = 96,708 total cells) and foveal from n = 5 eyes (n = 22,150 cells) from 3 independent donors [96].

A global overview of broad receptor expression across the retina and between cell types can be explored based on the percent of total TAM expression for the average of the three datasets. Generally, within the entire retina, TYRO3 has the highest overall level (50%), with lower expression for AXL (28%) and MERTK (22%). Differential expression of the TAM receptors in individual cell types provides an opportunity to investigate the distinct susceptibility potential for each. To summarize the highest receptor expression by cell type: (1) the percent of AXL expression is the highest for MGCs (74%), BC (43%), Cone PR (37%), and RGC (17%). The percent of MERTK expression is the highest for Rod PR (81%), BC (26%), and Cone PR (24%). TYRO3 expression is the highest for HC (88%), AC (86%), RGC (73%), and cone PRs (41%) (**Figure 6a**) [95, 96]. The unique TAM receptor expression profiles for each cell type support the differential mechanisms expected between highly specialized cell types.

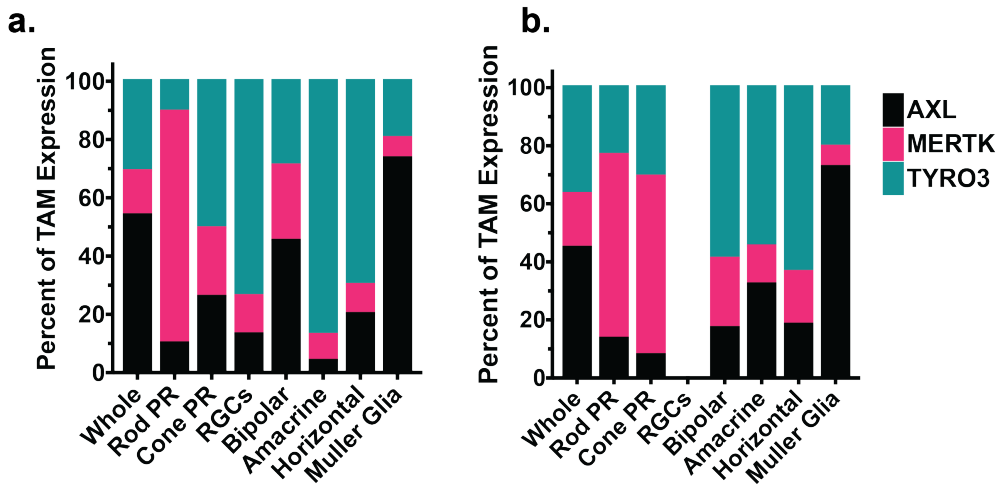


Figure 6. TAM receptor expression in fetal retina and retinal organoids. a. TAM receptor expression across the fetal retina (peripheral and foveal) and within retinal cell types. Percentages determined from the normalized TAM expression across 3 independent analyses in published datasets. **b.** TAM receptor expression in whole retinal organoids and individual cell types. No data are yet available for retinal ganglion cells. (See text [95, 96]).

VI. Neural Modeling of Zika Virus

Microcephalic Modeling of ZIKV

Effect of Zika Virus on Neurodevelopment

As mentioned previously, during the brain's neurodevelopment, new neurons arise from direct or indirect neurogenesis (**Figure 4)**. Early in mammalian cerebral cortex development, NPCs undergo direct neurogenesis that generates neurons directly before a second wave of indirect neurogenesis that supports boosting NPC numbers and proper cortical expansion [76, 97, 98]. Multiple forms of modeling

support ZIKV-causing microcephaly primarily by disrupting proper neurogenesis and cortical patterning through various mechanisms. Ultimately, infections of NPCs are implicated in microcephaly, although the underlying drivers for widescale mass loss are highly complex, extending beyond solely apoptosis. Changes to the developing brain result from altered NPC differentiation, cell cycle arrest, overall architectural disorganization likely from centrosomal depletion, abnormal mitoses, and changes to DNA replication and nonsense-mediated mRNA decay (NMD) [98, 99]. Strikingly, the modeling for microcephaly recapitulates clinical phenotypes remarkably well, facilitating the identification of specific cell types or pathways implicated in potential therapeutic targeting [100].

Organoids as a Model System

Human-derived stem cells have revolutionized the field of molecular biology by enabling the creation of organoids, three-dimensional structures that simulate human tissues, offering new insights into clinical and disease states. Under certain conditions, stem cells will self-organize into 3D aggregates and structures mimicking human tissues, known as organoids. The structure, complexity, and heterogeneity support the higher order of complexity and functions of a bona fide organ. Despite some limitations, organoids have unlocked many opportunities in cellular therapies, personalized medicine, drug discovery, and our understanding of genetic diseases. For organoid review, refer to Zhao et al., *Nat Rev Methods Primers* 2022 [101].

Organoids can be derived from many types of cells like iPSCs, adult or fetal cells (sperm, progenitors), or already differentiated cells. These cells form an initial

heterogeneous mixture of cells that are involved in specific biological processes like the digestive system (stomach, small intestine, colon, esophagus, pancreas, liver, tongue), respiratory system (lung), circulatory system (heart), and sensory system (ear, skin). The wide range of feasible starting materials is critical for recapitulating the expansive heterogeneity in systems and functions needed in organoids. Initial conditions and manual manipulations can predispose cell types into heterogeneous populations, driving precise differentiation signaling and resulting in complex organoids. Successful organoid generation hinges on a deep understanding of in vivo organ development, incorporating the essential elements of specific organogenesis into the process. Differentiation employs techniques like soluble factor addition or optogenetic activation, which mimic the spatiotemporal expression patterns of pathways during natural development, akin to the differentiation seen in traditional 2D stem cell cultures. However, the effectiveness of these techniques and the overall microenvironment are influenced by the distribution of physical cues, such as organoid size and the arrangement of cells. These physical aspects are critical as they can limit the complexity and size of the organoids, with inadequate nutrient supply, delivery, or waste removal leading to cell death. The delicate balance and interplay between physical and chemical signals within specific time frames pose challenges to reproducibility and efficiency in organoid culture. Nevertheless, increasingly refined strategies for standardizing conditions and homogenizing samples at crucial stages are improving the efficacy of organoid generation [101].

The cornerstone qualities for organoid quality and as a metric of differentiation efficiency are based on the generation and maturation of the proper cell types of that organ. Recapitulation of the functional characteristics of the respective organs, like accurate responses to external stimuli, requires effective transport or secretion of factors like cytokines [101]. In the case of ROs and the eye, mature ROs have photosensitive PRs with OS that can carry an electrophysiological potential [102]. Unfortunately, as of today, organoid differentiation cannot recapitulate the complete set of characteristic readouts, complexity level, and maturity achieved from true organogenesis. Organoid differentiation, occurring outside the body's hyper-specific contexts and spatiotemporal regulations, results in organoids lacking specific niches, cell types, architectures, or supporting systems. The major challenge for the widescale implementation of organoids comes from organoid-to-organoid heterogeneity, leading to batch effects compounding with high costs [101, 103]. The variability outside *in vivo* development is a critical limitation to controlling cellular, morphological, or size heterogeneity between ROs after initial formation.

Human organoids are a critical experimental intermediate between traditional mammalian models and advancements in studying human diseases, increasing therapeutic intervention efficiency and efficacy. The structure and cellular heterogeneity in organoids overcome the limitations of classic 2D cellular monocultures, as exemplified by brain organoids, where immune responses are critical for ZIKV and HSV1 infections and are not seen in 2D cultures [104]. Although individual organoids typically recapitulate only a subset of functions of a

complex system, advancements utilizing assemblies of distinct organoid types integrate unique properties between systems in a more natural association between retinal and cortical organoids cultured in suspension, enabling spontaneous generation of optic nerve-like structures while maintaining their distinct characteristics [105]. When organoid biology is combined with single-cell RNA sequencing, identifying the individual cell types implicated in viral infection and disease is possible [106].

Unfortunately, their use for large-scale drug and other screening assays is limited due to inter-organoid heterogeneity, which is compounded as organoid complexity increases. A significant contributor to organoid heterogeneity is multistep protocols requiring manual manipulation [103]. Standardizing organoid differentiation is a significant goal of the field. Identifying and integrating the myriad in vivo signals and contexts is a challenge for increasing organoid complexity and function, as in one case where tissue-specific ECM components were incorporated into the differentiation process. Refinement of morphogen timing and concentrations is beginning to address heterogeneity. Predominantly for screening and large-scale experimentation, there is a push to simplify organoid models, for example, through micropatterning and printing cells for those purposes [101]. Advances in organoids-on-a-chip, where the heterogeneity of organoids is integrated into a 2D chip, can reduce variability and other challenges facing 3D organoid culture. They have proven advantageous for compound screening throughput and sample homogeneity.

In some cases, Organs-on-a-Chip better recapitulates specifics of tissue microenvironments like media profusion that mimics vasculature, supporting a higher level of functional maturity [101]. Even with their limitations, the nascent stages of organoid biology are revolutionizing translational and stem cell biology, opening pathways for addressing new avenues of research. As organoid technology evolves, it will continue to catalyze a new wave of discovery.

Viral Modeling in Neural Organoids

A significant subset of organoid biology focuses on the nervous system, including organoid models for multiple brain and eye subregions. Terminal organs in the nervous system, like the brain and eye, are some of the most complex organs in the body. Advances into brain-and-retinal organoids (RO) have been revolutionary for studying viruses that target the nervous system, either developmentally, like with ZIKV, or adult-acquired like HSV1 or SARS-CoV-2. They offer insights into how viruses interact between multiple cell types and the interplay of those responses to organoid-specific functions, size, and architecture. Those features provide a route to an in-depth understanding of organ-and-cell-specific responses to viral infection, such as innate immune or proteomic stress response activation [107].

While retinal organoids remain somewhat underutilized for studying viral etiologies, brain organoids have been utilized to study a broad range of viruses, including flaviviruses (ZIKV, DENV), herpesviruses (HSV1), influenza (H1N1-WSN and H3N2-HKT68), coronaviruses (SARS-CoV-2), and enteroviruses (EV68 and EV71) [59, 104, 106, 108-115]. Notably, the prevalence of brain organoids in viral-

organoid modeling is critical for comparing pathologies between different viruses in the brain or for the same virus within other neural and non-neural organoid models.

Brain Modeling of ZIKV

Microcephaly commonly results from changes to NPCs expansion resulting from disruptions to the usual timing and pathway activation after ZIKV infection. In mice, in vivo targeting of NPCs affects brain development and directly targets multiple neuronal lineages. Targeting the early NPCs and radial glia, mainly in VZ and SVZ, ultimately leads to cortical thinning and loss of brain mass [98, 99, 116]. Human fetal samples emphasized human NPCs (hNPCs) targeting infection domains similar to those of mice, allowing windows into human-specific mechanisms [98]. Individually, differentiated hNPCs are heavily infected, exhibiting characteristics for driving microcephaly, like the inhibition of NPC differentiation through cell cycle arrest and apoptosis [98, 117]. One of the best ways to study early embryonic brain development in vitro is by complementing human-derived neurospheres with brain organoids representing the earliest stages and brain organoids mimicking the gene expression and patterning of a first-trimester fetal neocortex. A significant driver of microcephaly is caused by altered neurogenesis waves leading to the depletion of neural progenitor cells (NPCs) required for proper cortical expansion [44, 118]. Congruent with neural development, brain organoid development involves the immense expansion of different progenitor populations. As with clinical microcephaly, early 3D neurospheres and differentiating brain and cerebral organoids are heavily impacted by ZIKV infection, paralleling microcephalic profiles. Infected neurospheres, similar to the early stage of conglomerated neural

stem cells (NSCs), have disrupted morphology, a 40% loss of growth area, and low survival [114]. ZIKV targets and disrupts NSCs in brain organoids, again attenuating growth and mass specifically through a dual-factorial mechanism where proper neurogenesis is disrupted by cell cycle disruptions and inducing cell death [104, 112]. Those phenotypes extend to cerebral organoids, where the reduction of NSCs is caused by innate TLR3 activation and perturbations to axonal guidance, differentiation, neurogenesis, and apoptosis [115]. The interface and success of modeling ZIKV and HSV1 in brain organoids set the stage for expanding organoid modeling of the ocular pathologies in clinically relevant retinal neuronal cell types in ROs.

In conclusion, mouse models have high fidelity for recapitulating the specific patterning in microcephalic brains in CZS that are supported in human-derived cell types. There is the direct loss of proper NPC differentiation and indirect [98] impacts from disruption of the supporting cell types that, in combination, cause the neurogenesis and synaptogenesis loss seen in microcephaly. Although similar cell types are targeted between the two, a complete understanding of the interplay between cell types and mechanisms requires higher-complexity human-derived modeling, like brain organoids.

Ocular Modeling of ZIKV

Animal Modeling of Ocular ZIKV Infections

Mouse modeling is vital for understanding ocular tropism in response to ZIKV, although the ocular structure is highly variable to humans (especially rod and

cone ratios). Short-term infections highlight potential cellular targets and infection pathways, identifying the potential susceptibility of Müller glial cells (MGC), astrocytes, photoreceptors (PR), and the optic nerve and retinal ganglion cells (RGC) [25, 52, 119]. Long-term infections mimic the clinical ocular pathologies, with posterior uveitis and focal RPE defects [25, 31, 52]. Protracted infections highlight significant losses to cone PRs and RGCs after infection (60-70 dpi), likely partly due to dysfunction of the support from RPE and MGC (35). The outer nuclear layer (ONL), where PR nuclei organize, had focal degeneration from infection, PR loss, and RPE defects [25]. ZIKV infiltrated the optic nerve (ON) by 7 dpi with caspase activation in the nerve fiber layer and INL peaking at 9 dpi [25, 31]. Other mouse models suggest that viremia targets RGCs and the INL directly, with thinning of the OPL [31]. In total, mouse modeling parallels the clinical observations in that ZIKV targets the support networks of the eye in the RPE and MGC, with prolonged infections targeting RGCs and ultimately causing atrophy to the cone PRs and RGCs or the optic nerve (ON), suggesting infection of supporting cell types if not direct targeting [4, 15, 47].

In a limited capacity, other animals have been used in retinal experiments. Other small rodent models used to study ZIKV pathologies and production in the eye include Guinea pigs and Syrian hamsters [120, 121]. The only non-human primate studies use the pigtail macaque monkey. In utero, ZIKV delivery in macaques results in modeling similar to intraplacental transmission from the mother to the fetal eye [122].

In conclusion, although immune suppression is required, mouse models have high fidelity for recapitulating the specific patterning in microcephalic brains in CZS supported in human-derived cell types. There is the direct loss of proper NPC differentiation and indirect impacts from disruption of the supporting cell types that, in combination, cause the neurogenesis and synaptogenesis loss seen in microcephaly. Those features hold in more closely related mammals. However, the interplay between cell types and mechanisms in a human context requires higher-complexity human stem cell-derived modeling, like brain organoids.

Variability in Ocular Structure Between Model Organisms

In addition to the mouse modeling discussed extensively, when challenged with ZIKV, a wider range of mammalian models result in viremia in the eye. Other small rodent models identifying ZIKV pathologies and production in the eye include Guinea pigs and Syrian hamsters [120, 121]. The pigtail macaque monkey is the closest in similarity to *in vivo* human modeling because of the ability to introduce ZIKV *in utero*, which then manifests in the fetal eye via intraplacental transmission [122]. Macaques are valuable models due to their close relationship to humans, not only in terms of development but especially with the similarity to the *in vivo* human infection mechanism. The fidelity of pigtail macaques for modeling ZIKV infections as they are natural hosts, as are Rhesus macaques, the host to the original of ZIKV isolation [1, 123].

The persistent challenge underlying experiments in any system outside bona fide humans is the massive interspecies variability in retinal and ocular structures' size, cell type variabilities, and ratios. That variability is exemplified by focusing on

mammals with the most-to-least similar visual acuity to humans: humans, marmoset monkeys, macaque monkeys, mouse. Although humans are genetically more closely related to the Old World Macaques than New World Marmoset monkeys, marmosets have a visual acuity comparable to humans [124]. The human eye size is ~24mm in diameter, marmoset ~15mm (5/8), macaque ~20.4mm (85%), and 4mm (16.67%) for mice [124, 125]. The retinal size follows similar trends with 40mm, 20mm, and 5mm for humans, marmosets, and mice [124]. Primate vision and retinal composition are very similar to humans. Humans and macaques both exhibit trichromatic red-green-blue vision. In contrast, all male and some female marmosets have dichromatic vision (red-green colorblindness), as do all mice [124, 126]. Surprisingly, the subclassifications within each cell type are similar in mammalian and non-mammalian animals, although the limited literature on signal integration and transmission is not necessarily conserved [124].

Human-Derived Retinal Stem Cell Models

Traditional models (like mice, zebrafish, and chick) have been crucial for understanding the retina and retinal disease. However, they lack the unique structures of the human eye and have significant shortcomings in recapitulating human disease. Furthermore, early retinal development during gestation is challenging to study. Thus, additional novel methods are required for studying human retinal development and diseases that have the potential for therapeutic intervention for progressive vision loss, amongst others. The primary models using human-derived materials are dissociated primary tissue, explanted primary tissue, retinospheres, and stem cell-derived retinal organoids.

Dissociated Retinal Cultures

Dissociated retinal cultures are from primary (post-mortem or fetal) retinas. When plated on a culture dish, a monolayer of retinal cells maintains the diversity of retinal cell types, including rods and cones, BCs, HCs, ACs, MGCs, and RPCs. Dissociated retinal cultures offer the advantage of preserving RGC survival in vitro. When derived from fetal retinas from stages GW6-GW13, these cells are highly expandable, allowing the purification of cell types with low representation in the retina or that lack directed differentiation protocols. These properties are highly advantageous for large-scale drug screening due to the expansive capacity and isolation of single-cell types in dissociative cultures [127]. Unfortunately, as 2D cultures, they lack the structural context and lamination of the eye and have low fidelity for long-term cryo-storage. Additionally, the cell type ratios change with extended culture as the propensity for proliferation is unique between cell types.

Retinal Explants

Retinal explants originate from the dissection of primary retinas cultured after being laid flat onto a filter submerged in media. Unlike dissociation, explants maintain the cell type composition and retinal structure, making them highly advantageous for studying retinal degenerative diseases. Similar to dissociated cultures, these rely on the availability of retinas and the ability to dissect them rapidly post-mortem. After dissection, fetal retinal cells proliferate faster than adult cells. The higher replication rate, in turn, causes disorganization during long-term culture that is not seen in adults. The small number of samples, in combination with

considerable individual variability, makes study fidelity difficult when relying on dissected retinas [127].

Retinospheres

Retinospheres (RS) are closest to ROs structurally. They are a relatively easy way of culturing human retinal tissues in 3D. Primary fetal retinas are cut into small pieces or completely dissociated before low-adhesion culture for spontaneous spherical formation. As they condense, the cells self-organize into an INL supporting an encasing photoreceptor layer. Similar to 2D dissociated cultures, a large amount of retinospheres per retina can be generated by dividing a single retina into many pieces. Compared to the previous methods, they can be grown for long periods in culture while faithfully recapitulating fetal retinogenesis. During long-term culture, RSs maintain lamination and organization and support robust photoreceptor growth and outer segment maturation, but RGCs are rapidly lost. Other non-neural cell types, such as microglia, can be present and maintained. These are particularly useful for studying genetic diseases targeting retinal development as they can be derived from diseased or healthy patients with genetic variability. Furthermore, they maintain the potential for genetic engineering to support the correction or mitigation of clinical manifestations. RSs, unfortunately, do not offer the same capacity for large-scale screening due to the lack of availability and a mire of controversy behind fetal tissue harvesting [127].

Human Retinal Cell Modeling of ZIKV

Within the eye, CZS includes both structural and visual transduction anomalies. Structurally, clinical manifestations primarily target the retina, optic nerve, and retinal vesicles, commonly including macular findings of focal pigmentary mottling and chorioretinal atrophy, and those of the optic nerve like hypoplasia, cupping, and atrophy, amongst others [4, 15, 24, 119]. The retina must be highly organized and accurately connected for phototransduction initiation and integration through the optic nerve with proper craniofacial muscle operation for proper vision. The brain must also be conducive to higher-order visual processing. Therefore, visual impairment can arise from either developmental deficit targeting the structure or phototransduction of the retina, oculomotor tissues, or visual processing in the brain—our focus on the most severe retinal consequences from early trimester infections. From the clinical symptomology, the primary cell types targeted are retinal progenitor cells (RPCs), retinal ganglion cells (RGCs), Müller glia (MGC), and retinal pigmented epithelium (RPE) [24, 128, 129].

The variability between structural or visual manifestations of CZS likely results from distinct cell-specific infection and response profiles. The high incidence of chorioretinal lesions and the impact RPE dysfunction has on the developing eye suggests that RPE infection underlies the more dramatic macrostructural retinal phenotypes. Additionally, visual transduction deficits could be caused by the direct targeting of retinal neurons (like RGCs) or indirectly by the loss of MGC support. In support of this, RPE infected with ZIKV have time-dependent increases in viral titer, whereas MGCs, although permissive, do not. The persistent infections in MGCs could affect visual transduction disruptions as they support the retinal neurons

involved [25, 130]. As with glial cells in brain modeling, active Müller gliosis is a sign of stress from ZIKV infection, which can further damage retinal neurons, including PRs [25, 131]. The nuances between cell types for driving unique phenotypes may have immune involvement seen by the bimodal immune activation between RPE and MGCs having an immediate transient immune activation (as with retinal pericytes) [25]. A proper understanding of how the responses change within each cell type in the context of each other emphasizes the need for complex models to study ZIKV in the eye.

Blood-Retinal-Barrier Modeling of Viral Entry

Immune privilege is critical for maintaining the health of the highly sensitive retina. Therefore, ZIKV must overcome this and immune surveillance to establish infection. Privilege is maintained through 2 epithelial barriers: the outer blood-retinal-barrier (oBRB) comprised of RPE or the inner blood-retinal-barrier (iBRB) with retinal microvascular endothelium. Initial ZIKV entry must occur from the bloodstream during systematic infections, into the BRB disrupting the tight junctions, and into the retina for further dissemination. Cell types from both barriers are permissive to ZIKV and likely play unique roles in infection, supporting multiple potential mechanisms. In the oBRB, RPE and choroidal epithelial cells (CECs), and in the iBRB, retinal endothelial cells (RECs) and retinal pericytes (RPs) of the iBRB are infected by ZIKV [5, 25, 52]. For the iBRB, ZIKV infects RECs through retinal capillaries, leading to amplification through RPs into the inner retinal bed for further dissemination through the retina. In the oBRB, infection through CECs to RPE leads to massive deposition of ZIKV into the proximal retinal bed [132]. Upon infection,

RPs have an immediate (transient) immune activation lasting around eight days, whereas, in RECs, the activation is delayed until 8 dpi [128, 132]. TAM receptor expression in RPE and cells of the BRBs and the modulation and interplay with ZIKV infections are discussed in depth above. Differential response and receptor expressions may underly some of the variability of ocular symptoms in AZI. Effective dissemination through tight barriers, including the blood-brain, testicular, and placental barriers, is a hallmark of this ZIKV epidemic and supports conserved mechanisms within cell type classes, as could occur across neuronal-derived precursors [5, 133].

Studying infections in human-derived models that recapitulate the context of multicell-type interactions is imperative. Studies using monocultures of retinal cell types have revealed that nearly all cells in the retina are permissive to ZIKV. Although there is differential infectivity between them, the list of susceptible retinal cells includes RPE, retinal pericytes, retinal vascular endothelial cells (HRvEC), choroidal endothelial cells, MGC, rod photoreceptors (PR) [5, 15, 25, 52, 128, 130]. Unfortunately, there are some limitations to these models. 2D retinal cell cultures often require immortalized cell lines with altered pathways or are a single cell type that does not recapitulate the interplay between cell-type-specific infection trajectories. Although better, even co-cultures of retinal cells lack the 3D context of a retina. Murine models are out of the context of human development and have retinas with dramatically different compositions and structures than humans. They have a higher rod: cone ratio to humans (33-35:1 opposed to 20:1) and higher PR densities but lower peripheral-to-macular cellular distribution gradients [134-136].

Modeling in mice also requires immunosuppression or lines without an immune response for proper disease progression, eliminating heavily implicated and interconnected pathways from other responses. Thus, this thesis uses an alternative model to study ZIKV effects on the eye—human stem cell-derived retinal organoids.

Retinal Organoids (ROs) as a Model of Viral Infections

Retinal Organoids

Significant advances have been made in human visual stem cell biology in the last decade. Retinal organoids are a recent exciting development in that human stem cell-derived 3-dimensional cultures of retinal cells contain all major retinal cell types and mimic proper retinodevelopmental timings [102, 127, 137]. There is a drastic need for ROs due to sparse availability and a rapid degeneration rate of primary retinas, amongst other roadblocks. The complex nature of retinal development is routinely achieved by providing a series of different media, adherent, and suspension cultures and specific microdissection of specific neural retinal regions (**Fig 7**). Dissected neural retina regions will self-laminate in suspension, forming immature, stage 1 ROs containing an outer layer of RPCs at day 60 that will mature into ROs with mature, externally facing photoreceptors with defined outer segments that are physiologically active by day 160-200 [102, 103, 127, 137]. ROs show a significant, multifaceted promise for exploring the nuances of development, developmental and degenerative disease modeling, regeneration, and virology [127]. AAV vectors have been shown to infect multiple cell types in

ROs at high efficiency, allowing for the dissection of individual genes and pathways responsible for retinopathies [138]. Unfortunately, they are plagued by the same pitfalls as other organoids—they are expensive due to prolonged differentiation times for proper retinogenesis and the inherent variability of manual dissection, which leads to heterogeneity between individual organoids and differentiations—limiting their effectiveness and reproducibility for large-scale experimentation [103]. The utility of ROs will continue to increase as dissection-free protocols are refined. Although currently limited to ZIKV and SARS-CoV-2, RO's recapitulation through the developmental cascade holds promise for pursuing viruses targeting developing and adult retinas [129, 139].

Our studies followed the traditional differentiation in a modified protocol from Zhong et al. to generate ROs in a clinically relevant context of ZIKV pathologies (see **Figure 7** and **Materials and Methods**) [102].

Retinal Organoids (ROs) as a Model of Viral Infections

Retinal Organoids

Significant advances have been made in human visual stem cell biology in the last decade. Retinal organoids are a recent exciting development in that human stem cell-derived 3-dimensional cultures of retinal cells contain all major retinal cell types and mimic proper retinodevelopmental timings [102, 127, 137]. There is a drastic need for ROs due to sparse availability and a rapid degeneration rate of primary retinas, amongst other roadblocks. The complex nature of retinal development is routinely achieved by providing a series of different media,

adherent, and suspension cultures and specific microdissection of specific neural retinal regions (**Fig 7**). Dissected neural retina regions will self-laminate in suspension, forming immature, stage 1 ROs containing an outer layer of RPCs at day 60 that will mature into ROs with mature, externally facing photoreceptors with defined outer segments that are physiologically active by day 160-200 [102, 103, 127, 137]. ROs show a significant, multifaceted promise for exploring the nuances of development, developmental and degenerative disease modeling, regeneration, and virology [127]. AAV vectors have been shown to infect multiple cell types in ROs at high efficiency, allowing for the dissection of individual genes and pathways responsible for retinopathies [138]. Unfortunately, they are plagued by the same pitfalls as other organoids—they are expensive due to prolonged differentiation times for proper retinogenesis and the inherent variability of manual dissection, which leads to heterogeneity between individual organoids and differentiations—limiting their effectiveness and reproducibility for large-scale experimentation [103]. The utility of ROs will continue to increase as dissection-free protocols are refined. Although currently limited to ZIKV and SARS-CoV-2, RO's recapitulation through the developmental cascade holds promise for pursuing viruses targeting developing and adult retinas [129, 139].

Our studies followed the traditional differentiation in a modified protocol from Zhong et al. to generate ROs in a clinically relevant context of ZIKV pathologies (see **Figure 7** and **Materials and Methods**) [102].

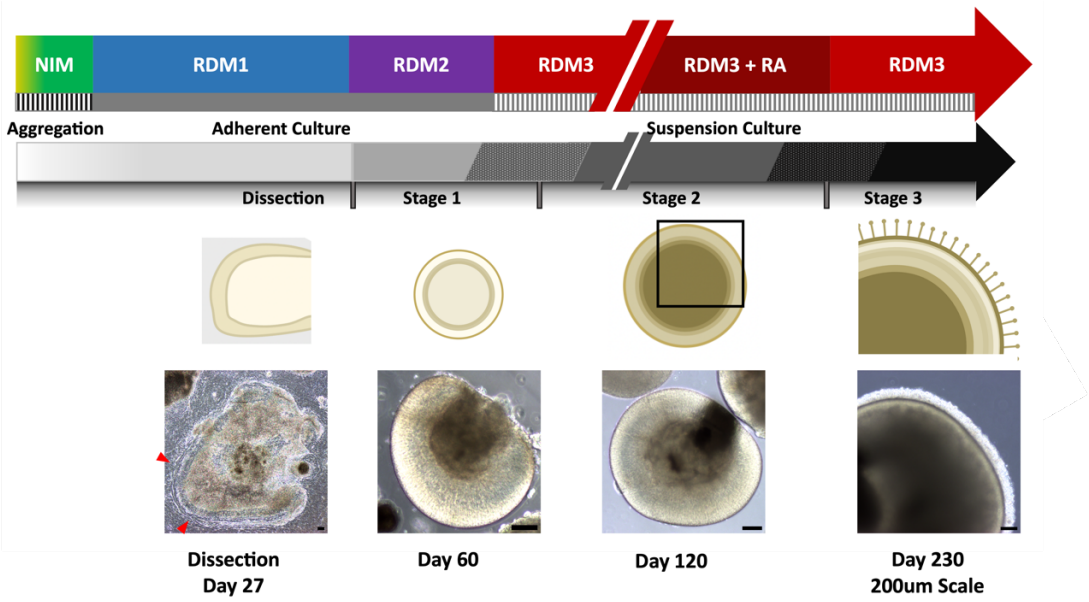


Figure 7. Retinal organoid (RO) differentiation. Briefly, dissected stem cells are cultured in neural induction media, forming aggregated embryoid bodies before seeding for adherent culturing. Adherent cultures are maintained in retinal differentiation media 1 (RDM1) until manual enrichment of neural retina regions at day 27 (arrows). Dissected domains self-laminate in RDM2 suspension culture forming stage 1 ROs dominated by retinal ganglion cells (RGCs) and retinal precursor cells (RPCs). Transitionary Stage 2 ROs contain developing photoreceptor precursors (PRP), bipolar cells (BC), and other retinal interneurons, with a diminishing population of RGCs. Continued differentiation in RDM3 produces stage 3 ROs with Müller glia cells and photoreceptor (PR) maturation. As maturation continues, PRs specify into rods and cones with functional outer segments. The specific days for imaging are day 27, day 60, day 120, and day 230. Scale Bars 200µm. (RO differentiation protocol is adapted from Zhong et al., *Nat Commun* 2014 [102]. RO stages are adapted from Capowski et al., *Development* 2019 [137]. Created in BioRender).

Timing of Cellular Differentiation in ROs

Order of Cell Types Generated

The complex nature of retinal development is achieved through adherent and suspension culture with microdissection of specific neural retinal regions, forming immature ROs containing an outer layer of RPCs. Those RPCs differentiate,

forming all major cell types of the retina in a proper sequential manner (early and late phases; early RGCs, cone PR, HC, and AC cells, or late phase rod PRs, BCs, MGCs) that will ultimately develop mature PRs with outer segments (OS) [87, 102, 137, 140]. RO differentiation can be described in three stages: Stage 1 with RPCs in the outer layer and formation of some inner RGCs; a disorganized Stage 2 with GCL breakdown and development of PRs, HCs, and ACs from RPCS; and lastly, a highly organized Stage 3 with robust MGC expression with the formation of an outer limiting membrane underlying mature PR that form outer segments [102]. Given the progression in differentiating contextualized human retinal cultures, ROs are becoming increasingly valuable for studying aging and developmental diseases of the eye [87, 102, 137, 140].

One of the enormous advantages of ROs is that they will generate all retinal cell types over time between initial RPC formation and mature photoreceptors closely following *in vivo* retinogenesis. As the RPCs differentiate, the major cell types of the retina are produced sequentially, paralleling the 2 major waves of in-utero retinal development, making them groundbreaking for studying early human retinal development. As with those disrupted by ZIKV in neurogenesis, retinogenesis follows 2 major waves—an early and a late phase. During normal retinogenesis, the early phase produced RGCs, cone PR, HC, and AC cells. In contrast, rod PRs, BCs, and MGCs appear in the late phase, ultimately developing into a highly structured retina with mature PRs with outer segments (OS) for light sensitivity. RO differentiation can be described in 3 parallel stages to retinogenesis (**Figure 5 *bottom***). Stage 1 ROs are around day 40-60 (similar to FD59-FD82), with

RPCs in the outer layer and the formation of some inner RGCs, HCs, and ACs. There is a disorganized Stage 2 from day 70-110 (FD82-125), where the ganglion cell layer begins to break down as immature (cone) PRs, HCs, and ACs form. Lastly, there is a highly organized Stage 3 with robust MGC expression with the formation of an outer limiting membrane from day 120-175 (FD125) followed by the rods and cones specification. Outer segments form on PRs after day 175+ (FD163+) [87, 102, 137, 140]. PR differentiation in ROs is particularly robust, producing rods and cones with similar morphologies to in vivo rods and cones capable of light responsiveness [127]. Unfortunately, ROs have a longer differentiation time than other human retinal cell models. ROs generation can be heterogeneous and complex because microdissection variability during adherent culture increases over long culturing periods. Even so, given their prolonged maturation and parallels to in-utero retinogenesis, ROs are becoming increasingly valuable for studying aging and developmental diseases of the eye [87, 102, 137, 140].

One of the significant challenges in retinal modeling is efficiently deriving RGCs. RGCs can survive past 4 weeks if isolated from dissociated fetal retinas, ROs, or some directed differentiations. Although a majority degenerate, ROs sustain RGCs for the longest compared to all other human retinal models extending over 100 days. In cases where RGCs are provided with non-retinal neuronal targets, their survival can be extended over 6 months. Unfortunately, RGCs are not consistently maintained in long-term RO cultures, with most dying through stage 2. RGC loss leads to the progressive degeneration of the INL, laminar loss, and

disorganization of its associated cells (HCs and ACs), making ROs a subpar model for studying retinal interneurons. The high diversity of RGCs produced allows an all-encompassing scope for understanding mechanisms behind RGC differentiation and disease modeling [127].

ROs are a potent tool for studying diseases of the human retina within a more physiologically relevant model. A significant strength of ROs is that they are differentiated from embryonic or iPSCs. Starting from those cells allows the creation of stable cell lines with genetic changes that can correct disease mutations in patient lines or create those same mutations in control lines, maintaining the ability to produce ROs for certain diseases to be studied broadly. This approach facilitates the intervention transition for either a conserved mutation across diseases or for creating personalized therapeutics. Genetic engineering has also been a critical tool for understanding when, how, and how efficiently certain cell types are produced in ROs or within the developmental context through fluorescent reporters for cell-specific genes (like RAX or VSX2 for RPCs) [127]. Cumulatively, ROs have created buzz with their potential for patient-specific treatments for genetic diseases, immune rejection in broader treatments, and for modeling other retinal stressors like impact damage or viral infections.

VII. Single Cell RNA Sequencing

Overview of Single-Cell RNA Sequencing

One of the major challenges in biology is untangling the nuances between the complexities of cell types and pathway interactions. Ideally, the goal is to identify

distinct differences between individual cell types in response to specific signals. Those nuances are lost in the averaging process in routinely used bulk assays. Original methods were limited to studying specific, known proteins by FACS. Recently, advancements in single-cell analyses have unlocked a way to study expression patterns of protein, RNA, or DNA at the single-cell level [141, 142]. With single-cell RNA sequencing (scRNA-Seq), the individual variability between cell types and states, like cell cycle, immune responses, and bystander priming, can be clarified [141-143]. The averaging in bulk sequencing is exceptionally detrimental when investigating intracellular components with a small percentage of protein expression in the cell [143]. scRNA-Seq now allows deconvolution between cell variability and the detection of RNA, which is a minute percentage of the cellular macromolecular totals. As scRNA-Seq can address a wide range of challenges within biology, the research method used, and the questions that can be investigated are evolving. It has been revolutionary across biology, especially for cancer, stem cells, epigenetics, immunology, and virology, and is being used now to tackle many long-standing questions [141].

As a global overview of scRNA-Seq, a population of cells must be isolated into single cells to be processed into an interpretable set of data points where complex clustering and analysis are possible. The physical isolation of individual cells for sequencing was overcome with manual or automated single-cell isolation methods. Additionally, limited biological material (0.1 pg of mRNA per cell) needs extensive cDNA amplification before the library preparation and sequencing. Finally, discrimination of actual cell-to-cell variation from the noise caused by many factors

has been addressed by developing analysis tools and pipelines dedicated and optimized for these datasets [142]. Those pipelines all contain a specific series of steps to create the final dataset: 1. reprocessing to organize and focus the data, including quality control and read trimming. Mapping to a reference genome, and 3. the refined data must be further processed downstream to properly normalize reads for gene expression before further analysis is utilized to identify heterogeneous gene expression patterns and cluster cells into subpopulations. Initial clustering based on cells with similar gene expression profiles subdivides groups based on cell-type characteristics or functional classifications. Although the generalized pipeline follows a specific series of steps, multiple techniques are specialized to address the variation in experimental approaches. The adaptation and specialized pipelines utilized between clustering methods exemplify the complexity involved. From the conventional clustering methods such as principle component analysis (PCA), hierarchical clustering, or K-Means, newer, novel methods (like, amongst others, the Sincell R Package) refine obscure and confounding effects while identifying cellular subgroups at higher power and with fidelity [142]. These techniques enable greater specificity for identifying rare cell type populations without regression of the broader cell classes identified with other methods [103]. s these pipelines refine and evolve, so will the throughput capabilities and questions that can be interrogated.

See Rato et al., *Virus Res* 2017, for an in-depth review of single-cell RNA sequencing [142].

Single-Cell RNA Sequencing in Virology

scRNA-Seq has emerged as a critical technology for investigating single-cell susceptibility to viral infection and responses, unlocking the ability to investigate challenging biological questions previously constrained by high costs and requirements for large sample sizes with tedious, time-consuming processing. Those advantages for the field of virology exemplify the advantages impacting biology overall. Foremost is the heterogeneity in viral infection profiles and particle fidelity, lost or diluted to an insignificant or undetectable percent of cellular totals when averaged in bulk assays [141]. Historically, methods addressing differential expression or cell type-specific susceptibility to infection were labor intensive, only applicable to a subset of viruses, and focused on host genes, as opposed to viral host interactions or the virus themselves [142, 143]. More recently, knockdown and knockout genetic screening based on RNA interference or CRISPR editing are the primary methods for understanding viral-host interactions. Unfortunately, they lack an understanding of many highly interconnected variables that can affect the susceptibility of a cell to support viral infection, the capacity for viral replication, and the fidelity of viral progeny.

scRNA-Seq can reveal the specific, inherent aspects of cellular heterogeneity impacting those based on differentiation state, cell cycle stage, differential host and immune responses, or cell type [141-143]. One of the underlying drivers is cell size, as larger cells have a higher replicative capacity and may contain additional resources (most proteins and mRNA) for conducting biological reactions, larger organelles, or a higher stress threshold [143, 144]. FMDV and Vesicular Stomatitis

Virus (VSV) exemplify this, where there are fluctuations in RNA level from cellular heterogeneity impact the replicative efficiency and viral production of viral progeny, leading to FMDV RNA level fluctuation, such as in cells at the G2/M phase of the cell cycle [141, 143]. Together, the interplay between the consequences of host response activation and their roles in the efficacy of viral progeny have implications for understanding how individual cell types or pathways disrupt proper replication or maturation and for tracking the evolution of viral progeny through successive rounds of replication [53, 57, 61, 142]. s single-cell sequencing techniques have evolved, they have been utilized as a blanket approach for directly measuring viral host interactions of intracellular viruses, creating a complete global snapshot of gene viral-host interactions for many viruses, including influenza A virus (IAV), poliovirus, foot-and-mouth-disease virus (FMDV), Zika virus (ZIKV), and Dengue virus (DENV) [142]. Unfortunately, spatial resolution is lost during dissociation to a single-cell level, which can be exceptionally detrimental when addressing cell-type infection profiles and pathway activation in the context of the infection in a given tissue or organ, as would occur with an expanding bystander effect in response to a virus.

scRNA Sequencing in Retinal Organoids

scRNA-Seq has been applied to study many organoid systems. It facilitates an in-depth characterization of developmental pathways, differentiation dynamics and trajectories, divergences in disease contexts, and cell types present and their change over time. cRNA-Seq is revolutionary for understanding how culture media manipulation influences organoid development and, by proxy, insight into *in vivo* organs while avoiding the limitations of primary tissues [145]. Applying scRNA-Seq

in organoid systems has resulted in identifying rare or novel cell types and driven the understanding of how inter-organoid heterogeneity recapitulates bodily organs or their development in intestinal, lung, liver, brain, kidney, and pancreatic organoids. cRNA-seq also has been integral to deconvolute variability and intricacy in modeling complex diseases like pancreatic ductal adenocarcinoma (PDAC) cancers or diseases of the brain in organoids [87, 94, 146]. n retinal modeling, it has been critical to understand retinal organoid (RO) heterogeneity and how they compares to the human retina [96, 147]. Comprehension of retinal differentiation and the order of cell generation over time in ROs has been facilitated by pseudo-time analysis, allowing comparisons to *in vivo* retinal development [96, 148]. Together, these established retinal cell type atlases, allowing for the centralization of the current status of the field [96, 147].

In this thesis work, we aimed to understand how ZIKV infects the human RO system and the consequences of that in primarily infected cells compared to the bystander cells, primarily using scRNA-Seq in combination with immunohistochemistry. The work presented in Chapter 2 establishes human ROs as a valid model for studying ZIKV infection. Chapter 3 evaluates cell type-specific changes in gene expression in response to ZIKV infection using scRNA-Seq. In both Chapters, we also present comparative data using HSV-1 infections as proof of concept. Chapter 4 interrogates the role of the unfolded protein response (UPR) in ZIKV infection, a stress response uncovered in the scRNA-Seq study. Finally, Chapter 5 expands on another area of cellular response, innate immunity through the interferon system, uncovered by the scRNA-Seq studies. The scRNA-seq led us

to evaluate the effect of treating ZIKV-infected ROs with interferon. Collectively, this work solidifies the use of Retinal Organoids as a powerful model to study viral infection and disease and provides essential insights into the ocular pathology and eventual therapeutic interventions of ZIKV infection.

Chapter 2. Human Stem Cell-Derived Retinal Organoids Recapitulate Zika and HSV1 Pathophysiology

Summary

The investigation into viral infections' impact on the human retina faces a critical challenge due to the absence of physiologically accurate models. This study introduces stem cell-derived retinal organoids (ROs) as a novel approach to analyzing the ocular effects of Zika virus (ZIKV) and herpes simplex virus 1 (HSV1). We demonstrate that ROs, particularly in their immature state, effectively replicate the severe pathogenic characteristics of ZIKV observed in early trimester in-utero infections, impacting retinal progenitor and ganglion cells and hindering organoid development. The inhibition of the AXL receptor markedly reduces ZIKV infection, establishing its pivotal role in viral entry into the human retina. We further extended our investigation to include exploration into HSV1 infections using mature ROs. This virus caused extensive damage to photoreceptor and Müller glial cells. These results validate the use of retinal organoids in closely mirroring the clinical progression of retinal viral infections, offering a significant advancement in the study of ocular pathogenesis.

Introduction

Clinically, ocular phenotypes of CZS manifest mainly as optic nerve (ON) atrophy and chorioretinal malformations [31, 119]. One of the challenges is the limited prevalence of physiologically relevant models for human clinical infections.

Although current use is minimal, the efficacy of human retinal organoids (ROs) for studying ocular targeting viruses has been demonstrated for AAV vectors in gene editing, SARS-CoV-2, and ZIKV [129, 138, 139]. The complexity and 3D structure of ROs are critical contexts for understanding how ZIKV can differentially infect and transmit between certain cell types or discerning the potential mechanisms underlying the diversity of retinal pathologies. Within infected ROs, the broader pathways activated or suppressed by ZIKV can be understood at a higher order and within the context of how specific cells initiate and propagate those responses. There is a differential expression of ZIKV receptors between cell types [96]. However, the precise roles of those receptors for ZIKV entry in the human retina remain unknown (see Chapter 1). The variability in TAM receptor expression between diverse cell types in ROs allow critical insight into the differential susceptibility within the complexity and heterogeneity in the retina.

Viral infections of the human eye have been limited due to a lack of an experimental model. For example, Herpes simplex virus type 1 (HSV1) is one of the most commonly circulating viruses worldwide. A member of the Alphaherpesviridae, HSV1 is a 100-110 nm diameter dsDNA virus encapsulated by an icosahedral capsid and spiked envelope [149]. Typically contracted in childhood, 50-80% of adults in the US, or about 2/3 of all people worldwide, are infected with HSV1 [150-152]. HSV1 is usually transmitted by direct contact with saliva, establishing typically asymptomatic primary infection in epithelial cells before establishing latency in the dorsal root ganglia before reactivation (DRG) [149, 152]. Upon lytic reactivation, symptom presentation for HSV1 is usually in the form of cold sores or blisters on the

lip. In rare cases, it can also infect the eye [150, 151]. Eye infections are usually nonspecific, with eye pain, redness and watering of the eye, and light sensitivity, although in rare cases, can lead to significant visual impairment [152, 153]. In about 1 in 1.6-2 million people, HSV1 reactivates in the retina, causing acute retinal necrosis (ARN) [154]. ARN is a rapid response to an acute retinal HSV1 infection that triggers widespread inflammation in a mature retina, leading to quick and dramatic retinal necrosis and often detachment [155, 156]. Historically, ARN and retinal HSV1 infections were modeled in chicken embryos and, more recently, with mouse subretinal injections [157, 158]. HSV1 tropism and infection profiles in human retinal stem cell models are unknown.

We used immature and mature ROs to model different pathologies between ZIKV and HSV1. ZIKV infections were modeled in immature ROs matching the cell types and timings of early *in-utero* infections, resulting in the most severe pathologies. Because of the severity of HSV1-related ARN in adults, we used mature ROs with PRs containing outer segments for modeling the adult retina (**Figure 1**).

The retinal organoid work presented would not have been possible without the training and support from Dr. Vignesh Nadar, Dr. Mohamed Faynus, and Mika Katsura. Joseph Melgoza was integral in RO fluorescence imaging by establishing paraffin embedding, processing, and marker stain optimization protocols. Zachary Aralis performed HSV1 infections as part of his dissertation work [159].

Results

Human Stem Cell-Derived Retinal Organoids and Pigment Epithelium Efficaciously Model Zika Virus Infections

First, to demonstrate the efficacy of ROs for studying ZIKV, they were grown to day 60 before infection with ZIKV at an MOI of 1. The permissiveness of ROs was analyzed in viral supernatants at 24, 48, and 96 hpi, and ZIKV titer increased over time (**Fig 2a**), as determined by focal assay. Subsequently, to confirm viral entry and demonstrate infection dynamics within the 3D, multicellular context of an RO, we performed immunohistology (IHC) staining against ZIKV NS2B in RO sections over 96hpi. Consistent with the increase in viral titers, there was an expansion of ZIKV-NS2B signals over 96hpi. Within that is establishing sites of ZIKV infection on the RO periphery by 48hpi, penetrating through multiple nuclear layers by 96hpi (**Fig 2b**; secondary control **Suppl. Fig 1a**). To confirm active ZIKV replication in day 60 ROs, IHC was performed against the J2 dsRNA antibody to identify double-stranded replication intermediates and through the morphology of NS2B staining. In day 60 ROs, J2 staining is highly associated with NS2B by 96hpi (**Fig 2c;** secondary control **Suppl. Fig 1b**), paralleling the increase in NS2B infection progression (**Suppl. Fig 1c**). Formation of perinuclear replication factories is a hallmark of ZIKV propagation and was observed in day 60 ROs by perinuclear NS2B localization at 48hpi and with J2 colocalization and 96hpi (**Fig 2c** and **Suppl. Fig 1d**).

Macular alterations dominate ocular manifestations from later, second, and third-trimester infections, although less frequently than earlier, other structural defects occur [24, 48]. Both the proper infection timing and the presence of retinal components can be modeled by the older ROs and human stem cell-derived RPE. The susceptibility and permissiveness of mature organoids to ZIKV remain unknown. To further evaluate the ability of ROs for modeling later trimester infections, the susceptibility was determined by IHC of NS2B in sections of day 112 and day 200 infected (MOI 1) ROs demonstrating localizations through multiple areas of unique morphology and penetrating deeper regions of the RO suggesting multiple cell types infected (**Fig 2d**; secondary control **Suppl. Fig 1e**). One such case is the heavily infected regions in areas of cells sharing an RPE-like morphology across all time points (**Suppl. Fig 1f***).

Next, to determine the susceptibility and permissiveness of stem cell-derived RPE, monocultures of RPE were infected at an MOI of 1. RPE susceptibility was demonstrated by IF for ZIKV envelope protein at 48hpi staining with disruption of the highly structured actin from phalloidin staining (**Fig 2e**; left inset is structured, right disrupted). These actin disruptions in RPE are apparent in lower magnification imaging (**Suppl. Fig 1g**; secondary control **Suppl. Fig 1h**). Permissiveness of stem cell-derived RPE is seen by the large increase in FFU over 96 hpi from supernatant tittering (**Fig 2f**). These results demonstrate the efficacy of human stem cell-derived ROs and RPE in modeling aspects of ZIKV pathophysiology through different stages of retinal development.

AXL is a Primary Receptor in Retinal Organoids and Pigment Epithelium

The TAM family of receptors, specifically AXL, has been reported to be one of the primary host factors facilitating ZIKV infection in human cells. AXL expression occurs in the early retina, RPCS, RPE, RGCs, and MGCs [94-96].

To investigate the role of AXL in ZIKV infections of human stem cell-derived models, we pretreated ROs with an anti-AXL function-blocking antibody (R&D Systems AF154) at 0.1 mg/mL for 1 hour prior to ZIKV infection at an MOI of 1. Inhibition of infection in day 60 ROs was demonstrated through tittering 30hpi supernatants by a considerable reduction of ZIKV titers in anti-AXL treated ROs over IgG controls (**Fig 3a**). We performed an IFA on whole mounted day 60 ROs for AXL and NS2B from the same conditions, determining a reduction of ZIKV in anti-AXL treated samples with limited AXL staining present (**Fig 3b;** secondary staining **Suppl. Fig 2a**). To examine if RO susceptibility and mediation through AXL is maintained across cell types and differentiation state by tittering supernatants at 48hpi from IgG and anti-AXL antibody treated ROs at days 60, 112, and 200. Susceptibility in ROs is demonstrated with ZIKV production in IgG-treated samples of all ages. The efficacy of AXL inhibition was maintained as titers were reduced for AXL-inhibited samples at all time points, although it may proportionally reduce with age (**Fig 3c**). As the likelihood of RPE increases with RO age, we wanted to determine RPE contributions to later-stage ROs by repeating the AXL-inhibition experiments in RPE. Titers of 48hpi supernatants are reduced by about half in AXL-treated samples compared to IgG (**Fig 3d**). This data validates AXL as a primary

receptor in human stem cell-derived retinal modeling with immature ROs and RPE, bolstering the current understanding of receptor selectivity in human retinal models.

Zika Virus Infects Retinal Precursor and Ganglion Cells in Immature Retinal Organoids

Two primary cell types implicated in severe structural and visual defects are retinal progenitor cells (RPCs) and retinal ganglion cells (RGCs). Both are present within a heterogeneous, 3D population in day 60 ROs. After demonstrating RO permissiveness to ZIKV (Figure 1), we aimed to investigate the role of individual cell types in pathogenesis. Individual cell-type infections were established by IHC staining for cell-specific markers and ZIKV NS2B in RO sections at 24, 48, and 96hpi (MOI of 1). First, ROs stained for the RGC marker SNCG demonstrating early ZIKV penetration into the *expected SNCG+ internal RGC regions by 24hpi and infection throughout at 96hpi (**Fig 4a**) and is supported with vimentin costaining (**Suppl. Fig 3a**; secondary controls **Suppl. Fig 3b**) [137]. When the percent of all SNCG+ nuclei is quantified against NS2B, nearly all SNCG+ cells are infected at 96hpi, dramatically increasing from 17.8% to 84.4% between 48 and 96hpi (**Fig 4b**). Subsequently, immunostaining for the RPC marker VSX2 demonstrates sites of infection establishing within the expected peripheral VSX2+ rim at 48hpi, further disseminating radially by 96hpi (**Fig 4c**; secondary control **Suppl. 3c**). When quantified, VSX2+ increases stepwise from 18.7% at 48hpi to 39.6% at 96hpi (**Fig 4d**). Similar trends are seen in flow cytometry on dissociated ROs at 30 and 96 hpi (**Suppl. Fig 3d**). When measured against the 7.6% to 42.6% of all cells infected at 48 and 96hpi, the difference in infection profile between the two is stark as VSX2+

profiles match all cells, whereas SNCG+ RGCs were significantly higher by 96hpi (**Fig 4e**).

One of the significant drivers of microcephaly is a change in neural progenitor fate from ZIKV infection. As reductions in global eye and optic nerve size are prominent in severe cases of ocular CZS, we investigated how ZIKV infection impacts the implicated RPCs and RGCs in the canonical published localizations by quantifying the percent of cells that were positive for VSX2 or SNCG+ within or excluded from ZIKV infection a 10% region of the total image (VSX2+ images with representative ROIs in **Suppl. Fig 3e**). For VSX2, the percent of all cells in uninfected samples is 76%, consistent at around 75% for uninfected regions in both 48 and 96hpi samples. In contrast, the percent VSX2+ with regions positive with NS2B declines significantly stepwise from 54% to 34% VSX2+ positive at 48 and 96hpi (**Fig 4f**). Unlike VSX2, the percent SNCG+ regions within NS2B+ ROIs has not significantly dropped by 96hpi, suggesting ZIKV underlies a loss in progenitor fate (**Suppl. Fig 3f**). In sum, ZIKV readily infects both RGCs and RPCs in day 60 ROs while potentially causing a loss in progenitor fate.

Zika Virus Attenuates Retinal Organoid Growth Causing Severe Pathogenesis

Due to the prevalence of microphthalmia and other ocular growth or expansion-related manifestations, we investigated the impacts of protracted, 2-week ZIKV infections of day 60 ROs at a lower 0.1 MOI. Initial investigation with white light imaging reveals that although the shape changes, uninfected morphology remains consistent morphology with a tight outer barrier and nerve fiber layer

integrity, unlike ZIKV+ ROs with condensation of the NFL at 3dpi into a darkening collapse of RO structure by 14dpi (**Fig 5a**). These impacts are dramatic, as emphasized at higher magnification by destruction and disintegration of the tight outer edge with a change in cellular morphology indicating cell death (**Fig 5b**). To quantify the impacts of ZIKV on organoid growth, we measured the 2D surface area based on the outside rim of individual ROs across 2 weeks, revealing significantly higher growth in uninfected samples by day 6, with an average 14-day growth of 55% against an only 17% for ZIKV-infected samples (**Fig 5c**).

Initially, we sought to understand the impact of infection on RO health by measuring the metabolism change over 2 weeks with alamarBlue (AB). On average, the uninfected samples have higher AB fluorescence at 14dpi, suggesting better health, supported by a tightening in variance between ZIKV+ samples that support cell death (**Suppl. Fig 4a**). Next, whole ROs were bathed in Hoechst and PI to determine if cell death underlies size and metabolomic decreases. 14dpi ZIKV-infected ROs have drastically more PI-positivity seen with a higher proportion of red, PI-staining and significantly more quantified in about 47% of infected against 8% from uninfected samples (**Fig 5d,e**). 14-day ROs were sectioned and stained for cleaved caspase 3 to examine the role of programmed cell death in the ROs. At 14dpi, there is more cleaved caspase staining and significantly higher quantified fluorescence units in ZIKV-infected ROs over uninfected (**Fig 5f**,**g**; secondary staining **Suppl. Fig 4b**). ROs were pretreated with the pan-caspase inhibitor Z-VAD FMK (ZVAD) and the necrosis inhibitor Necrostatin (Nec1s), and treatment was sustained over the two weeks of infection to clarify the mechanism of cell death. BF

imaging and long-term growth quantifications were highly variable, but a significant drop in alamarBlue fluorescence for infected mock, ZVAD, and Nec1s treated samples, suggesting no significant rescue (**Suppl. Fig 4c-e**). These data demonstrate that ZIKV has long-term consequences for RO growth, with cell death as at least one underlying mechanism.

HSV1 Tropism is Recapitulated in Mature Retinal Organoids

HSV1 can reactivate in the retina, with acute infections triggering rapid and severe responses in the adult retina leading to ARN with detachment and death [155, 156]. To determine the susceptibility of older, day 113, and day 180 ROs to HSV1, they were challenged with 15,000 pfu/RO. Phase contrast imaging against HSV1-US11-GFP in day 113 and 200 ROs, heavily permissive to HSV1 with multiple foci of infection by 16hpi (**Fig 6a,b**; **Suppl. Fig 5a**) Uninfected and an additional HSV1+ day 118 ROs. In the time course of HSV1 infection in day 180 ROs, there are rivers of HSV1-US11-GFP into the deeper regions of the RO by 16hpi with GFP expression encompassing the entire RO at 24hpi and with a collapse of overall RO structure at 48hpi (**Fig 6b**). Permissiveness was established through focus forming assay of RO supernatants at 8, 16, and 24hpi, demonstrating high susceptibility to HSV1 with production by 8hpi and a sharp increase in titer from 16-to-24hpi (**Fig 6c**). Next, to determine the susceptibility of individual cell types within the complexity of the RO, we sectioned and stained day 180 ROs at 24hpi for specific cell type markers. Firstly, IHC against the MGC marker vimentin demonstrates that HSV1 infects MGCs by 24hpi as demonstrated by the overlap of HSV1-US11-GFP and vimentin (**Fig 6d**; secondaries **Suppl. Fig 5b**). Subsequently,

although diminishing by day 180, IHC for SNCG+ RGCs suggests that RGCs are highly susceptible to HSV1 as it penetrates the internal RGC-containing regions (**Suppl. Fig 5c**). Lastly, IHC for Opsin, a marker for the other primary cell type present photoreceptors, and HSV1-US11-GFP demonstrates that PRs are susceptible to HSV1 by 24hpi (**Fig 6e**). ROs with visible PR outer segments were infected with HSV1 at 15,000 pfu/mL and tracked over 24 hours to confirm PR infections. By 8hpi, initial infection establishes with GFP expression in the OS rim, expanding to multiple puncta by 16hpi. By 24hpi, GFP has expanded through multiple layers of cells with unique morphologies (**Fig 6f**; additional imaging set in **Suppl. Fig 5d**). In summary, maturing ROs are susceptible and permissive to HSV1, with infection perpetuating into all cell types, including RGCs, MGCs, and PRs, with infection establishing amongst PR outer segments.

Discussion

These data demonstrate the efficacy of ROs to model 2 viruses of different classes in parallel, ZIKV and HSV1. We found that ROs at multiple stages of differentiation are permissive to ZIKV and HSV1, and cell types infected match viral tropism. ZIKV infections demonstrate that RPCs and RGCs in ROs and stem cell-derived RPE are susceptible to ZIKV. We found that the AXL receptor is necessary for ZIKV infection in ROs at all stages and in the RPE. HSV1 infections in mature ROs highlight that PRs, MGCs, and RGCs are susceptible to HSV1.

This study validates the power of retinal organoids to model ZIKV infections through a range of differentiation points and developmental windows. A recent report by Contreras et al., *Viruses* 2023, identified that retinal stem cells could be

infected on days 19 and 29 in organoidotypic culture. Our modeling in further maturing day 60 ROs bolsters the cell-type preferences and tropism of more developed in-utero infections. The later-stage interface between stage 1 and stage 2, day 60, is a point that is exceedingly promising for ZIKV modeling as they are reminiscent of early retinogenesis and the establishment of implicated retinal neurons (like RGCs). At that stage, they are reminiscent of higher severity first trimester infections, containing the major cell types implicated in ZIKV infections (including RPCs and RGCs) [102]. We show for the first time that the infection of human cell-derived RGCs alone or within a heterogeneous population with other known targets (RPCs). Throughout RO differentiation, RPCs give rise to multiple neuronal cell types across differentiation time, suggesting varying intermediate progenitor populations. Paralleling Contreras et al., *Viruses* 2023, we found that ZIKV readily infects RPCs in older, day 60 ROs that likely have unique transcriptional profiles compared to earlier-stage progenitors. Our work is the first report of decreases in RPC populations at ZIKV-infected regions congruent with the changes in neural precursor cell fate in brain organoids [44]. However, the specific mechanism of fate in ROs remains elusive.

Our work bolsters our knowledge of ZIKV infections in ROs and expands them into HSV1 modeling. Although extensive characterization was conducted only at day 60, the efficacy extends to late-stage ROs. Future work is needed to determine the susceptibility of all retinal cell types. Furthermore, this work presents further evidence that stem cell-derived RPE are highly permissive and susceptible to ZIKV, congruent with previous studies that harness primary RPE (prRPE) by

Roach and Alcendor, *J Neuroinflammation* 2017 [132] and Singh et al., *JCI Insight* 2017 [52], fetal RPE by Contreras et al., *Viruses* 2023 [129], or stem cell-derived RPE by Simonin et al., *EBioMedicine* 2017 [128]. In infected RPE, we saw disruptions to the usually organized actin cytoskeleton, congruent with results in stem cell-derived RPE and Sertoli cells, responsible for the blood-testicular-barrier (BTB) by Strange et al., *mBio* 2019, where interactions between F-actin and ZO-1 (tight junction marker) were reduced with BTB loss [128, 160]. In addition to independent RPE cultures, we noted ZIKV-infected regions with RPE morphology in ROs of all stages, thus expanding our understanding of the differential susceptibility of RPE in the context of other neural retinal cells out to day 200.

Although considered an undesirable cell type in ROs, those regions are likely infected. The morphology and ZIKV staining in the presumptive RPE of day 200 ROs (Suppl. Fig 1e, 96hpi*) are strikingly similar to AXL staining in RPE and the neural retina of primary fetal cortices. Further analysis of older samples to confirm RPE identity and ZO-1 tight junction loss from infection will corroborate morphological findings and further elucidate the interplay between RPE and neural retinal pathologies. Even though ROs have RPE, it provides an imperfect way to begin modeling the complexity in different developing regions. Combinatorial modeling between RPE and ROs would naturally encompass that, and by differentiating both from the same stem cell line, the impact of cell line variability would be reduced. This method could also increase RO differentiation time, as seen by co-cultures by Akhtar et al., *Stem Cell Res.* 2019 [161]. In U2OS cells, the

vimentin and cytoskeletal networks organize around ZIKV replication complexes [162]. One such advantage of joining RPE and RO for how infection progresses and reshapes complex architecture is combining those bridges our results for intense vimentin co-staining in ZIKV-infected ROs at all ages with the changes in the actin cytoskeleton from infection in RPE.

Worsening ocular consequences based on the timing of in-utero infection suggest receptors, permissiveness, and viral replication capacity change with developmental age. Contreras et al. reported higher levels of ZIKV replication in day 29 retinal cell cultures over day 16. Our work suggests that replication levels are higher at day 120, with similar overall levels at day 60 or 200. Unfortunately, a high degree of variability in organoid composition and limited replicates muddles those results. The most likely cause of those discrepancies is the level of RPE contaminants, as our data and those by Contreras et al. both support a higher replicative capacity in RPE over ROs (from independent experiments). Shared results between our groups for different age ROs support that viral capacity changes with RO age, although the exact mechanism remains elusive. Future experiments with more organoids with a low level of RPE will bolster our understanding beyond these datasets.

Further, our work demonstrates AXL as a primary receptor in stem cell-derived ROs of multiple differentiation windows and stem cell-derived RPE. Modeling across these windows is critical for pushing our understanding of differential infection mechanisms between reservoirs and even progenitor cell types. In cerebral organoids and NSCs, genetic ablation of AXL does not protect them

from infection [163]. In contrast, antibody inhibition (AF154 R&D Systems) in Sertoli cells of testicular organoids inhibited ZIKV infection [160]. Previously, within ocular cell types, the specificity of AXL for viral entry in RPE has been demonstrated with a near complete ZIKV inhibition in prRPE by Singh et al., *JCI Insight* 2017 after inhibition with the AXL R428 (APExBio) inhibitor [52]. For our experiments, we chose to utilize antibody inhibition of AXL to coat against initial binding on the cellular surface as R428 inhibits the catalytic activity of AXL, and inhibition for prRPE was at 1 uM (IC50 14 nM). Foremost, day 60 ROs. Our work has furthered the support of AXL as a primary receptor in stem cell-derived RPE as, even after 2 hours of antibody inhibition of AXL (AF154, R&D Systems), ZIKV titer remained 44% lower than IgG controls after 48hpi even without replacement of antibody post-infection, supporting previous work. The presence of heavily infected RPE regions on all age ROs and the intense level of AXL inhibition in those ROs with AXL-containing media replacement further support AXL as the primary receptor. Repeating RPE inhibition experiments with congruent experimental approaches to RO studies would confirm that.

Overall, this work compounds previous modeling supporting AXL as the primary receptor in human retinal cultures across cell types and differentiation states. Although RPE cultures are at different infection timelines, the lowest proportion of inhibition is in RPE and day 200 ROs. One possible explanation is that there is a shift in TAM receptor profiles during development and maturation, allowing incomplete inhibition from shifting receptor profiles, cross talk, or other alternative infection mechanisms. An analysis of the role of other TAM components

in ZIKV infection is also unknown. Individual and multiple knockout or inhibition experiments for Gas6 upstream of AXL and the other two TAM receptors, MERTK and TYRO3, will be able to determine the effect of each on ROs and RPE of different points of differentiation. Although not ocular cells, preliminary results with an anti-Gas6 inhibiting antibody demonstrate potent ZIKV inhibition in H4 cells (a neuroglioma cell line) (**Suppl. Fig 2d**).

Our work is the first application of ROs for modeling the long-term consequences of viral infection resembling severe ocular consequences of CZS, such as shifts in eye growth and macrostructural changes. Like brain organoids, a significant advantage of utilizing ROs is their growth phases, such as early retinal expansion. As in brain organoids, we have demonstrated long-term growth deficits and induction of cell death with cleaved caspase 3 expression in ZIKV-infected ROs [104]. Unfortunately, individual pan-caspase or necrosis inhibition did not help rescue the consequences of infection. One explanation could be that overlapping cell death induction pathways result in overwhelming inhibition; therefore, dual inhibition may be required, as demonstrated in other models [164]. Alternatively, cell death may be only one facet of growth deficits.

Microcephalic models demonstrate that the loss in neural expansion is from altered progenitor fates, but the role of shifting progenitor populations in retinal modeling is unknown. Our data supports the loss of progenitor fate over 96 hpi, demonstrating a potential role in long-term infections. Future tracking of VSX2+ levels over 14 dpi with a VSX2+ reporter would untangle some of the interplay with cell death. Even with the loss of progenitor fate, there is no indication of the new

fate from that altered state. From a VSX2+ reporter, RPC populations can be isolated from dissociated ROs and infected. The altered differentiation cascade could be determined by tracking the cell fates from sorted VSX2+ and VSX2 negative populations from infected samples over time. One of the factors underlying the shift in NPC fate is cell cycle delay and dysregulation. Altered NPC fates and impacts on growth can be attributed to translational arrest from cell cycle exit, leading to decreased neuronal differentiation [114]. A fluorescent ubiquitination-based cell cycle indicator (FUCCI) reporter system to track cell cycling phases in long-term infected ROs would resolve another axis of variability underlying ocular consequences. Lastly, it would be fortuitous to adjust either the infection level or timetable in subsequent experiments, as 14dpi at an MOI of 0.1 may have overwhelmed the capacity of ROs to sustain ZIKV infection.

Figures

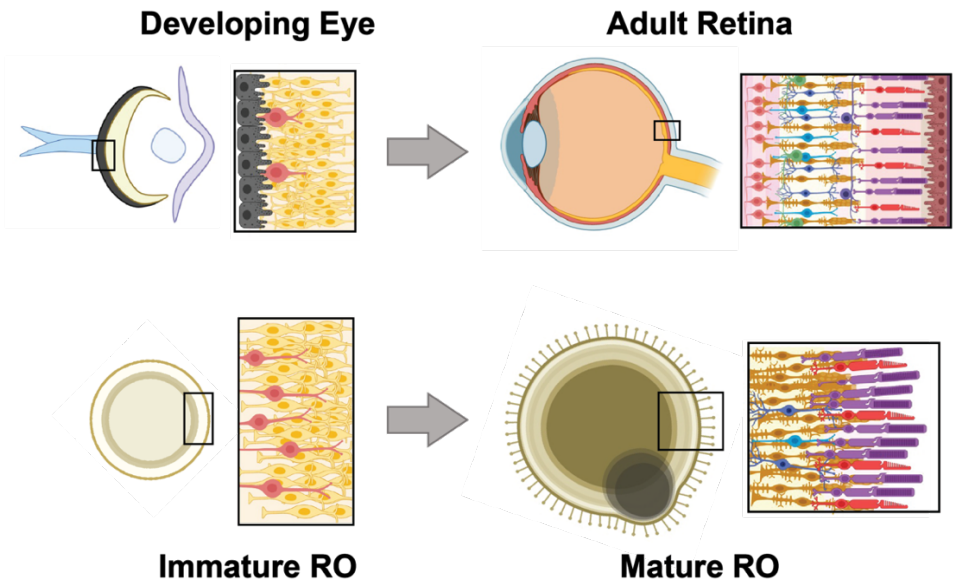


Figure 1. Day 60 and Day 200 ROs Mimic Developing and Adult Retinas. Early retinal development and organoid differentiation have similar cell type compositions. Early developing retinas are comprised of RPE, RGCs, and RPC whereas day 60 ROs are dominated by RGCs and RPCs, excluding RPE. The cell types present in the adult retina parallel those of mature ROs. Adult retinas are highly ordered with light-responsive rod and cone PRs associated against RPE. Day 200 ROs contain MGC with light responsive rod and cone photoreceptors. Other generated cell types atrophy in internal structures. (Created in BioRender).

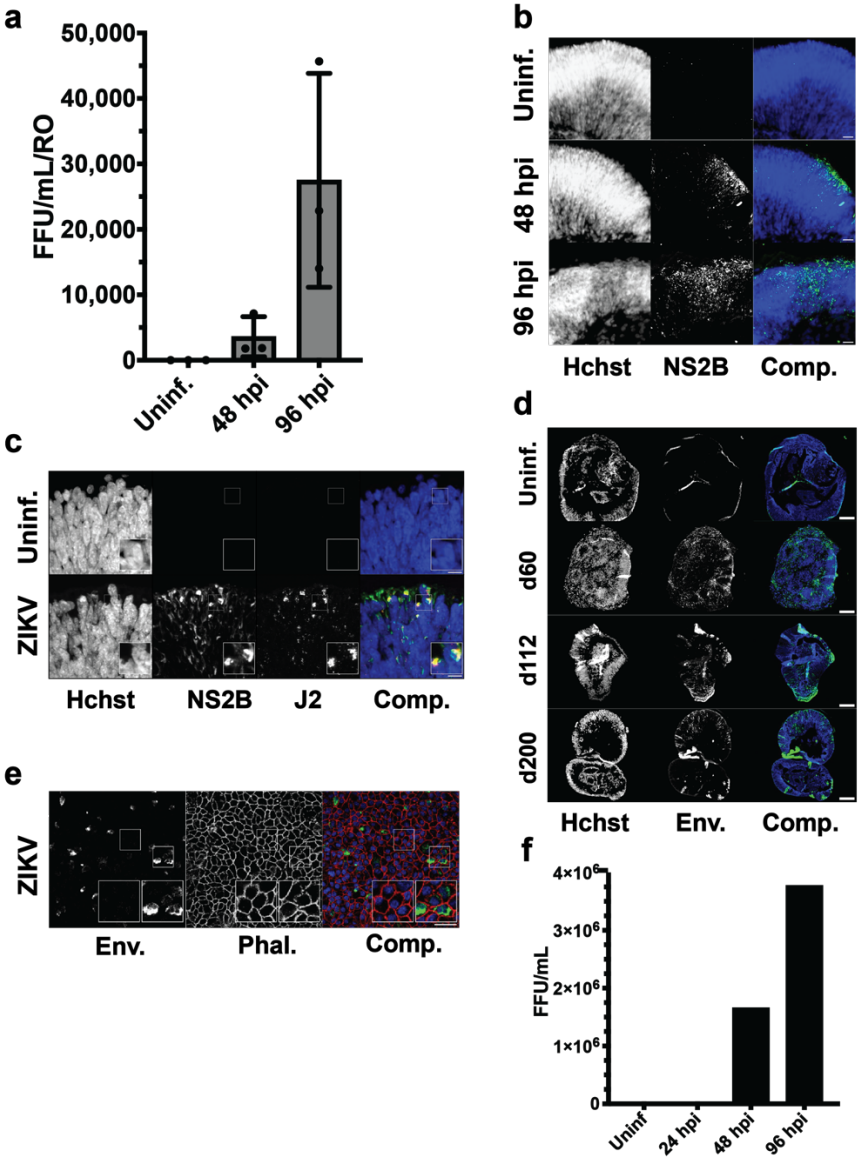


Figure 2. Human Stem Cell-Derived Retinal Modeling Recapitulates ZIKV Infections. a. Analysis of ZIKV titer from uninfected or 48 and 96 hpi day 60 ROs by focus forming assay (n=3 from 9 ROs). **b-d.** Immunohistochemistry staining for the ZIKV protein NS2B alone in day 60 ROs at 48 and 96 hpi (**b**, 20μm scale bar), with J2 dsRNA staining in day 60 ROs at 48 hpi (**c**, 10μm scale bar), and alone at 48hpi in day 60, 112, and 200 ROs (**d**, 400μm scale bar). **e.** Immunofluorescence staining for ZIKV envelope and phalloidin at 48 hpi in stem-cell-derived RPE. 40um scale bar. **f.** Analysis of ZIKV titer in uninfected, 24, 48, or 96 hpi RPE supernatants

by focus forming assay (n=1). All ZIKV infections were at an MOI of 1. Nuclei staining for all IHC is with Hoechst 33258 other than *DAPI for 1e.

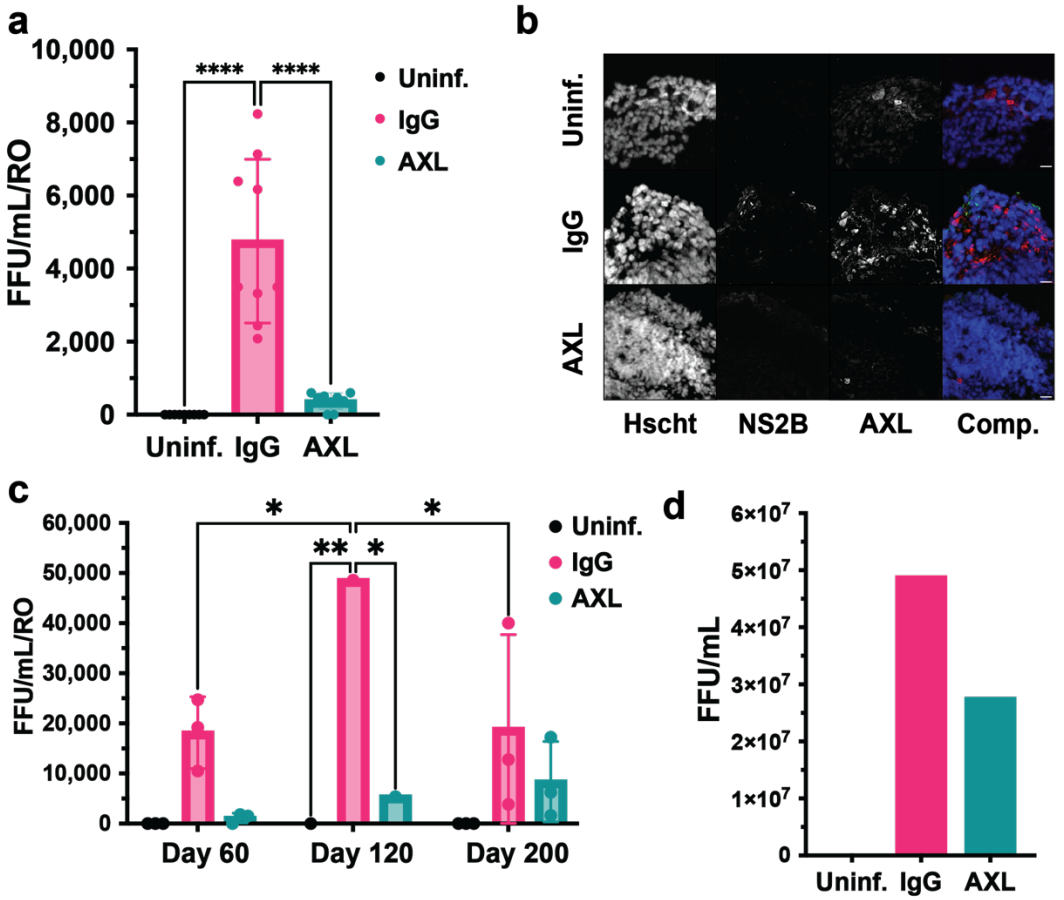


Figure 3. AXL is a Primary Receptor in Human Retinal Stem Cell Models. a. Analysis of ZIKV titer from the pooled supernatants of 3-4 uninfected, anti-IgG, or anti-AXL treated day 60 ROs at 30 hpi by focus forming assay. (n=9; **** indicates pValue <0.0001; 2way ANOVA). **b.** Immunohistochemistry for AXL and ZIKV NS2B in day 60 ROs at 30hpi. Nuclei staining with Hoechst 33258. 20μm scale bar. **c.** Analysis of ZIKV titer of uninfected, anti-IgG, or anti-AXL treated day 60 (n=3), 112 (n=1), and 200 (n=3) RO pooled supernatants at 48hpi by focus forming assay (p=0.0291 day 60 IgG vs day 120; p=0.0331 day 120 IgG vs day 200 IgG; p=0.0058 day 120 uninfected vs day 120 IgG; p=0.0124 day 120 IgG vs day 120 AXL; 2way ANOVA)**. d.** Analysis of ZIKV titer 48hpi uninfected, anti-IgG, or anti-AXL treated RPE supernatants by focus forming assay (n=1).

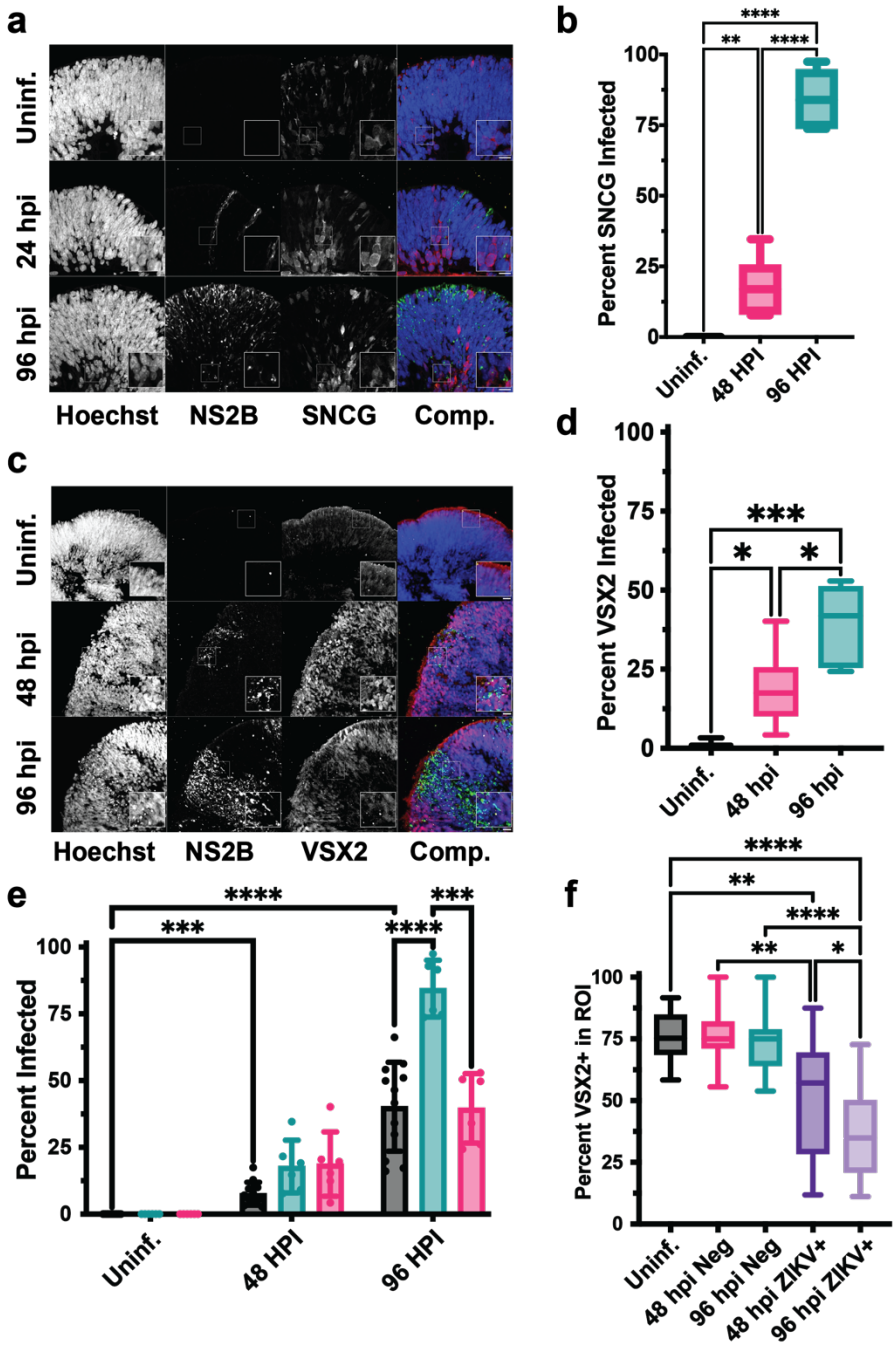


Figure 4. Zika Virus Infects Major Cell Types of Immature Retinal Organoids. **a,c.** Immunohistological staining for ZIKV NS2B and SNCG (a marker of RGCs) in uninfected and 24 or 96 hpi (**a**) or VSX2 (a marker of RPCs) in uninfected or 48 or 96 hpi (**c**) day 60 ROs. 20μm scale bars. **b.** Quantification of the percent of all

SNCG positive cells colocalized with NS2B staining at 48 and 96 hpi (n=3-4 RO; 2 regions per RO. p=0.0098 uninfected vs 48hpi; **** is pValue <0.0001; 2way ANOVA). **d.** Quantification of the percent of all VSX2 positive cells colocalized with NS2B staining at 48 and 96 hpi (n=3-4 RO; 2 regions per RO. p=0.0365 uninfected vs 48hpi; p=0.0136 48hpi vs 96hpi; p=0.0002 uninfected vs 96hpi). **e.** Quantification of NS2B costained for all nuclei compared to the percent of SNCG and VSX2 cells (n=3-4 RO; 2 regions per RO. p=0.0002 all uninfected vs all 48hpi; p=0.0002 all 48hpi vs all 96hpi; p=0.0002 VSX2 96hpi vs SNCG 96hpi; **** is pValue <0.0001; 2way ANOVA). **f.** Quantification of the percent of all nuclei VSX2+ from regions in or out of NS2B localization at 48 and 96 hpi (n=3-4 RO; 2 regions per RO. p=0.0002 all uninfected vs all 48hpi; p=0.0002 all 48hpi vs all 96hpi; p=0.0002 VSX2 96hpi vs SNCG 96hpi; **** is pValue <0.0001; 2way ANOVA). All ZIKV infections were at an MOI of 1. Nuclei staining for all IHC is with Hoechst 33258. Data in this figure are shown as the mean ± s.d.

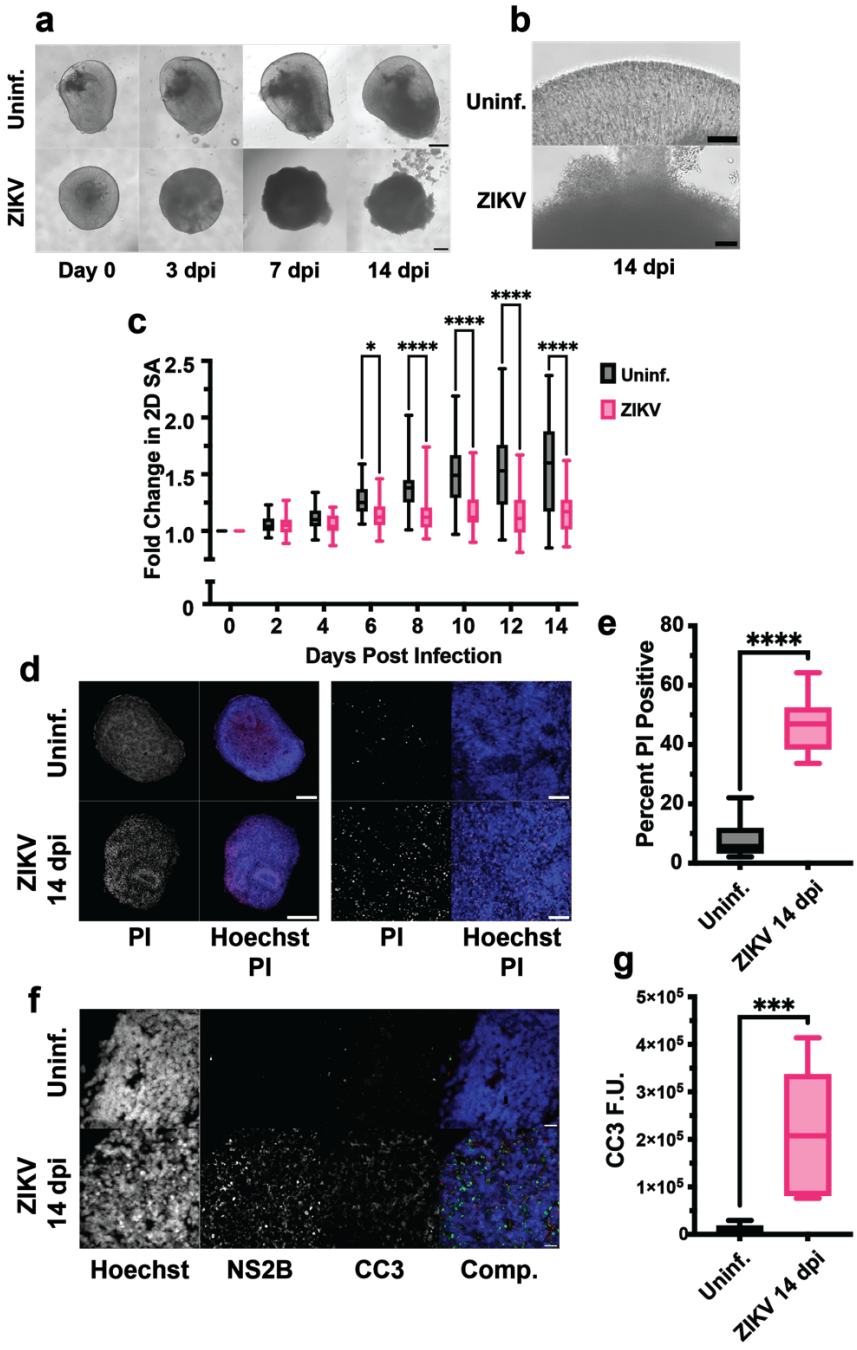


Figure 5. ZIKV Infection Impacts RO Growth and Viability. a,b. Brightfield imaging of day 60 ROs over 2 weeks of infection. Scale bars 100μm (**a**) or 50μm (**b**). **c.** RO size was quantified by the fold change in 2D surface area for individual organoids from time 0 (n=32. p=0.0139 Day 6; **** is pValue <0.0001; 2way ANOVA). **d.** Immunostaining of whole mounted 14dpi ROs stained with Hoechst and propidium iodide. Scale bars 200μm (left) or 50μm (right). **e.** Quantification of the percent of PI-positive cells of uninfected or ZIKV+ ROs at 14dpi (n=7 regions

from 3 RO; pValue **** <0.0001; unpaired t-test). **f.** Immunohistological staining for cleaved caspase 3 and ZIKV NS2B was performed on uninfected and 14dpi day 74 ROs (20μm scale bar). **g.** Quantification of cleaved caspase 3 fluorescence units in uninfected or 14dpi infected day 74 ROs (n=9 regions from 6 RO. p=0.0002; unpaired t-test). All ZIKV infections were at an MOI of 0.1. Nuclei staining for all IHC is with Hoechst 33258. Data in this figure are shown as the mean ± s.d.

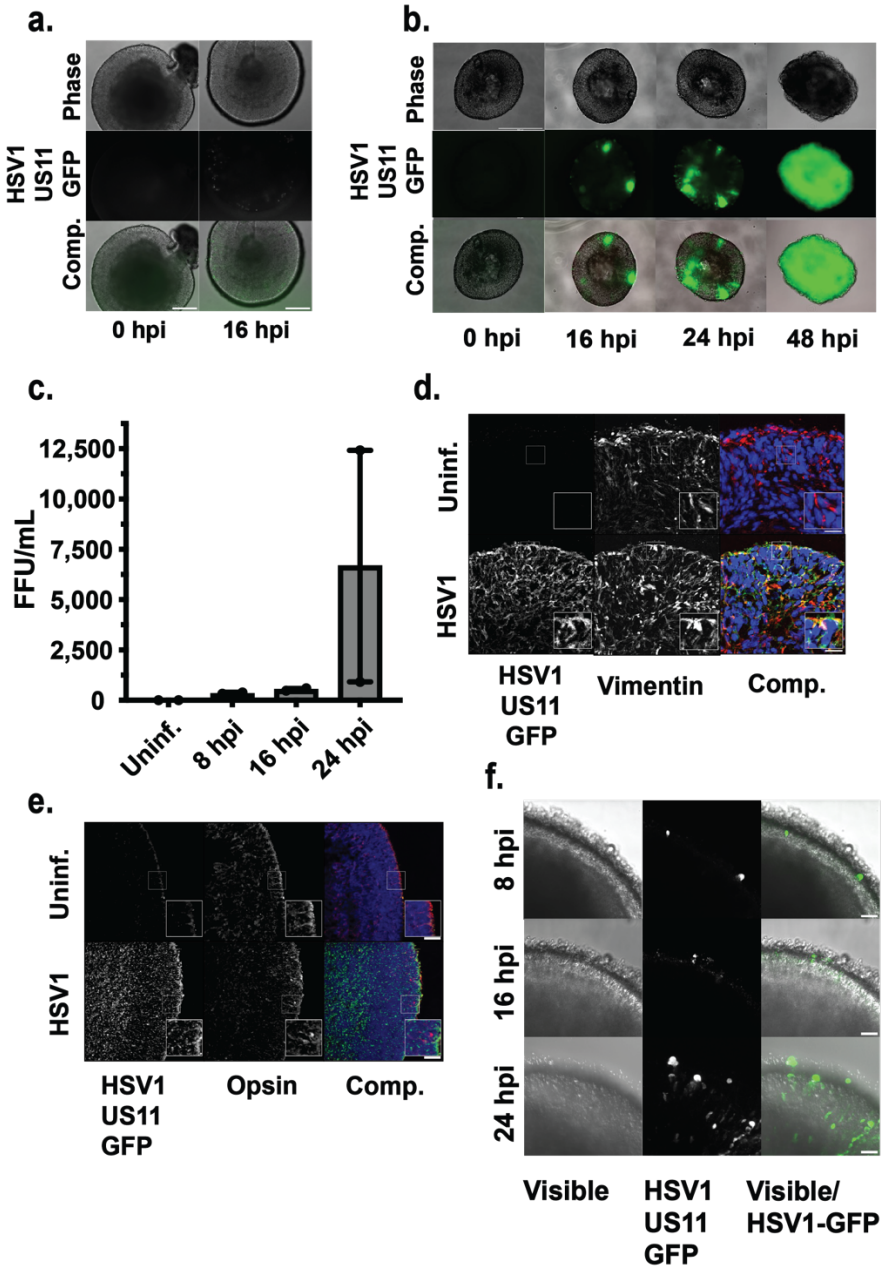
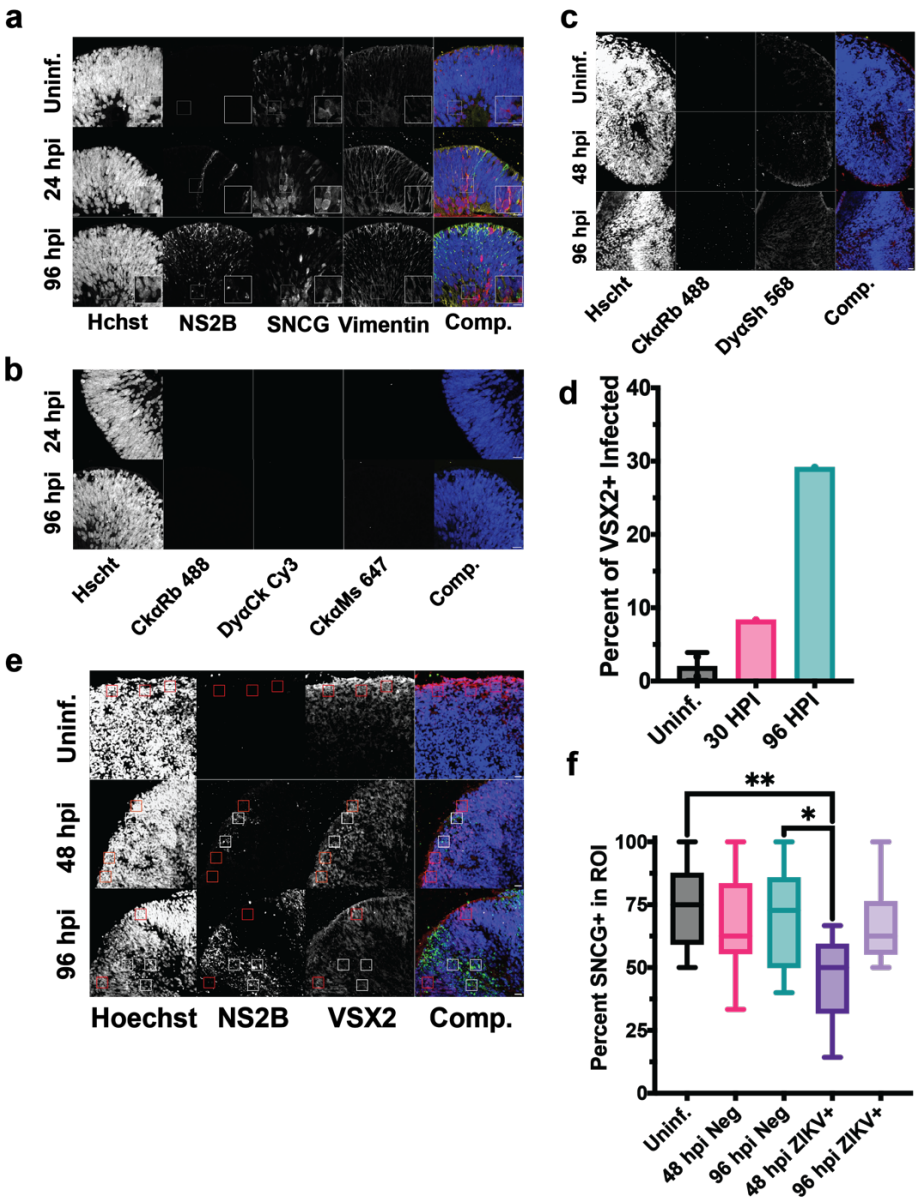
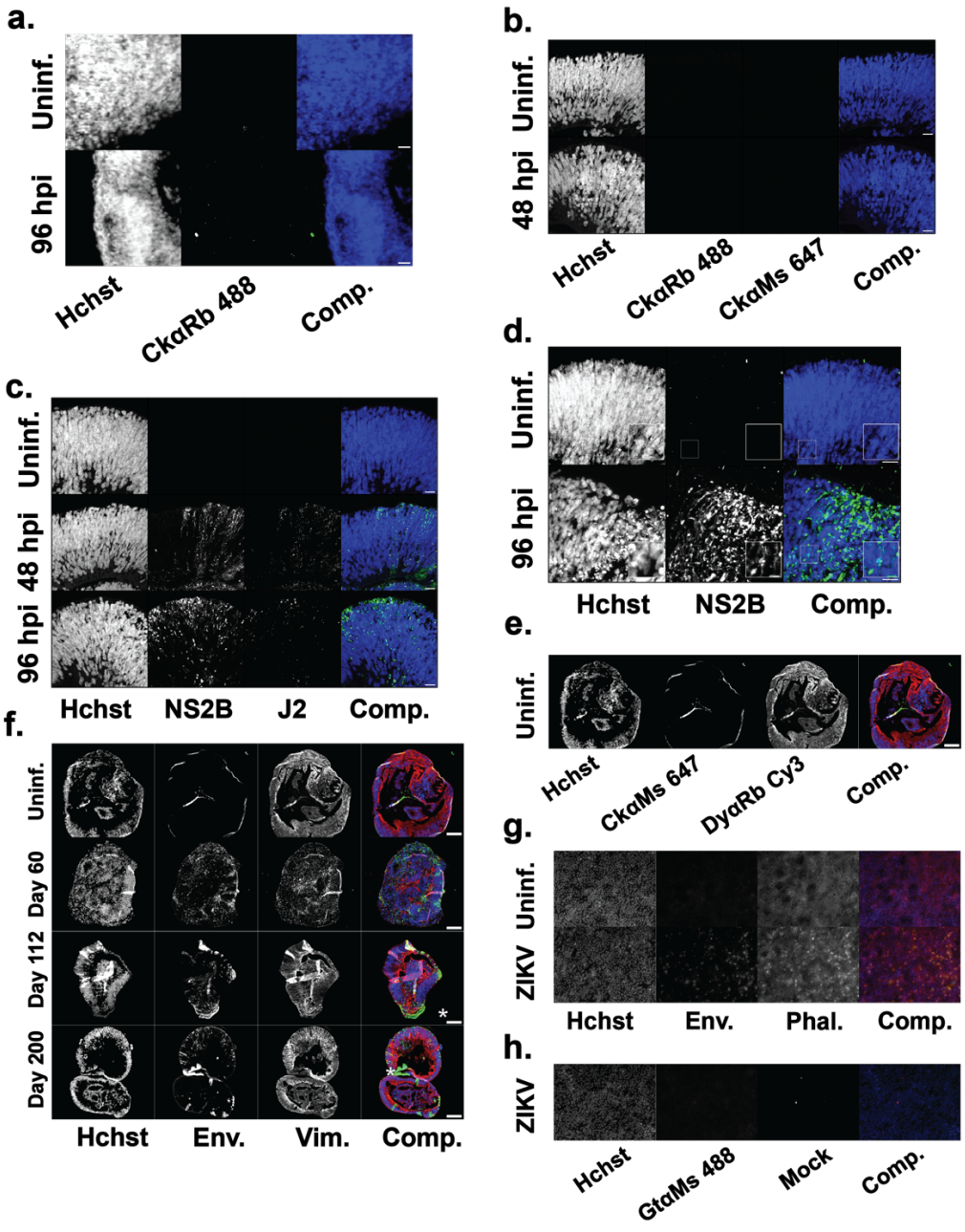


Figure 6. Mature ROs Effectively Model HSV1 Infection. a,b. Live imaging of phase contrast and HSV1-US11-GFP in uninfected and HSV1 infected day 113 ROs over 16 hpi (**a**) and day 180 ROs over 48 hpi (**b**) Both with a 200μm scale bar. **c.** Analysis of HSV1 titer from the pooled supernatants of 3-4 day 180 ROs over 24 hpi by focus forming assay (n=3). **d.** Immunohistological staining for vimentin (a marker of MGCs) against HSV1-US11-GFP in day 200 ROs at 24 hpi. 20μm scale bar. **e.** Immunohistological staining for opsin (a marker of PRs) against HSV1-US11-GFP in day 200 ROs at 24 hpi. 40μm scale bar. **f.** Live white light and HSV1-

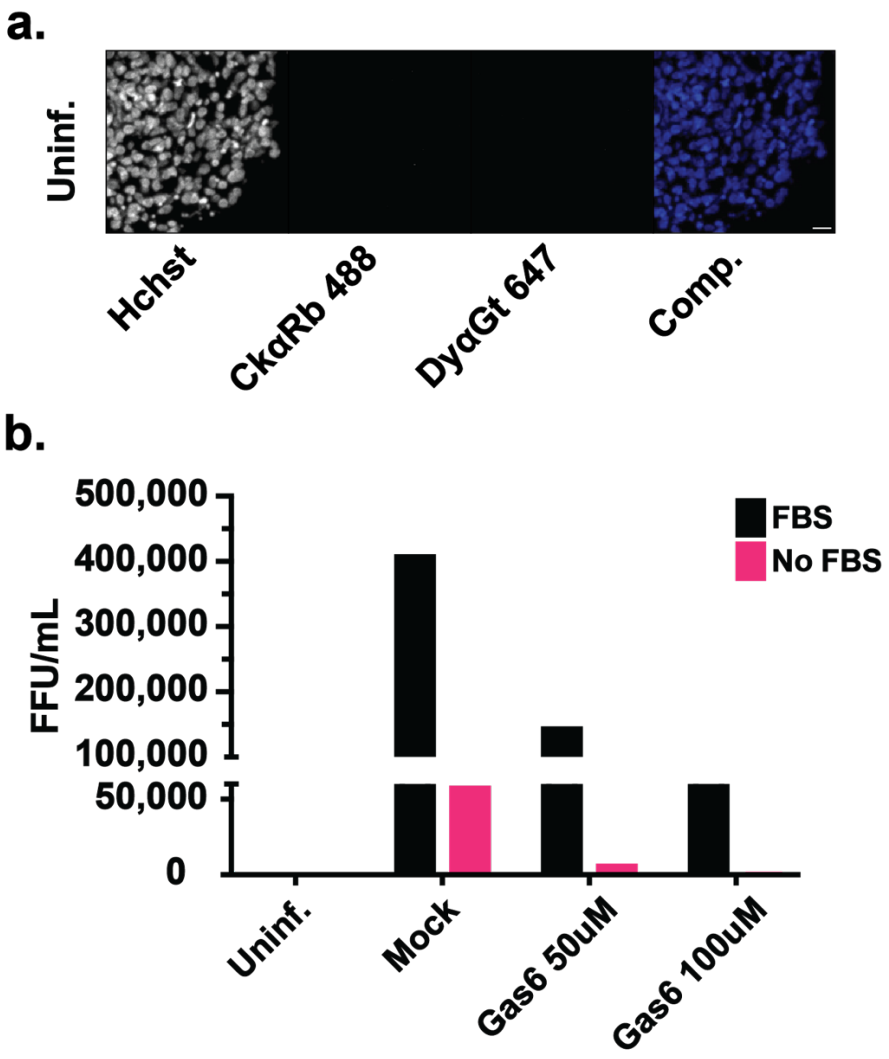
US11-GFP imaging in day 200 ROs at 8, 16, and 24 hpi. 40μm scale bar. All HSV1 infections were at 15,000 pfu/RO. Nuclei staining for all IHC is with Hoechst 33258.



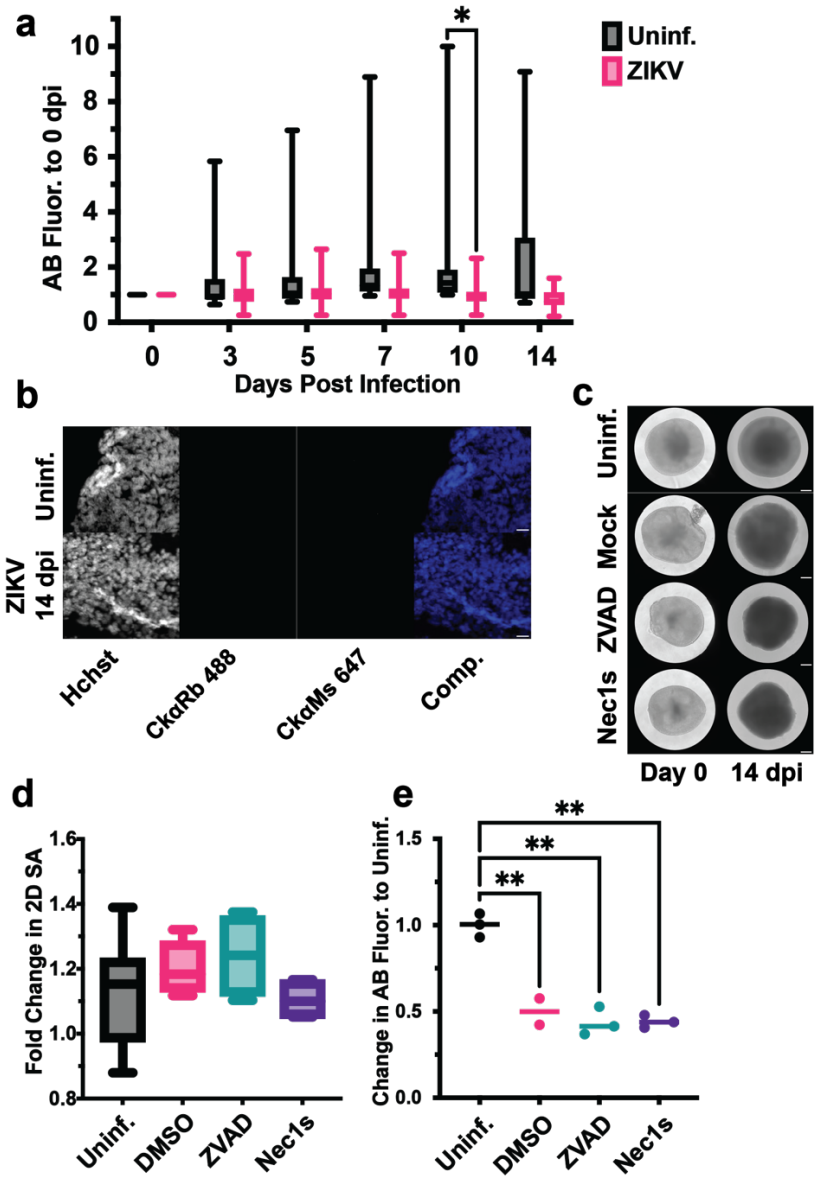
Suppl. Figure 1. a. Secondary control for chicken anti rabbit 488 (NS2B). **b.** Secondary control for chicken anti rabbit 488 (NS2B) and chicken anti mouse 647 (J2) (10um scale bar). **c.** Immunohistochemistry staining for NS2B and J2 dsRNA in uninfected, 48, and 96hpi in day 60 ROs (20μm scale bar). **d.** Histochemistry staining for NS2B (20μm scale bar). **e.** Secondary control for chicken anti mouse 647 (Env.) and donkey anti chicken 647 (vimentin) (400μm scale bar). **f.** Immunohistochemistry staining for NS2B and vimentin at 48hpi in day 60, 112, and 200 ROs (400μm scale bar). **g.** Immunofluorescence for ZIKV envelope and phalloidin. **h.** Secondary control for goat anti mouse 488.



Suppl. Figure 2. a. Secondary control for chicken anti rabbit 488 (NS2B) and donkey anti goat 647 (AXL) in anti-AXL treated day 60 RO at 30 hpi. **b.** Analysis of ZIKV titer in uninfected or anti-IgG, 50uM, or 100uM anti-GAS6 treated H4 cell supernatants at 48 hpi by focus forming assay (n=1). All ZIKV infections were at an MOI of 1.

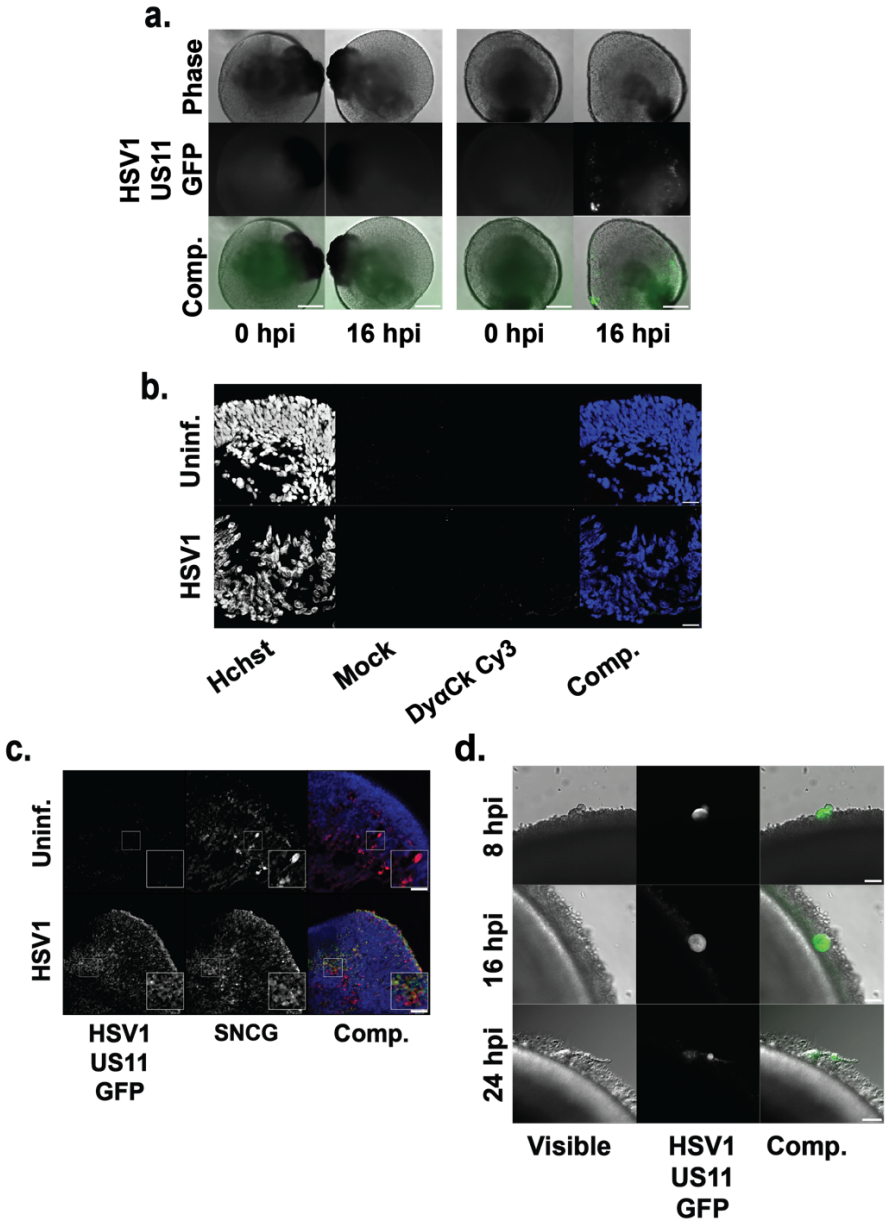


Suppl. Figure 3. a. Immunohistological staining for ZIKV NS2B, SNCG (a marker of RGCs), and vimentin in uninfected and 24 or 96 hpi 20μm scale bars. **b.** Secondary control for chicken anti-rabbit 488 (NS2B), chicken anti mouse 647 (SNCG), donkey anti Cy3 (Vim.). 20μm scale bars. **c.** Secondary control for chicken anti-rabbit 488 (NS2B) and donkey anti sheep 568. **d.** Quantifying the percent of VSX2+ stained cells that are NS2B+ from cytometry in dissociated uninfected and 30 or 96 hpi ZIKV-infected day 60 ROs (n=1). **e.** Representative 10% ROIs within NS2B-positive (white) or NS2B-negative (red) regions of VSX2 and NS2B stained day 60 ROs for Fig. 3f quantification. 20μm scale bars. **f.** Quantification of the percent of all nuclei SNCG+ from regions in or out of NS2B localization at 48 and 96 hpi (n=3-4 RO; 2 regions per RO. p=0.0054 uninfected vs 48hpi ZIKV+; p=0.0112 96hpi ZIKV neg vs 48 ZIKV+; 2way ANOVA). All ZIKV infections were at an MOI of 1. Nuclei staining for all IHC is with Hoechst 33258. Data in this figure are shown as the mean ± s.d.



Suppl. Figure 4. a. quantification of the fold change in alamarBlue fluorescence for individual ROs from day 0 to 14dpi (n=12 uninfected and 15 ZIKV. p=0.0297 Day 10; 2way ANOVA). **b.** secondary control for chicken anti rabbit (NS2B) and chicken anti mouse 647 (CC3) for cleaved caspase 3 imaging in Fig 4f. **c.** Brightfield imaging of day 60 ROs treated with ZVAD (50 uM) and Nec1s (50 uM) over 14dpi. 200μm scale bar. **d.** Quantification of the fold change in 2D surface area for individual ROs from day 0 to 14dpi in day 60 ROs treated with ZVAD or Nec1s. **e.** quantification of the fold change in alamarBlue fluorescence for individual ROs treated with ZVAD or Nec1s from time 0 to 14dpi (n=3 RO, n=2 DMSO. p=0.0035 uninfected vs DMSO; p=0.0011 uninfected vs ZVAD or Nec1s; 2way ANOVA). All

ZIKV infections were at an MOI of 0.1. Nuclei staining for all IHC is with Hoechst 33258. Data in this figure are shown as the mean ± s.d.



Suppl. Figure 5 Legend. a. Imaging of HSV1-US11-GFP in uninfected and HSV1 infected day 113 ROs over 16 hpi. Using phase contrast and immunofluoresence (200μm scale bar). **b.** Secondary control for donkey anti chicken Cy3 (Vim.). **c.** Immunohistological staining for SNCG (a marker of RGCs) against HSV1-US11-GFP in day 200 ROs at 24 hpi. 40μm scale bar. **d.** Live white light and HSV1-US11-

GFP imaging in day 200 ROs at 8, 16, and 24 hpi. 40μm scale bar. All HSV1 infections were at 15,000 pfu/RO. Nuclei staining for all IHC is with Hoechst 33258.

Chapter 3. 5’ and 3’ Single Cell RNA Sequencing Illuminates Differential Mechanisms Between Zika and HSV1 Infections

Summary

This study addresses the gap in understanding the role of distinct cellular populations in viral pathogenesis, a detail often missed in bulk assay analyses. Using single-cell RNA sequencing (scRNA-seq), we unveil the diverse mechanisms of Zika virus (ZIKV) and herpes simplex virus 1 (HSV1) pathogenesis within the varied cellular landscape of retinal organoids (RO). Our findings reveal the universal susceptibility of retinal cell types to ZIKV infection in ROs sampled at day 60. scRNA-seq further allows us to pinpoint specific genes highly differentially expressed in response to infection, notably those involved in cellular stress responses and interferon alpha and beta signaling pathways. In contrast, HSV1 infection leads to a reduction in intracellular transcript diversity, culminating in the formation of a distinct HSV1-specific cell cluster. These insights underscore the utility of scRNA-seq in detecting unique and virus-specific pathogenic pathways within individual cells, offering a more nuanced understanding of viral effects in retinal organoids.

Introduction

To comprehensively understand ZIKV infection and disease, we sought to probe global expression changes between cellular populations in retinal organoids (ROs). As described in Chapter 1, single-cell RNA sequencing is a powerful method to achieve this, but it has to be carefully adapted to studying viruses such as ZIKA.

The original methods for scRNA-Seq were 3’ and were based on polyadenylation for transcript capture. Unfortunately, as Flaviviruses are single-stranded, positive-sense viruses lacking a 3’ poly(A) tail, original methods could not capture flaviviral transcripts, so they could only be measured indirectly through changes in host responses. Subsequent studies applying scRNA-sequencing for immune profiling led to developing 5’ based methods like Single Cell Immune Profiling Assay at 10Xgenomics. Although initially for immune profiling, this and similar methods can be adapted for studying Flaviviral infections through modifications like spiking in flaviviral-specific capture primers into the RT step as suggested by 10Xgenomics and has been implemented for DENV and ZIKV by Zanini et al., *eLife* 2018 [141, 165]. This methodology has successfully analyzed DENV infection of memory and naïve B cells and PBMC monocyte cells [166, 167]. scRNA-Seq has further been applied to investigate ZIKV in multiple contexts. As mentioned, Nowakowski et al., *Cell Stem Cell* 2016 identified candidate target cellular populations in primary human neural retinas like retinal progenitor cells [94]. It has been further applied to study ZIKV in brain organoids by Ocwieja et al., *PEDS* 2021, and in comparison to HSV1 by Krenn et al., *Cell Stem Cell* 2021 [104, 106]. Validation for modeling ocular ZIKV infections in retinal organoids (ROs) was demonstrated by Contreras et al., 2023. [insert citation] However, only bulk sequencing was applied to infected hiPSC-derived retinal stem cells and fetal RPE (fRPE) with deep-sequencing just for fRPE [129]. Here, we provide the foundation for utilizing scRNA-Seq to assess ZIKV and HSV1 infections in ROs at stages with more clinically relevant cell types. For ZIKV, we applied 5’ single-cell RNA sequencing following the 10XGenomics

protocol while spiking in a ZIKV-specific primer into the master mix for viral transcript capture (**Materials and Methods**) [165].

Our work with single-cell RNA sequencing would not have been possible without Dr. Zachary Aralis. He is responsible for the entirety of the single-cell RNA sequencing, both at the bench and computationally, for all of the scRNA-seq figures in this dissertation.

Results

5' scRNA-Seq Reveals Stress and Immune Dysregulation in ZIKV Infected ROs

scRNA-Seq has provided the ability to examine how differences between individual cells and populations behave, bringing a high order of power to complete experiments such as within cell complexity of organoids or variability in viral infection. We applied scRNA-sequencing to dissociated day 60, ZIKV-infected ROs at 24, 48, and 96hpi at an MOI of 1 to investigate the impact of ZIKV on individual RO cells (**Fig 1a**). As ZIKV is not polyadenylated, 5' scRNA-Seq was utilized to identify ZIKV-transcripts by spiking ZIKV-specific primers into the reagent mix (**Suppl. Fig 1a**). For a successful run, active infections were confirmed with tittering (**Suppl. Fig 1b**), the number of input cells was determined by TrypanBlue (**Suppl. Fig 1c**), and the final post-processing number of cells used in the analysis was pooled between replicates (**Suppl. Fig 1d**). scRNA-seq identified all expected cell clusters, with a strong association of representative cell type genes in the clusters

(**Fig 1b, Suppl. Fig 1e**). As a global overview of infection by cell types, the Log_2FC expression level of ZIKV transcripts on the same UMAP cluster analysis demonstrates that all types are permissive (**Fig 1c**). Across all cell types, the percentage of infected cells increases stepwise over 96hpi (**Fig 1d**). The clusters were split by cell type to determine the individual contributions. When pooled across time points, the proportion of cell types infected is relatively consistent. However, compared to other classes, the PRs have decreased infection levels, and ISGs are dominated by ZIKV-positive cells (**Fig 1e**). At a granular level, the infection profiles between cell types are variable, suggesting underlying differences (**Suppl. Fig 1f**). The starkest difference is for the ISG cluster generated in response to ZIKV over time, both globally and in terms of the percent of all infected after 24 hpi (**Suppl. Fig 1g***). To match IHC data from Chapter 2 Fig 3e, although the percent infected is lower than IHC, the proportion of cell types infected is consistent (**Suppl. Fig 1h**).

To better understand the impact of ZIKV infection on ROs, the differentially expressed genes (DEGs) between ZIKV+ cells from 48-and-96hpi compared to uninfected mock samples were portrayed in a volcano plot with the most significantly dysregulated DEGs over $-Log_{10}pValue$ of 100 and Log_2FC less that -1 for downregulated and over +1 for upregulated genes (**Fig 1f**). Lastly, to identify globally dysregulated networks, pathway enrichment analysis was applied to the significant DEGs identifying Cellular Stress Responses, IFN Alpha and Beta Signaling, mRNA Processing, amino acid metabolism, and cellular stress responses (**Fig 1g**) [168]. 5’ scRNA- sequencing can identify ZIKV infection within cell type-

specific clusters of day 60 ROs while highlighting specific DEGs within broader transcriptional network dysregulation.

3’ scRNA-Seq Highlights the Decay of Cellular Identity from HSV1 Infection in Mature ROs

In addition to 5’ single-cell RNA sequencing, conventional 3’ scRNA-seq single-cell RNA sequencing has been applied to study polyadenylated viral infections and organoids. Similar to ZIKV, we applied 3’ scRNA-Seq for mature ROs infected with 15,000 pfu/RO. Infected ROs at 0, 8, 16, 20, and 24 hpi were dissociated and processed through the scRNA-Seq pipeline (**Fig 2a**) with the total number of input cells by replicate (**Suppl. Fig 2a**). UMAPs clustering of pooled timepoints demonstrates expected cell type clusters for the retina in mature ROs, including PR, Cone PR, MGC, HC, AC, BC, RGC, and RPCs, in addition to an HSV1-specific cluster for cells whose transcripts are dominated with HSV1 transcripts (**Fig 2b**). Representative genes for each cluster are expressed in a dot plot (**Suppl. Fig 2b**). When HSV1 transcript expression is expressed on the same UMAP, there is a limited infection in all cell types with an expressing shoulder of the MGC cluster. In contrast, the infected cells and the heaviest infected regions are dominated by the HSV1 cluster (**Fig 2c**). HSV1-positive cells were denoted by > 0.1 Log2FC in at least 2 of the immediate early genes (US1, RS1, RL2, UL54) to determine the percent of cells infected by timepoint. When quantified by time point, there is minimal infection at 8hpi, slightly more plateauing at around 10% from 16-to-20 hpi, and spiking to about 70% at 24hpi (**Fig 2d**). During HSV1 infection,

replication encodes a virion host shutoff (VHS)-RNase involved with host evasion by widespread host and viral RNA degradation [169]. The diversity of transcript populations was analyzed to determine if VHS contributes to the loss of identity. The density of the unique molecular identifiers of transcripts is severely reduced in the HSV1-positive population compared to the HSV1-negative, supporting identity loss during infection (**Fig 2e**). HSV1 genome replication involves the highly ordered cascade from latency through lytic reactivation [170]. To interrogate the timing of HSV1 replication, the clustering of HSV1 transcripts alone is based on the percentage of all transcripts that are HSV1 (**Fig 2f**). The HSV1 cluster was then expressed through pseudotime based on the temporal expression of the HSV1 genome. The percent of HSV1 expression matches the pseudotime analysis where there is increased temporal HSV1 expression over time (**Fig 2g**). The timing of reactivation and replication from representative genes is expressed in a dot plot with high expression peeking through time (**Suppl. Fig 2c**). In sum, 3' scRNA-Seq can be faithfully applied to mature ROs to detect HSV1 transcripts and replication through time and all expected cell type clusters while determining viral-host shutoff from infection.

Discussion

We have applied scRNA-Seq to study ZIKV and HSV1 in ROs for the first time for either. scRNA-Seq is crucial for clarifying the infection profiles of ZIKV and HSV1 infections at a granular level within the complexity of RO cellular populations. In this chapter, we demonstrated the power of scRNA-Seq for understanding ZIKV and HSV1 infections in distinct ages of retinal organoids while identifying unique

infection mechanisms. (1) We confirmed the efficacy of scRNA-Seq in identifying all expected cellular identities by RO age and ZIKV and HSV1 expression levels from primer spiking. (2) Unique viral expression profiles through time in ROs with stepwise increases for ZIKV as opposed to a dramatic late time point increase for HSV1, indicative of lytic replication. (3) Differentially expressed genes by ZIKV infection status involve cellular stress and type I immune signaling. (4) Stress responses were upregulated in ZIKV-positive cells, whereas the opposite is true for bystander immune signaling. (5) A loss in cell identity from HSV1 infection from viral-host-shutoff (VHS) not seen for ZIKV.

First, we identified all expected cell types in immature ROs and ZIKV transcripts with a high sensitivity. scRNA-Seq identified similar patterns of ZIKV production following a stepwise increase in ZIKV transcripts proportional to titers in Chapter 2 (and the titers for the ROs used in sequencing experiments). Within day 60 ROs, the susceptibility of all cell types to ZIKV was identified by scRNA-seq with ZIKV transcript expression in clusters of RPCs, RGCs, HC/AC/BP, MGCs, and PRs. Unlike the rest, PRs have less than half the number of infected cells as the other clusters. Of note, from the few down-regulated genes, the largest was for recoverin, a photoreceptor marker suggesting impaired photoreceptor differentiation. Unlike photoreceptors, there is the generation of an ISG cluster, seen by UMAPs (denoted by *) or by the percent of each cell type infected by time point. It appears to be reduced at 96hpi based on umaps, suggesting the resolution of infection, altered fate, or cell death. In addition to comparing scRNA-seq ZIKV levels to IHC, the relative percent of SNCG+, VSX2+, and all cell populations infected from scRNA-

seq was comparable to IHC quantification in Chapter 2, although at a lower level overall. ZIKV infection highlighted a set of differentially expressed genes (DEG) based on infection status at a granular level enriched for cellular stress and immune responses, some of which are conserved across other modeling.

Unlike the easily distinguishable levels of ZIKV infection in our clusters, that was not the case for HSV1. HSV1-mediated loss of cellular identity is likely the combination of VHS degrading host transcripts and HSV1 replication dominating the proportion of sampled transcripts, as seen with neuroepithelial identity impairment in HSV1-infected brain organoids [104]. In this thesis, we aimed to model acquired adult HSV1 infections, but in addition to ARN, acquired adult infections can be transmitted *in utero* or newborns and cause ocular lesions and other fetal malformations [171]. As we modeled congenital Zika syndrome in immature ROs, the difference in responses between viruses and RO age responses could be directly compared from ZIKV infection in day 200 and HSV1 infection in day 60 ROs. ZIKV infection between day 60 and 200 ROs would clarify the conservation of responses or the nuanced mechanism underlying early or late trimester infections, especially with MGCs and PRs. As with ZIKV, it would be interesting to see if the individual comparisons between ROs for HSV1 are conserved by age (like VHS and no immune or stress responses) or if independent mechanisms are in place.

The most accurate modeling for HSV1-related ARN is with fully functional viral particles. Active VHS severely limits the identity of cell types infected and any potential host responses to HSV1 at an RNA level. VHS would likely cause a loss in cell identity and responses, so future experiments with a VHS-deficient form of

HSV1 would help identify bystander or host responses from infected cells [172]. These experiments would solidify the foundation for modeling ocular targeting viruses in ROs and allow more direct comparisons to the specific responses to HSV1 and ZIKV in brain organoid modeling [104]. Although there is limited published literature, scRNA-seq can bridge organoid modeling to clinical pathologies in primary or patient-derived cell systems [96]. The efficacy of RO infections compared to those of the human retina remains unknown. If primary retinas can be obtained from HSV1 and ZIKV-infected patients or from healthy donors that are separately infected after dissection, it will be crucial for in-depth comparisons of how well ROs are for modeling primary, clinically relevant viral diseases.

Although ZIKV-specific responses were clear by infection status, future experiments to increase sample size would allow interrogation into cluster-to-cluster response variation to fully harness the heterogeneous nature of ROs. The most robust data would be produced by increasing the number of organoids and independent differentiations to average out any cell type-sampling bias. Further power would be achieved from more cells sequenced and deeper sequencing depth. A higher level of infection would help solidify the critical bystander and ZIKV-stimulated genes by increasing the proportion of cells infected while generating more robust responses. The increase in data points in each category will help clarify the specific nuances in responses over time and, more importantly, allow visualization of the difference in cell type-specific susceptibility, bystander stimulation, and responses to infection.

Lastly, even though scRNA-seq has excellent power for addressing the cellular heterogeneity of organoids, the spatial resolution is lost during dissociation, ignoring the role of 3D structure and infection proximity on cellular responses. Our data suggests that we can indirectly see infection differences in cell types based on proximity to virus access by the percent of cell types infected at 24hpi matching proper cell type niches within the organoid. The RPCs expected to localize to the outside of the RO have the most significant proportion infected, MGC and recoverin positive PR precursors spread through the organoid with an intermediate infection level, and internal RGC, HC, and ACs with minimal infection [137]. IHC in Chapter 1 supports the delay in infection by spatial differences in differential infection profiles where SNCG+ ROIs have decreased expression at 48hpi that recovers to uninfected expression levels by 96hpi when viral penetrance reaches internal RGC regions. As we likely see differences in infection profiles based on localization, combining an increased sample size and spatial sequencing would allow a multidimensional analysis of infection responses between cell types or over differentiation time.

Recently, techniques like Light-Seq and Nanostring GeoMx Digital Profiling have been developed using light-directed spatial profiling that combines antibody staining for regions of interest with UV-cleavable in situ RNA probes. RNA probes can be collected from individually segmented areas with light while leaving samples intact for subsequent processing at a comparable resolution to field standards like RNAseq [173, 174]. From antibody staining, these techniques would identify responses inside plaques that expand outwards radially as would occur with

bystander stimulation as seen with spatial resolution of host inflammatory responses in postmortem COVID-19-infected lung tissue [175]. In ROs, we can parallel the marker staining from Chapter 1 to understand the change in transcriptional profile by cell type. Even though the IHC in Chapter 1 demonstrated decreased loss of VSX2+ at infection sites, what those cells become is unknown.

Similarly to the bystander effect, spatial sequencing could help understand that using antibodies against VSX2 and NS2B to select representative regions and the transcriptomic transitions in changing progenitor populations could be investigated. As the ISG cluster generates in scRNA-seq, there appears to be a decrease in the RGC cluster by 96 hpi, not reflected at the protein level by IHC, further emphasizing the power from the intersection between these techniques. Again, these could be paralleled for data obtained from other proposed VHS-deficient HSV1 future experiments.

In-depth commentary on the scRNA-seq data is presented in the thesis of Dr. Zachary Aralis [159].

Figures

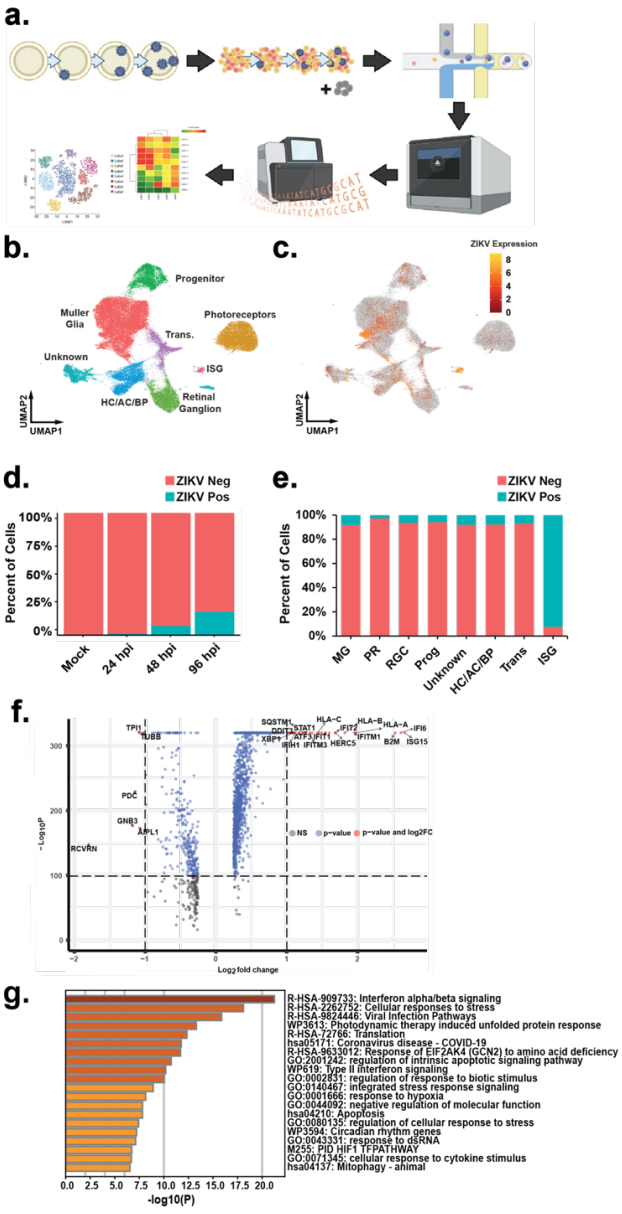


Figure 1. 5' scRNA-Seq Identified ZIKV Infection in RO Specific Clustering. a. Experimental workflow diagram for scRNA sequencing (scRNA-Seq) of ZIKV infection at an MOI of 1 over 96 hpi in day 60 ROs (created in BioRender). **b.** Global display of clustered scRNA-seq data represented as a UMAP. **c.** ZIKV transcript expression represented in UMAP clustering. Each cell's infection status designated by >0.1 Log_2FC ZIKV expression; expression level increases from red to yellow. **d,e.** The percent of ZIKV-positive cells identified of all cells at each infection

timepoint (**d**) or cumulatively by cell type (**e**). **f.** Volcano plot analysis of ZIKV-positive cells at 48 and 96 hpi to mock samples. Genes above a $Log_{10}P$ value 100 in blue and a Log_2FC $-1 > X > 1$ in red. **g.** Pathway enrichment analysis for the significant DEGs between 48 and 96 hpi ZIKV positive cells to mock (generated in Metascape [168]).

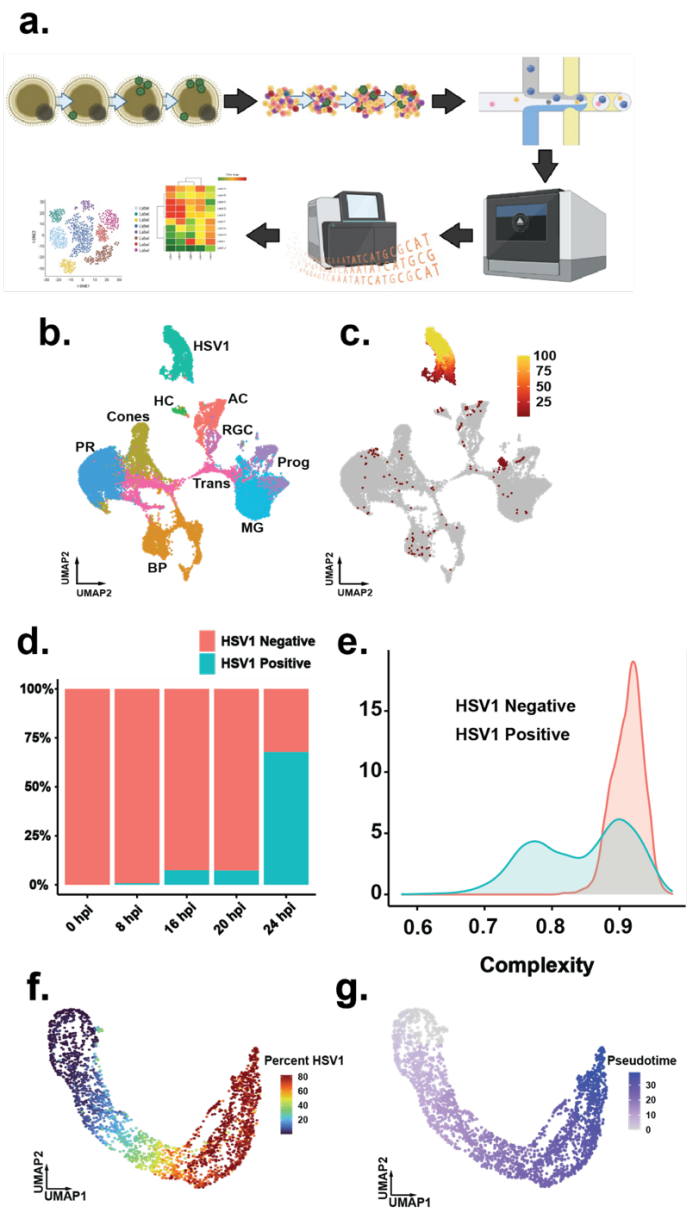


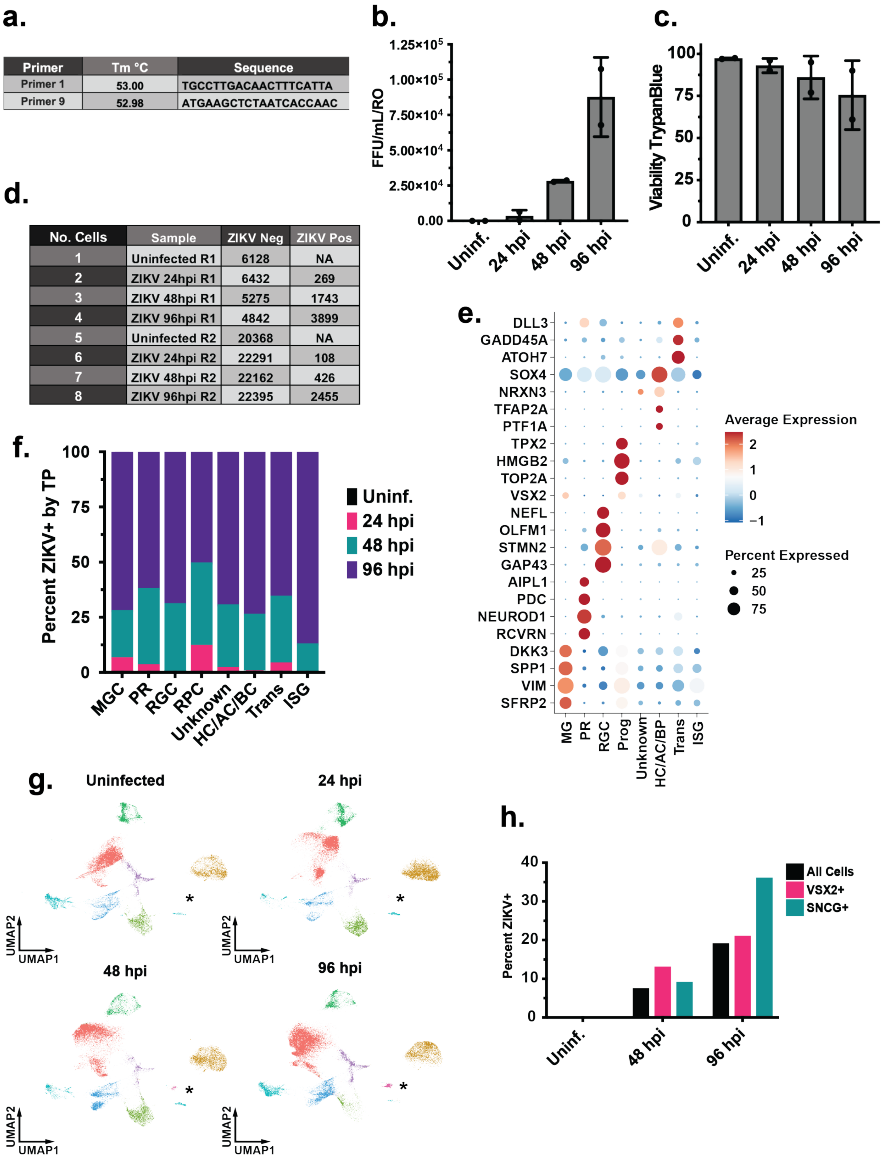
Figure 2. 3' scRNA-Seq of HSV1 highlights identity loss from infection in mature ROs. a. Experimental workflow diagram for scRNA sequencing of HSV1 infected day 180 with 15,000pfu/RO over 24hpi (created in BioRender). **b.** Global display of clustered scRNA-seq data represented as a UMAP. **c.** HSV1 transcript expression represented in UMAP clustering. Expression level increases from red to yellow. **d.** The percent of HSV1 positive cells identified of all cells at each infection time point. **e.** Density plots for the complexity of transcripts by infection status. **f,g.** Clustering of HSV1 positive reveals cellular trajectories based on HSV1 transcript level (**f**) and pseudotime (**g**).

a.

Primer	Tm °C	Sequence
Primer 1	53.00	TGCCTTGACAACTTTCATTA
Primer 9	52.98	ATGAAGCTCTAATCACCAAC

d.

No. Cells	Sample	ZIKV Neg	ZIKV Pos
1	Uninfected R1	6128	NA
2	ZIKV 24hpi R1	6432	269
3	ZIKV 48hpi R1	5275	1743
4	ZIKV 96hpi R1	4842	3899
5	Uninfected R2	20368	NA
6	ZIKV 24hpi R2	22291	108
7	ZIKV 48hpi R2	22162	426
8	ZIKV 96hpi R2	22395	2455

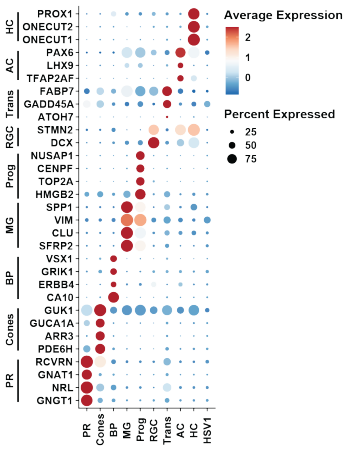


Suppl. Figure 1. a. Spike in primer sequences. **b,c.** Analysis of ZIKV titer by focus forming assay (**b**) and dissociated RO viability with Trypan Blue (**c**) for scRNA-seq input uninfected, 24, 48, and 96 hpi samples (n=2). **c.** Individual contributions to global UMAPs by time point. **d.** Number of input samples by sample and replicate (n=2). **e.** Dot plot analysis for representative genes utilized for cell type clustering. **f.** The percent of infected cells by cluster across time. **g.** UMAPs for the representation of clusters by time point. **h.** The percent of all cells, SNCG+, or VSX2+ cells that are ZIKV positive over 96 hpi from scRNA-Seq.

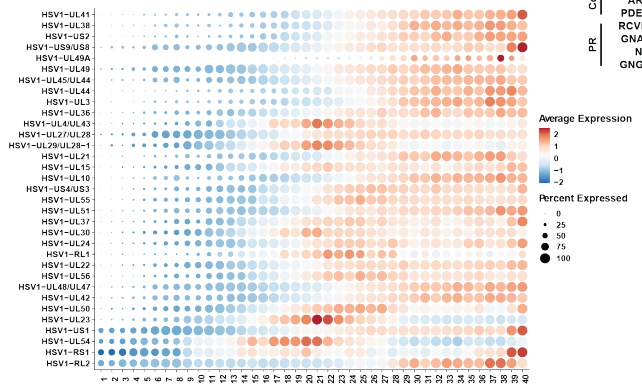
a.

No. Cells	Sample	HSV1 Neg	HSV1 Pos
1	Uninfected R1	6128	NA
2	ZIKV 24hpi R1	6432	269
3	ZIKV 48hpi R1	5275	1743
4	ZIKV 96hpi R1	4842	3899
5	Uninfected R2	20368	NA
6	ZIKV 24hpi R2	22291	108
7	ZIKV 48hpi R2	22162	426
8	ZIKV 96hpi R2	22395	2455

b.



c.



Suppl. Figure 2 Legend. a. Number of input samples by sample and replicate. **b.** Dot plot analysis for representative genes utilized for cell type clustering. **c.** Dot plot analysis for HSV1 genes organized by expression timing.

Chapter 4. Modulation of Stress Response Networks Undermines Zika Replication and Infections in Retinal Stem Cell Modeling

Summary

The role of cellular stress responses in Zika virus (ZIKV) infection of the retina remains unexplored despite its significant influence on ZIKV pathogenesis in the brain and its link to microcephaly. Utilizing single-cell RNA sequencing (scRNA-seq) on retinal organoids (RO), this chapter delineates the modulation of unfolded protein responses (UPR) in cells positive for ZIKV. Our investigation reveals that targeting the UPR components—IRE1, ATF6, and BIP—through pharmacological inhibition markedly reduces ZIKV replication. Furthermore, we identify ATF6 and PKR inhibition as critical for enhancing the viability of RO cells during infection. Notably, during prolonged infections, the inhibition of PERK is shown to restore RO metabolism, suggesting differential roles of UPR pathways in acute versus chronic retinal ZIKV infections. These findings provide a comparative view of UPR activity's impact on ZIKV infections, highlighting distinct retinal responses compared to other tissues and underscoring the potential for targeted therapeutic interventions.

Introduction

ZIKV uses cellular resources and structures to replicate and infect further cells (discussed in **Chapter 1. III**). In doing so, ZIKV must compete with and subvert host cell stress networks to replicate effectively, like by forming ZIKV replication hubs in the endoplasmic reticulon (ER) [54]. The ER is the largest organelle in a cell and is responsible for approximately one-third of the synthesis of the proteome,

including a great majority of the proteins secreted and displayed on the plasma membrane [176]. The ER and autophagic networks are critical for maintaining retinal homeostasis and supporting neuronal health for proper phototransduction in the retina. Photoreceptors are under constant insult from light exposure and, to combat that, have a daily turnover of their outer segments requiring constant proteasomal support [177]. The retina's high metabolic cost and sensitivity make it exceedingly susceptible to insult from viral infection.

ER morphology is complex and has specialized environments with rough sheets and smooth tubules, allowing the ability to perform a wide range of functions. The nuclear envelope is contiguous with the ER and is responsible for the passive or active transport with the nucleus by creating a barrier between inner and outer nuclear lipid bilayer membranes. Those are connected to the peripheral ER, comprised of rough sheets of membranes saturated with ribosomes, intricately folded to create the cisternae where most membrane-bound proteins are synthesized, folded, modified, and then secreted. The tubular network of the ER is highly dynamic in response to different cellular processes, an attribute that can be harnessed as an advantage for viral replication as with ZIKV, as discussed in Chapter 1 [63, 178].

Refer to Ropidi et al. *J Biomed Sci* 2020 for an extensive review of ZIKV and modulation of the ER [63].

Zika Virus Modulation of ER Biosynthetic Capacity

ER Function and the Unfolded Protein Response (UPR)

Proper ER health is crucial for cellular function maintained through strict quality control paired with effective countermeasures against proteomic stress. The unfolded protein response (UPR) is a conserved cellular stress response activated by the accumulation of unfolded or misfolded proteins in the ER lumen, known as ER stress. The UPR is governed by three transmembrane sensors, IRE1, PERK, and ATF6, which act in concert to trigger transcriptional networks, leading to reduced protein load and increased folding capacity of the ER to accommodate and relieve ER stress. If successful, the cell will adapt and survive, but if the initial insult is too great or ER stress is not resolved, the balance of this transcriptional network will shift to cell death pathways to preserve the organism's health (**Figure 1**) [179, 180].

ATF6 is a type II ER transmembrane protein that, upon ER stress, leads to an ATF6-to-Golgi translocation before the release of the ATF6 N-terminal (ATF6n) cytoplasmic domain. ATF6n is a bZIP transcription factor that translocates to the nucleus to upregulate UPR target genes, including XBP1. IRE1 is a single-pass transmembrane protein that, when activated, leads to alternative splicing of XBP1 mRNA (XBP1s), acting as a transcription factor driving genes involved with ER homeostasis. Concurrently, IRE1 relieves protein input by limiting input with regulated IRE1-dependent decay (RIDD). The third, PERK, phosphorylates the alpha subunit of eukaryotic translation initiation factor eIF2 (eIF2a) in the cap-

dependent translation complex. eIF2a-phosphorylation leads to global translational arrest in an attempt to alleviate the translation burden of the ER. eIF2a-phosphorylation also leads to selective translation of an upstream ORF in the mRNA of transcription factor ATF4, which activates pro-apoptotic CHOP through upregulations in ATF4 and XBP1 [179].

In addition to being a member of the UPR, PERK is also a member of the broader integrated stress response (ISR), a dynamic response network responsible for throttling the biosynthetic capacity of the cell through a diversity of stressors. The mammalian ISR is composed of four stress kinases: PERK, protein kinase RNA-activated (PKR; double-stranded RNA detection), GCN2 (uncharged tRNA detection), heme-regulated inhibitor (HRI; heme deficiency detection, redox imbalance, and as a mitochondrial stress relay). When under stress, the interplay of these pathways converges on kinase phosphorylation of the eIF2a and a global translational halt against further insult. In concert, there is the selective synthesis of specific proteins to alleviate stress, ultimately to cell survival and adaptation, or others for initiating cell death if the insult is too great or remains unresolved [181].

There has been significant interest in studying the UPR and ISR in the context of viral infections, particularly flaviviruses. Due to its highly regulatory role, BIP is a frequent target for flaviviruses for ER modulation [63, 182]. Although not conserved, in most cases, ZIKV infection causes a blunted BIP response [183, 184]. Currently, the modulation of BIP during ZIKV infection and its role in replication in eye modeling is unknown.

In mammals, tissue and organ development require extensive cellular proliferation. Proliferation is integral in brain development for new neuron synthesis and proper cortical expansion before pruning of excess neuralization through apoptosis. The UPR is a fundamental mechanism for triggering the temporal regulation between direct and indirect neurogenesis and as an effector for downstream neuronal programmed cell death (**Chapter 1, Figure 4**).

Human Embryonic Brains

The differences in UPR activity between fetal and adult brains are a crucial indicator of the role of the UPR in early neurogenesis. Embryonic brains have higher expression of ATF6 and ER chaperones (including calreticulin, GRP78, and GRP94). More directly, in the early stages of development, there is high ATF4 that gradually decreases through development, supporting ATF4 as a critical factor in the transition to indirect neurogenesis [97]. The underpinning of the UPR in fetal neurogenesis is imperative for how its dysregulation from ZIKV infection induces microcephaly. In human fetal embryonic cortices, ZIKV infection causes upregulation of PERK and IRE1 downstream effectors (~22 GW) [76]. Other ZIKV-infected cortices have shown upregulations to ATF4, CHOP, PDI, and MX1 (21-23 GW) [185]. In infected cortices, prolonged ER stress (including Calreticulin and Calnexin) restricts hNPCs to direct neurogenesis while causing widespread neuronal cell death [76]. Together, cell death and prolonged UPR activation in primary ZIKV-infected fetal cortices suggest that proper neurogenesis disruptions underly microcephaly, on top of excessive neuronal cell death. Modeling and

investigations reveal the direct connections between ZIKV infection, ZIKV-induced neurogenesis defects, and UPR deregulation [76].

Neural Cell Culture and Mouse Brain Development

In addition to UPR activation by ZIKV infection in hNSCs of microcephalic brains, other immortalized neural cells and mouse modeling begin to dissect how specific activations contribute to microcephaly and pathologies in those systems. Differential activation of the UPR during ZIKV infection is demonstrated with astrocytoma (CCF-STTG1) and neuroblastoma cells (SK-N-SH). Both demonstrated eIF2a-phosphorylation and increased XBP1s/u ratios, ATF4, and CHOP expression, but increased BIP, phosphorylated-IRE1, and ATF6n were only seen in SK-N-SH cells [184].

Mouse modeling for ZIKV-induced microcephaly parallels the UPR expression seen in the fetal cortices. In those, ZIKV infection causes microcephaly by inhibiting the transition from direct to indirect neurogenesis [185]. At a granular level, in mouse NPCs, ER stress markers (like calreticulin and calnexin) are upregulated [76]. More broadly, there is conservation for increased IRE phosphorylation and nuclear XBP1s expression [184, 185]. Tan et al., *J Neuroinflammation* 2018 reported ATF6 nuclear translocation that was not seen by Gladwyn-Ng et al., *Nat Neurosci* 2018 suggesting that the specific mechanism can be variable even in similar systems. In totality, all branches of the UPR underly specific aspects for ZIKV propagation and have implications for microcephaly and other CZS consequences.

Mechanistic Underpinnings of the UPR in Neurogenesis

In ZIKV infections, one of the significant contributors to microcephaly is the inhibition of the transition from direct to indirect neurogenesis. UPR activation is high during early, direct neurogenesis, and attenuation is the physiological signal for transitioning to indirect neurogenesis and for IP proliferation to occur. During normal neurogenesis, there is excessive neuralization to ensure proper neuronal signaling that, once established, leads to caspase 7-and-12 mediated programmed cell death for unused or redundant neurons. During ER stress, the ability of NSCs in the cerebral cortex to proliferate and survive is impaired by induction of ATF4 and CHOP, while knocking down ATF4 alone restored proper neurogenesis and intermediate progenitor expansion [97]. Mechanistically, UPR inhibition in mice supports individual roles of the UPR for replication and pathologies. PERK inhibition with GSK2656157 reduced ZIKV-induced microcephaly without a reduction in ZIKV infection levels. Similarly, IRE1 inhibition with 4μ8c rescued cortical dimensions but did so while reducing ZIKV levels. 4μ8c treatment also inhibited the PERK-ATF4 branch, suggesting crosstalk may mediate rescue [185].

There are no reports of UPR activation or the role of UPR inhibition in ZIKV infections in any ocular modeling. Even so, minimal studies highlight that programmed UPR activity is critical for proper eye development—the most characterized is lens development. After the initial differentiation of epithelial cells at the anterior surface, proper lens expansion is achieved through continuous lens fiber cell differentiation at the lens equator. UPR activity, as seen by BIP and PDI expression, is high early in lens fiber cell differentiation, with activity decreasing

through maturation and enucleation of lens cells [186]. Although disruptions to lens expansion alter ocular development, it is currently unknown if UPR activity plays a role in retinal progenitor differentiation or retinal neuron development like neural progenitors in the brain. Independently from ZIKV infection, altered UPR activity underlies congenital glaucoma and other genetic diseases whose clinical manifestations resemble signature aspects of CZS symptomology in the eye [4, 23, 24, 130]. The interplay between the role of the UPR in genetic ocular diseases, proper neurogenesis, and ZIKV infections lays the foundation for investigating the role of the UPR in retinal organoids and RPE.

Results

ISR Modulation Impacts ZIKV Replication and Tropism in Human Retinal Cell Types

A class of the significantly dysregulated gene networks identified from scRNA-Sequencing of ZIKV infected, day 60 ROs involved cellular stress, the unfolded protein response, and the integrated stress response. Ultimately, a reduction in input required by the ISR is through global translational arrest with eIF2a phosphorylation that can occur from the convergence of either PKR, PERK of the UPR, GCN2, or HRI [181, 187]. The UPR comprises three transmembrane sensors that activate specific downstream effectors to relieve the protein folding stress and return cellular homeostasis. From the differential expression between ZIKV-negative or ZIKV-positive cells (see Chapter 3 Figure 2), representative UPR and ISR genes were expressed in a dot plot to identify how these networks are dysregulated at a

granular level. There is minimal change for all three sensors *ATF6* (ATF6), *ERN1* (IRE1), and *EIF2AK3* (PERK) from infection, with slight upregulations for *ATF6* and *ERN1* and downregulation for *EIF2AK3*. Almost all UPR effector genes are upregulated in ZIKV+ cells as seen with *ATF4* (as a proxy for PERK), *XBP1* (as a proxy of IRE1, although splicing cannot be detected in our assay), *ATF3*, and higher in the cell death effector *DDIT3* (CHOP). Unlike the others, *HSPA5* (BIP) is severely downregulated in ZIKV+ cells but appears heavily upregulated under mock conditions. Two other ER chaperones, Calnexin (*CANX*) and Calreticulin (*CALR*), are upregulated in ZIKV+ samples (**Fig 2a**). HSV1 samples have a distinct profile with downregulations to all UPR-related genes, other than minimal upregulations to *ATF3* and *EIF2AK3* (**Fig 2b**). Both ZIKV and HSV1 infected cells have high expression *PPP1R15A*, a gene involved with the dephosphorylation of eIF2a, helping to resolve global translational arrest (**Fig 2a,b**) [188]. Single-cell RNA sequencing supports the activation of all three branches of the UPR in ZIKV+ cells. How the independent branches of the UPR are involved in inhibiting ZIKV replication or rescuing RO health remain unknown.

Patterns of UPR activity for ZIKV replication and consequences can be distinct depending on the cell type infected. To investigate the role of the UPR on ZIKV infections in the context of the human retina by pretreating day 60 ROs with UPR inhibitors (4μ8c, ISRIB, Ceapins, HA15, C16) for 2 hours before infecting with ZIKV at an MOI of 1, replaced with media exchange. Supernatants for each treatment were collected at 48 hpi and tittered to measure the impact of UPR inhibition on

ZIKV replication against DMSO controls. Comparatively, there is a reduction in ZIKV titer by about 50% for 4μ8c, Ceapins, and HA15, with slightly less inhibition for C16. Unlike the others, ISRIB treatment does not impact or increase ZIKV titers up to about 15% over DMSO (**Fig 2c**). ROs under the same conditions at 48hpi were collected and stained for surface expression of NS2B in whole-mounted ROs to confirm replication levels. Uninfected samples reside at the same level as secondary controls. The ratio of quantified NS2B fluorescent units (FU) from inhibition parallels titers for all conditions except for ISRIB dropping below and C16 above the DMSO control (**Fig 2d**). In addition to replication, UPR modulation can impact cell death from ZIKV. Hoechst and propidium iodide (PI) staining determined viability in whole-mounted, inhibitor-treated ROs at 48hpi. Compared to about a 7.5% PI positive in DMSO control samples, the percent PI positive was reduced from all inhibitor treatments, with significant reductions for C16, followed by Ceapins and HA15 under 5%, then 4μ8c and ISRIB treated samples with high variability around 5% PI positive (**Fig 2e**). Unlike with ROs, RPE ZIKV-titers are reduced to a lesser extent from 4μ8c, ISRIB, and Ceapin treatment (**Suppl. Fig 1a**). AlamarBlue metabolism was used as another metric of health. Between time 0 and 48 hpi for each condition, UPR inhibition rescued metabolism towards uninfected controls with stepwise increases in AB fluorescence from 4μ8c (significantly below uninfected) to ISRIB, Ceapins, HA15, and C16 with the largest rescue (**Suppl. Fig 1b**). Overall, single UPR inhibition generally decreases viral titer and rescues RO health to an intermediate amount.

Inhibiting a single target often creates a muted phenotype, so the interplay between the UPR branches for ZIKV replication and cell death induction must be explored through (at least) dual inhibition. At 48hpi, ZIKV titers were reduced by about 70% for 4μ8c +Ceapins treatment, 30% for 4μ8c+Ceapins, but increased by about 20% for ISRIB+Ceapins treatment (**Suppl. Fig 1c**). Similar trends are seen in NS2B FU from whole mounted ROs with 4μ8c+Ceapins near the uninfected baseline except for ISRIB+Ceapins treatment now quantified below DMSO controls (**Suppl. Fig 1d**). Hoechst and PI viability is significantly rescued for 4μ8c+ISRIB dual inhibition close to uninfected baselines at about, with slightly less inhibition for ISRIB+Ceapins and 4μ8c+Ceapins with more variability at (~2%, 3%, and 4% respectively) (**Suppl. Fig 1e**). There was partial rescue of metabolism in AB fluorescence from dual inhibited ROs with the most rescue from 4μ8c+ISRIB, slightly less for ISRIB+Ceapins, and 4μ8c+Ceapins to significantly lower amount to uninfected control ROs (**Suppl. Fig 1f**). The increased complexity from dual inhibition muddles direct interpretations, demonstrating the variability in rescue between overlapping pathway inhibition to single inhibition experiments.

Inhibition of PERK and PKR are Candidates for the Success of Protracted Zika Virus Infections in ROs

In cases of microcephalic modeling for ZIKV, infections caused extended UPR activation, disrupting normal cortical expansion by forcing progenitors into neurons directly [98]. Day 60 ROs were pretreated with UPR inhibitors, infected at an MOI of 0.1, and then tracked over 14dpi in inhibitor-containing media to investigate if UPR

inhibition plays a role in long-term growth deficits and cell death induction. Phase imaging of the ROs amongst each treatment condition at day 0 and 14dpi demonstrates a darkening of RO color and loss of outer edge integrity by varying amounts for all conditions compared to uninfected controls, with minimal disruption for C16 treatment (**Fig 3a**). When the 2D surface area is quantified, uninfected ROs have variable size changes with minimal growth. The average RO SA decreased from 4μ8c treatment, with ISRIB and Ceapins slightly above that and close to DMSO control sizes. RO SA increases for C16 treatment and a smaller amount for HA15 treatment (**Fig 3b**). Once again, alamarBlue fluorescence was used for long-term metabolomic changes over 14 dpi. The only significant rescue in alamarBlue fluorescence is from ISRIB treatment. Otherwise, 4μ8c and Ceapins are close to ZIKV-infected baselines at around 0.65 change to uninfected, with stepwise increases for HA15 to about 0.74 and 0.76 in C16 treated samples (**Fig 3c**).

Once again, to help adjust for compensatory signaling from inhibition, we measured the effect of dual UPR inhibition on 2-week infected ROs. As before, representative PC imaging of 14dpi infected ROs demonstrates a darkening of RO color with the most outer integrity loss sustained from 4μ8c+Ceapins treatment, less so for 4μ8c+ISRIB, and minimally in ISRIB+Ceapins treated ROs (**Suppl. Fig 3a**). Conversely, ISRIB+Ceapins treatment has the lowest FC 2D SA average to DMSO treated with an increased SA for 4μ8c+ISRIB and 4μ8c+Ceapin treatments (**Suppl. Fig 3b**). AlamarBlue fluorescence from day 0 to 14 dpi was used as a final indicator of RO health through treatment metabolism. The fluorescence of DMSO-treated

ZIKV-infected samples is reduced to about 0.65 of uninfected controls. ISRIB+Ceapins treatment was the only condition where RO metabolism was nearly completely and significantly rescued from treatment, although it is marginally rescued from 4μ8c+ISRIB treatment.

In contrast, AB fluorescence was decreased from dual inhibition with 4μ8c+Ceapins. Long-term lower MOI infections have more dramatic phenotypes over transient infections, with ISRIB significantly rescuing RO metabolism (**Suppl. Fig 3c**). However, changes in growth may be muted through RO growth variability and variable levels of destruction.

Discussion

Here we demonstrate a cellular stress response activation to ZIKV for the first time in any retinal modeling, especially human stem cell-derived ones. Specifically, we found that (1) scRNA-Seq supports the activation of all three branches of the UPR in ZIKV+ cells of ROs, although *HSPA5* is decreased. (2) 4μ8c, Ceapin, HA15, and C16 treatment all reduce ZIKV titers in ROs by about half, whereas ISRIB may have been advantageous. (3) Inhibition had a reduced effect in RPE than ROs, although titer was still decreased from all three treatments—Ceapin, ISRIB, and 4μ8c treatment (in order from most to slightest inhibition). (4) All UPR inhibitors reduced RO viability from DMSO with the only significant reduction from C16. (5) The health of long-term infected ROs was rescued by ISRIB (only significant) with partial rescues from C16 and HA15 treatments (as based on metabolism).

The Impact of UPR Inhibition on ZIKV Pathogenesis is Semi-Conserved Between Neural and Retinal Organoid Modeling

First, from scRNA-seq in infected ROs, we demonstrated the ability to detect transcriptional responses all three branches of the UPR in response to ZIKV infection. In ZIKV+ cells, there were upregulations in PERK and IRE1 effectors with specific ATF4 and CHOP induction that are highly conserved across brain modeling (primary samples or cell and mouse models) [76, 184, 185]. We compared our data to microcephalic mouse models to better understand the conservation of UPR inhibition on replication and pathology. In ZIKV-infected day 60 ROs, there is a similar conservation of responses for most of the reported players, other than a slight decrease in *ERN1* (IRE1) expression in ZIKV+ cells. As with previous modeling, ZIKV+ cells held small upregulations in *EIF2AK3* (PERK) with further upregulation for its effector *ATF4*. Subsequently, the downstream cell death effector *CHOP* is heavily upregulated from infection. Even so, the inhibition of PERK and IRE1 impacts viral replication and the consequences from infection similarly in ROs as in other modeling, exemplified by Gladwyn-Ng et al., 2018 [add citation]. In IFN-a/b receptor KO mice, PERK inhibition showed no change or slight increase in ZIKV levels. The same is seen for PERK-inhibited titers in ROs – although quantified NS2B levels were reduced by 50%. The trend holds for IRE1 inhibition as the ZIKV level in mice and titers in RO are reduced by 50% (with only a 25% reduction in NS2B levels in ROs), suggesting the conservation in mechanisms with RO.

In addition to reduction in replication, inhibition of either PERK or IRE1 has near-complete rescue of brain size [185]. Although disrupted neurogenesis is a

significant player in microcephaly, cell death is involved. Therefore, cell death was used as a proxy for brain size compared to the downstream consequences of infection in ROs. Neither treatment had the same effect in ROs, with a 42% rescue from PERK inhibition and 53% with IRE1 inhibition at 48hpi. Analysis of the change in RPC levels from treatment may explain the difference in rescue efficiency between the two, and those experiments could reveal differential mechanisms for UPR-related pathologies. An MOI reduction to produce subtler phenotypes may be needed for similar results. A better comparison would be the change in surface area instead of cell death for ROs against brain size. There may have been crosstalk in mice, where IRE1 inhibition reduced the PERK-ATF4 signaling, suggesting that it may still be mediating brain size rescue. Our work suggests a similar combinatorial effect is conserved with ROs with a more significant reduction in cell death from IRE1 inhibition, although it needs to be directly confirmed.

One striking gene expression profile in our scRNA-seq was *HSPA5* (BIP). In day 60 ROs, *HSPA5* (BIP) is downregulated in ZIKV+ cells. This data strongly supports the conservation of BIP attenuation typical for flaviviral infections in ROs that is previously unreported in retinal modeling (as demonstrated in A549 cells but not conserved in CCF-STTG1 astrocytes) [182-184]. Two other ER chaperones, calnexin (CANX) and calreticulin (CALR), function to relieve stress and protein aggregation by increasing protein assembly and folding efficiency. Unlike BIP, (CANX and CALR are upregulated in ZIKV+ cells, suggesting distinct roles in infection to maximize efficiency. Individual UPR components are indispensable in the ZIKV life cycle, driving replication by disconnecting the dampening effect of BIP

and increasing throughput by upregulating CALX and CALN. BIP inhibition in ROs with HA15 reduced ZIKV titers and viability by about 50%, suggesting that initial BIP activity is required for ZIKV establishment before the attenuation with infection progression. Our results parallel A549 cells where pharmacological pretreatment impacts viral infection, but infection is unaffected once established [183]. If pretreatment of UPR inhibitors caused an incomplete infection inhibition, titer persistence could be explained by the heterogeneity between cell types or bypassing inhibitor penetration when infection progresses into internal RO regions.

Understanding the mechanisms disconnected in ISR signaling will require untangling various proteomic and phosphorylation level shifts. Single-cell proteomics would identify differential regulation and timing of translational modulation in both ZIKV-infected and bystander cells. Subsequent phosphoproteomic analysis would give more detail regarding changes in pathway activation on top of changing global expression levels. The comparison of expression profiles from the RNA, protein, and phosphorylation levels would further the understanding of ZIKV modulation at specific points across transcriptional, translational, or activation-state levels.

Cell Type Differences Likely Contribute to the Inconsistent Pathogenesis

Different cell types have differential expression of UPR-related proteins based on function or differentiation state, suggesting differential UPR inhibition between cell types could contribute to incompleteness. Differential activation in UPR responses has been demonstrated in direct comparisons between cell types. For example, neuroblastomas (SK-N-SH) and astrocytomas (CCF-STTG1) have

increased XBP1s/u ratios and ATF4 and CHOP levels in response to ZIKV. They also have differential activation from ZIKV with only phospho-eIF2α significantly increased in SK-N-SH cells, but CCF-STTG1 cells have increased BIP, phospho-eIF2α, phospho-IRE1, and ATF6n [184]. Differences can also be seen between mouse models where both have phospho-IRE1, XBP1 with nuclear localization of XBP1s, and ATF6n was only detected in one [184, 185]. Cell type differences exist between A549 cells and ROs for the role of UPR on ZIKV replication. In A549 cells, PERK inhibition (GSK2606414) alone does not affect ZIKV replication unless in combination with ATF6 inhibition (Ceapin-A7). Ceapin treatment alone inhibited the later stages of infection [183]. Similarly, in our ROs, there was no change in titer from PERK inhibition and titer inhibition from ATF6 inhibition alone. Unlike A549 cells, dual inhibition with ATF6 did not affect RO titers. Additional scRNA-seq replicates to acquire significantly more of each RO cell type would demonstrate differential UPR temporal or expression activation.

As with the attenuation of ATF4 in the transition to indirect neurogenesis, XBP1s, on the other hand, is increased during brain development, explicitly functioning for neurite outgrowth and maturation [97, 189]. Neuronal maturation impairments by Tm treatment during RA-induced neuronal differentiation can be rescued by ERAD through HRD1, highlighting the role of IRE1-XBP1s [97]. RA signaling is critical for eye development in presumptive RPCs at the optic vesicle early in development, with later developmental signaling in rod PRs and RPE [190]. It would be fascinating to inhibit HRD1 to investigate its contribution to ROs and RPE tropism, especially as it is implicated in the partial rescues of RO phenotypes.

UPR Dysregulation in Inherited Eye Diseases Parallel CZS Symptomology

All three branches of the UPR are implicated in different clinical pathologies with overlapping manifestations and dysregulations with CZS. Although not directly linked, convergent pathologies may arise from the specific timing of aberrant UPR activity with infection. Lens subluxations are a consequence of CZS that UPR-dysregulation could cause during ZIKV infection [186]. In the developing lens, ER-resident chaperones BIP and PDI are highly expressed, along with ATF6, ATF4, phospho-PERK, and XBP1 upregulations in newly forming fiber cells. Direct disruption of the fibrous filaments connecting the ciliary body with the eye's crystalline lens underlies a CZS case [35]. Lens fiber cell dysregulation is implicated across developmental diseases, including myopia and cataracts, two ocular CZS consequences. Newly forming fiber cells of embryonic lenses highly express ER-resident chaperones, BIP, and PDI while also explicitly expressing ATF6, ATF4, phospho-PERK, and XBP1, which is typically linked to alpha-crystallin [186]. In cataract patients, those with high myopia had decreased a-crystallin and induction of GRP78, ATF6, p-eIF2a, p-IRE1, and XBP1s [191]. Altered UPR activity is implicated in paralleling occulo developmental consequences beyond lens dysregulation.

ATF6 and OASIS Signaling may have Dual Function in Retinal Pathologies

Our scRNA-seq in ZIKV-infected day 60 ROs highlights a similar upregulation in ATF6 as PERK (or decrease for IRE1) in ZIKV+ cells. Unfortunately,

there are limited reports on ATF6's involvement in neurological consequences or the ZIKV life cycle. In one case, ATF6n translocation was seen from ZIKV infection in astrocytoma cells (CCF-STTG1) [184]. ATF6 may have a broader implication for ZIKV infection as inhibition in A549 cells attenuates the late stages of ZIKV replication [183].

In addition to the canonical UPR sensors, ATF6, IRE1, and PERK that can sense ER stress is a fourth, old astrocyte, specifically induced substance (OASIS). OASIS is a transmembrane protein in the CREB/ATF family of transcription factors. Similarly to ATF6, OASIS is cleaved at the Golgi apparatus upon ER stress to induce BIP and other UPR target gene expression in the nucleus [97]. OASIS and ATF6 share regions with high sequence similarity that do not extend to the luminal domain. They likely have unique regulatory mechanisms as mutations to the luminal domain of OASIS do not affect Golgi translocation or proteolytic processing as occurs from ATF6 mutations [192, 193]. OASIS activity in astrocytes and RPE within the eye could provide an additional layer of complexity underlying retinal pathologies [194]. Their interplay is suggested across a wide range of clinical manifestations in CZS.

Although not present in ROs, microglia are one of the ways that ZIKV infiltrates immune-privileged regions like the brain and retina [195]. Aberrant ATF6 activity in microglia may be involved with autoimmune encephalitis (inflammation of the brain and spinal cord), similar to that in CZS, AZI, and GBS [97]. As microglia are present in the ganglion cell and inner plexiform layers, this may be involved in retinopathies associated with ZIKV, also seen by increased infiltration in ZIKV-

infected mouse retinas [196]. In future experiments, ZIKV-infected microglia could be introduced to RO cultures to probe the role of ATF6 in pathogenesis alterations.

As the primary light-sensing cells of the retina, photoreceptor dysfunction and death lead to blindness and other visual defects [32]. PR health is dependent on RPE and the heavily vascularized underlying choroid [197]. Another CZS feature that may be directly or indirectly linked to UPR dysregulation is altered choroidal vascularization [198]. There are a few mechanisms where ATF6 signaling is implicated in vascularization changes. Choroid vasculature endothelial cells are mesodermally derived, and ATF6 activation suppresses human embryonic stem cell potency while enhancing mesodermal fates [199, 200]. Inversely, patient-derived iPSCs retain pluripotency and have impaired mesodermal differentiation with the loss of ATF6 function [200]. The authors specifically state that ATF6 may contribute to abnormal retinal vascular development in visual disorders, supporting the role of ATF6 in similar CZS-related vasculature changes [200, 201]. RPE secrete vascular endothelial growth factors (VEGF), a growth factor critical for proper choriocapillaris development [202]. Fetal RPE infected with ZIKV have increased levels of VEGF secretion [129]. After ER stress in RPE (ARPE-19), OASIS effectively and directly binds the VEGF promoter to induce neovascularization, consistent with changes in retinal vascularization seen from ZIKV infections [119, 194, 200]. Future experiments could focus on how the interplay between OASIS and ATF6 within RPE or across retinal development contributes to CZS presentation heterogeneity.

Another conserved characteristic between CZS and AZI with implications for UPR dysregulation is myelination disruptions [97, 203]. Dysfunction and death in

oligodendrocytes and Schwann cells, the myelinating cells of the CNS, and PNS result in demyelination. The ON is myelinated by oligodendrocytes, beginning in the first trimester before full coverage at seven months and subsequent thickening [204]. Myelination disruptions are present in other CZS targets, suggesting that demyelination underlies ON thinning or visual alterations from late-stage infections and can develop after birth. Astrocytes are the glial cells of the CNS that are critical for supporting oligodendrocyte health and myelination. OASIS signaling theoretically would support the ON as it is required for glial cell (astrocytes) differentiation and confers a protective role against hypoxia or ischemia-induced injury and death [97]. Within myelinating cells where OASIS signaling is present, like the oligodendrocytes surrounding the ON, CHOP has a noncanonical, antiapoptotic role under pathological ER stress, suggesting neuronal demyelination and death are from unique mechanisms during prolonged ZIKV infections [97].

Paralleling Clinical Symptomology and UPR Activity Between CZS and Genetic Disease Counterparts

PR layer thinning is another characteristic of CZS. Consequences from long-term ZIKV infections are PR layer thinning and significant cone PR and RGC loss, most prominently at peripheral sites [31, 201]. The role of ATF6 in PR and cell fate specification is highlighted by two genetic diseases: achromatopsia (ACHM) and cone-rod dystrophy (CRD). Both diseases are caused by an impaired ability of ATF6 to sense misfolded proteins because of a mutation in the luminal domain. People with ACHM have colorblindness due to a lack of cone PR function with morphological consequences in the fovea (cone-containing region of the eye), with

some patients entirely lacking a foveal pit [193, 205]. CRD is characterized by progressive cone-to-rod functional loss. CRD patients also have a missing foveal pit and foveal hypoplasia consistent with the loss of foveal reflexes, like in CZS [206]. Interestingly, peripheral cones may persist in ATF6-associated ACHM patients, indicating a potential role in CZS where consequences often discretely affect the central and peripheral retina [23, 205].

In a rare disease of the anterior corneal epithelium, Meesman epithelial corneal dystrophy (MECD) patients present with ocular symptoms similar to AZI and CZS with photophobia, blurred vision or foreign bodies, with ruptured epithelial cysts at the corneal surface. In MECD patients and mouse models, the proapoptotic UPR markers CHOP and Caspase 12 are activated with the highest upregulations in lens crystallin [207]. UPR activity is also suggested to cause congenital glaucoma and raise intraocular pressure, other attributes of CZS in the eye [4, 208]. Patients with primary open-angle glaucoma (POAG) have raised intraocular pressure from loss of function mutations in UPR regulators almost entirely related to IRE1 and XBP1s commonly dysregulated in ZIKV infections [76].

A high level of complexity in stem cell-derived tissues and their organization would be required to recapitulate all aspects of CZS pathologies in the eye. The role of the UPR in the individual components, or the interplay between different cell types, would further our understanding of the variability across the diversity of pathologies. Changes to the proper expansion of lens fiber cells are responsible for pathologies resembling those in CZS. ZIKV RNA was detected in mice in all eye regions, including the lens [209]. Advances in differentiation protocols for stem cell-

derived lens fiber cells open an exciting avenue to further our understanding of the interplay between UPR dysregulation in different human stem cell-derived ocular models [210].

Figures

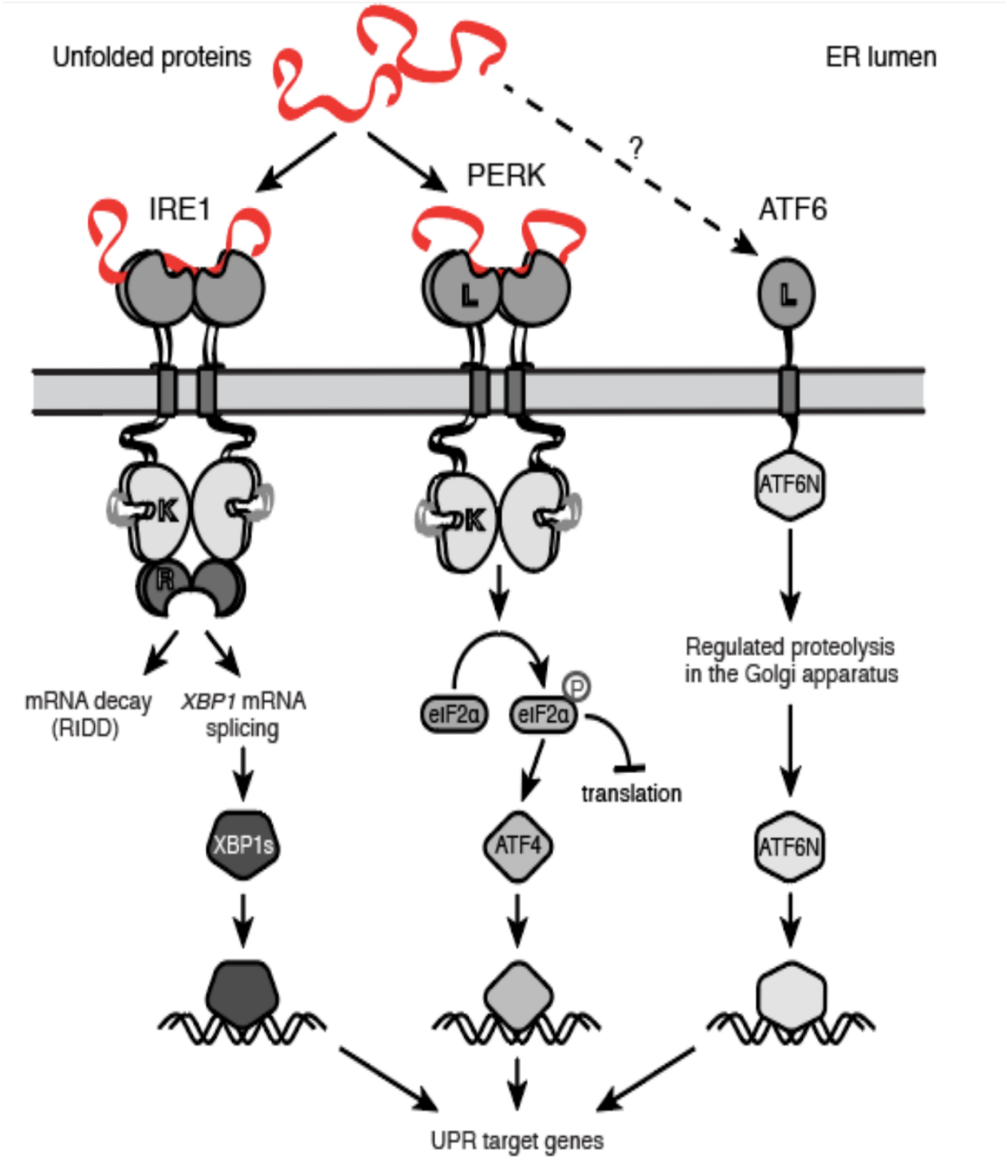


Figure 1. The mammalian unfolded protein response. Three transmembrane sensors, IRE1, PERK, and ATF6 and their signaling outputs upon activation. (Figure from Solley, 2020 [211]; originally from G. Elif Karagöz et al., *Cold Spring Harb Perspect Biol* 2019 [180]).

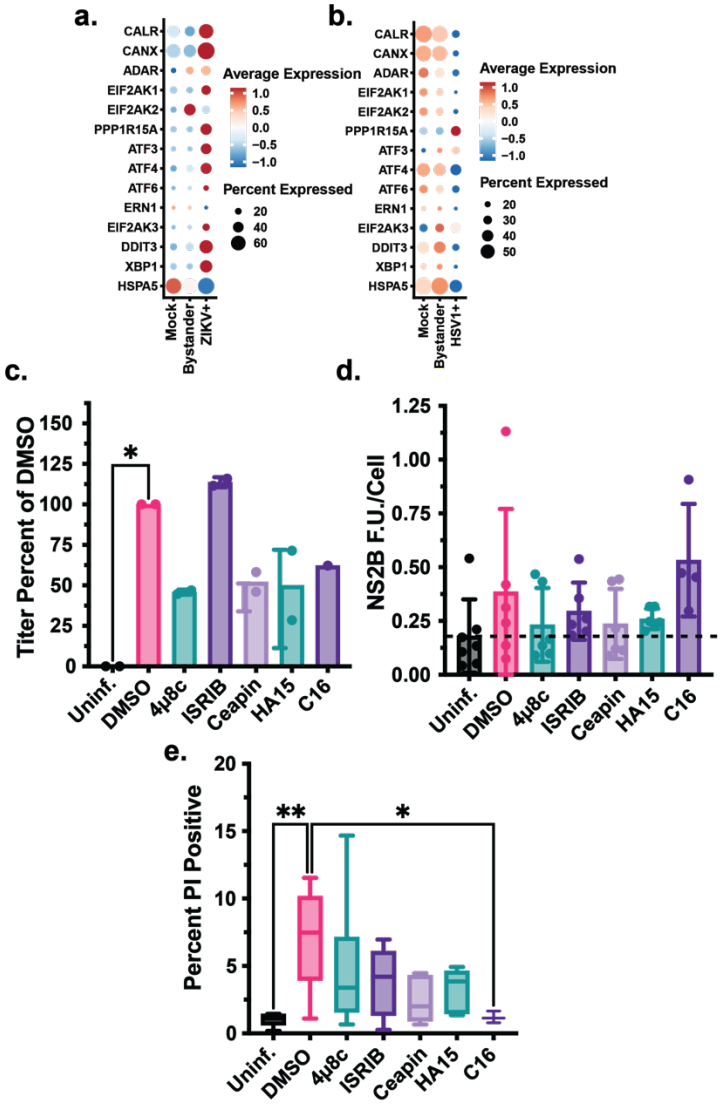


Figure 2. The Integrated stress network is critical for Zika virus infection and replication. a,b. Dot plots of expression changes in stress-related genes in response to ZIKV (**a**) and HSV1 (**b**) infection status. **c.** Analysis of ZIKV titer as a percent of DMSO-treated for UPR inhibitor-treated, day 60 RO supernatants at 48 hpi (n=2 from 4 RO; p=0.0151 uninfected vs DMSO; 2way ANOVA). **d.** Quantification of ZIKV NS2B fluorescence units per cell from inhibitor treatment in whole mounted day 60 ROs (n=6 regions from 3 RO, C16 n=4 regions from 1 RO). Dashed line is secondary control fluorescence level. **e.** Quantification of the percent propidium iodide positive cells in UPR inhibited ROs infected with ZIKV at 48hpi (n=6 regions from 3 RO. p=0.0035 uninfected vs DMSO; p=0.0187 DMSO vs C16;

2way ANOVA). All ZIKV infections were at an MOI of 1. Data in this figure are shown as the mean ± s.d.

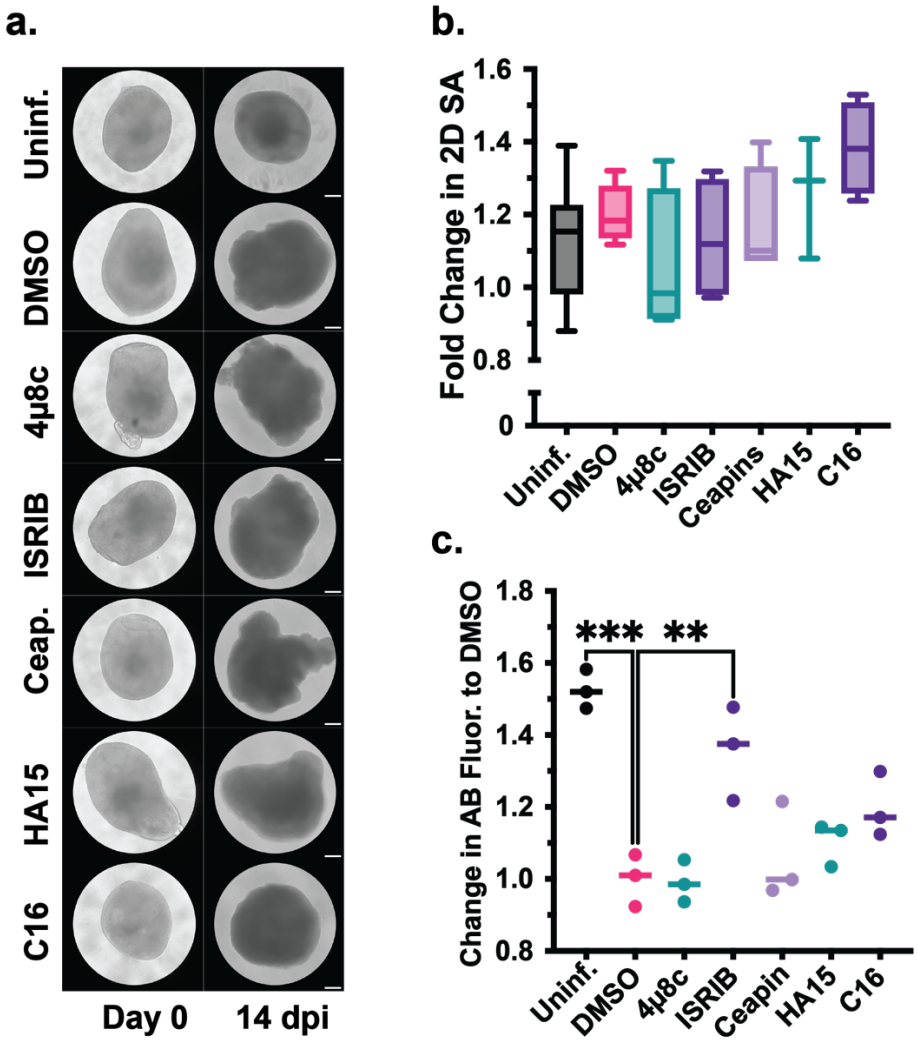
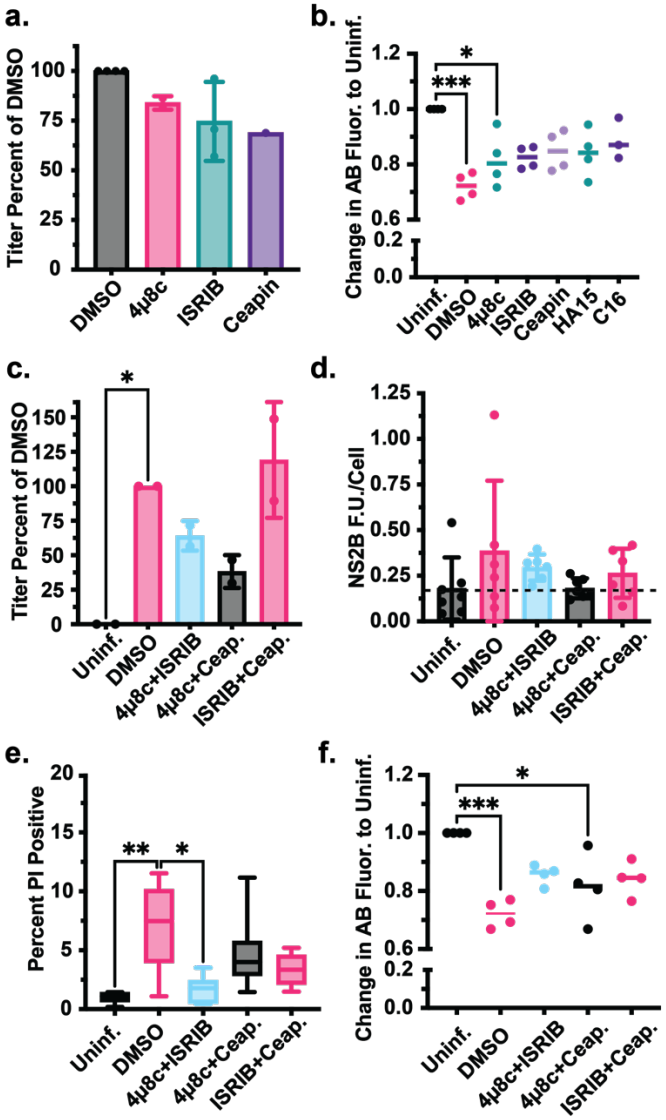
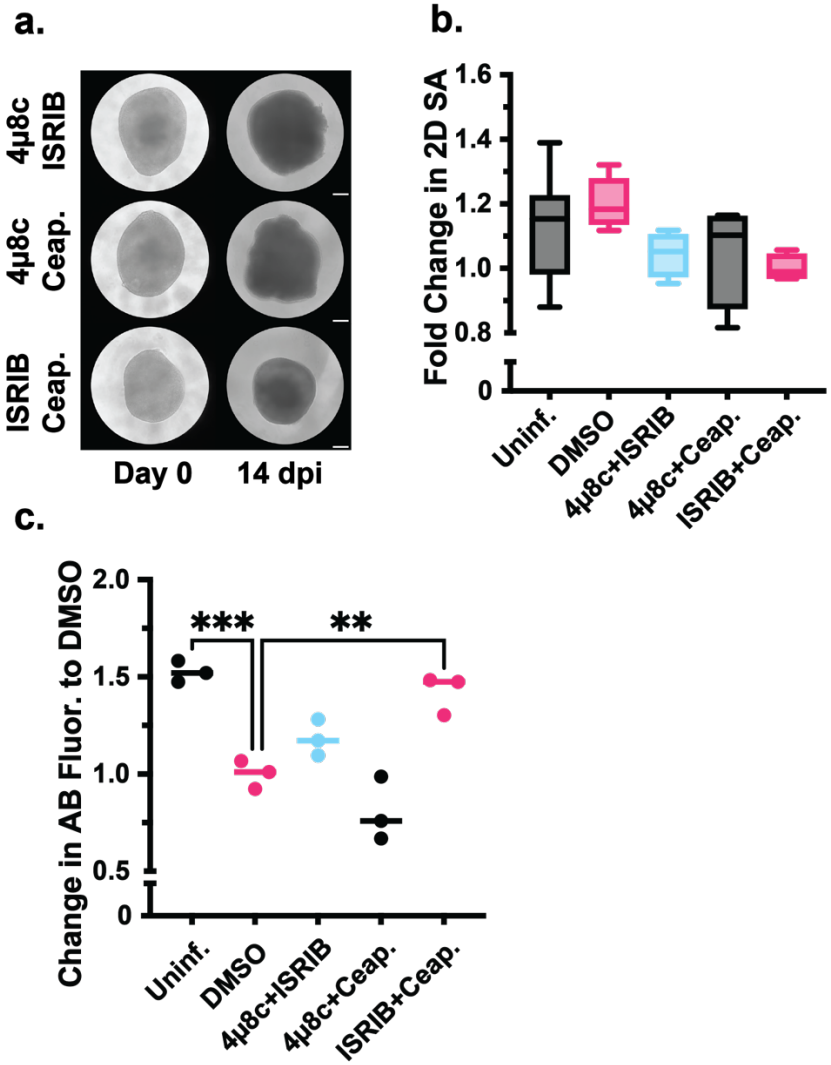


Figure 3. Inhibition of the UPR response with ISRIB or C16 treatment mitigates long term RO health deficits from ZIKV. a. Brightfield imaging of UPR inhibited day 60 ROs 0 and 14 dpi. 200μm Scale bars. **b.** RO size was quantified by the fold change in 2D surface area for individual organoids from day 0 (n=3). **c.** Quantifying the fold change in alamarBlue fluorescence for UPR inhibited ROs from 0 to 14dpi (n=3. p=0.0001 uninfected vs DMSO; p=0.0076 DMSO vs ISRIB; 2way ANOVA). All ZIKV infections were at an MOI of 0.1. Data in this figure are shown as the mean ± s.d.



Suppl. Figure 1 Legend. a. Analysis of ZIKV titer as a percent of DMSO control treatment for inhibitor-treated RPE supernatants at 48 hpi (n=2). **b.** quantification of the fold change in alamarBlue fluorescence for individual, UPR inhibited day 60 ROs compared to uninfected (n=4. p=0.0004 uninfected vs DMSO; p=0.0425 uninfected vs 4μ8c; 2way ANOVA). **c.** Analysis of ZIKV titer as a percent of DMSO for supernatants of dual inhibited day 60 ROs at 48 hpi (n=2 from 4 RO; p=0.0151 uninfected vs DMSO; 2way ANOVA). **d.** Quantifying ZIKV NS2B fluorescence units per cell from dual inhibitor treatment in whole mounted day 60 ROs (n=6 regions from 2 RO). **e.** Quantification of the percent propidium iodide positive cells in dual UPR inhibited ROs infected with ZIKV at 48hpi (n=6 regions from 3 RO. p=0.0035 uninfected vs DMSO; p=0.0171 DMSO vs 4μ8c+ISRIB). **f.** Quantification of the fold

change in alamarBlue fluorescence for dual UPR inhibited day 60 ROs compared to uninfected. Dashed line is secondary control fluorescence level. (n=4. p=0.0004 uninfected vs DMSO; p=0.0375 uninfected vs 4μ8c+Ceap; 2way ANOVA). All ZIKV infections were at an MOI of 1. Data in this figure are shown as the mean ± s.d.



Suppl. Figure 2 Legend. a. Brightfield imaging of dual inhibited day 60 ROs 0 and 14 dpi. 200μm Scale bars. **b.** RO size was quantified by the fold change in 2D surface area for dual inhibition (n=3). **c.** Quantifying the fold change in alamarBlue fluorescence for UPR dual inhibited ROs from 0 to 14dpi (n=3. p=0.0015 DMSO vs ISRIB+Ceap; 2way ANOVA). All ZIKV infections were at an MOI of 0.1. Data in this figure are shown as the mean ± s.d.

Chapter 5. Type I Interferon Alpha and Beta Ameliorate Zika Infections in Retinal Organoids

Summary

The interplay between host antiviral immune responses and viral evasion mechanisms is crucial in determining the outcome of viral infections, including Zika virus (ZIKV). Despite growing evidence surrounding key genes for conferring widespread antiviral immunity, their activation and impact on the ZIKV in the retina remain underexplored. Through single-cell RNA sequencing of ZIKV-infected retinal organoids (ROs), we discovered significant activation of the immunorestrictive genes IFI6 and ISG15 alongside an enhanced interferon alpha and beta pathway signaling. IFNα and IFNβ treatment effectively suppresses ZIKV replication and improves cell survival in ROs, highlighting the protective role of interferon signaling against ZIKV. This study confirms the protective role of interferon signaling against ZIKV in retinal models and emphasizes the critical role of bystander immune activation within the complex 3D structure of ROs.

Introduction

Overview of the Immune Response

The ability to respond to pathogenic assault is critical for the survival of any individual and, by extension, species. The human immune system comprises both a rapid responding, nonspecific innate immune and a long-term, antigen-specific adaptive immune response. The antiviral immune responses activate specific

pattern recognition receptors (PRPs) that bind different pathogen. The PRPs bind specific pathogen structures known as pathogen-associated molecular markers (PAMPs) that do not exist on native cells. The different PAMP-dependent PRRs include toll-like receptors (TLRs), retinoic acid-inducible genes (RIG)-I-like receptors (RLRs), NOD-like receptors (NLRs), and cyclic CMP-AMP synthase (cGAS) [212, 213]. The innate immune response utilizes those for rapid antigen detection and phagocytosis activation by either fast-acting neutrophils or macrophages. In mammals, TLR-stimulated responses are one of the oldest evolutionarily, working to modulate molecule expression to ring the alarm for the innate immune response and initiate adaptive responses [213]. These are critical for ZIKV infection success or deterrence. A representation of these responses is presented in **Figure 1**.

The adaptive immune response is the antigen-specific immune response, including memory development for future challenges by the same pathogen. CD4+ and CD8+ T cells arise from a standard lymphoid progenitor population in the bone marrow and act as coreceptors, uniquely binding invariant sites for MHC class II or I on antigen-presenting cells (APCs), respectively. MHC class I molecules are expressed on nearly any nucleated cell and bind self-generated and cytoplasmic intracellular pathogenic antigens presented to CD8+ T cells. MHC class II molecules are explicitly expressed on specialized APCs like B cells or dendritic cells and present ingested protein-derived antigens for CD4+ T cells [214]. For ZIKV, the overall mechanism supported is an initial rapid and transient increase in plasmablast and CD38(high)CD8+ T cells initiating/preceding an increase in intermediate monocyte populations. The intermediate phenotype plays a critical role

in the ZIKV-mediation of the adaptive immune response seen by increased intermediate monocyte populations, plasmablast induction, and a substantial activation of CD8+ T cells with distinct phases during acute infections [215]. The primary focus of our thesis is on the innate immune system as it is present for acute infection retinal organoids, which are out of the context of adaptive immune timing and cellular mediators and the circulatory system. Specific immune pathways are critical for the host defense response to pathogens.

Antiviral Immune Responses

Although specific PRRs activate different innate immune pathways, there is a high order of overlap and crosstalk between them following activation. One of the foremost host antiviral pathways for the detection of foreign cytosolic nucleic acids is through the cyclic GMP-AMP (cGANP) synthase (cGAS), leading to the activation of the protein stimulator of interferon genes (STING) and amplifying the downstream type I IFN production. Once stimulated, STING drives a strong, IFN-I dominated response. With cytosolic DNA detection, cyclic GMP-AMP (2'3' cGAMP) will bind STING directly, producing type I IFN through TBK1 phosphorylation. Type I IFN production through TBK1 is alternatively driven by the viral RNA activation of RIG-I, focusing STING interactions towards the mitochondria by activating mitochondrial antiviral signaling proteins (MAVS) [216].

RLRs are a primary sensor for viral dsRNA in the cytoplasm. They can be broken into three distinct classes: RIG-I, melanoma differentiation-associated gene 5 (MDA5), and laboratory of genetics and physiology protein 2 (LGP2). Conventionally, upon recognition, RIG-I and MDA5 interaction with MAVs activates

interferon regulatory factors 3 and 7 (IRF3/7) in combination with nuclear transcription factor-kB (NF-kB) [217]. Overall, MAVS acts as the primary hub for the signal transduction from RIG-I-like receptor inputs modulating both proinflammatory and antiviral genes (including IFNs (alpha and beta) and ISG production) [216, 217]. The production and release of type I IFNs alpha and beta propagate the inflammatory response by binding neighboring cells and activating the Janus kinase-signal transducer and activator of transcription (JAK-STAT) network.

JAK-STAT signaling plays roles in initiating antiviral states, stimulating adaptive immune responses, and recruiting immune cells depending on the conformation of the JAKs (JAK1/2/3 and Tyk2) from cytokine receptor binding. STAT1-STAT2 heterodimers will bind IFN-regulatory factor 9 (IRF9), forming the ISGF3 complex that stimulates the production of many ISGs through interferon-stimulated response element (ISRE) binding. The ISGF3 complex is critical for all inherent antiviral defensive responses like OAS and MX1[218]. Lastly, eukaryotic translation initiation factor 2 alpha kinase 2 (or PKR) is another antiviral pathway that senses dsRNA (like ZIKV replication intermediates) before inhibiting global translational machinery and inducing a balancing act between viral clearance or apoptosis [219]. The activation and inhibition of these pathways are critical to the success of ZIKV infection and tissue-specific infectivity. There are currently no reports of PKR in any retinal modeling for ZIKV.

A few genes of interest (like IFI6 and ISG15) are gaining traction for having broad-spectrum antiviral properties [220-226]. In cell culture models, others have been identified as capable of mitigating ZIKV and HSV1 infections. There is a

divergence in anti-ZIKV-and-HSV1 responses between cell culture models and organoids, as seen with brain organoids (see Chapter 1). Therefore, retinal organoid (RO) modeling is crucial for a deeper understanding of antiviral responses in the eye [104]. Previously, scRNA-seq of ZIKV infection in human dendritic cells demonstrated the effectiveness of capturing antiviral responses [227]. A specific view of the immune modulation around both in retinal organoids remains unknown. This chapter investigates the immune responses triggered by ZIKV and HSV1 in human stem cell-derived retinal organoids from scRNA-Seq (**Chapter 3**). We demonstrate distinct immune profiles between the two viruses and probe the role of type I interferons on ZIKV infections in ROs.

Results

scRNA-Seq Reveals Strong Bystander Antiviral Immune Responses to Zika Virus in Retinal Organoids

The immune response, or evasion of it, plays a critical role in the success of viral infections. Pathway enrichment analysis from the significant DEGs in Chapter 3 for ZIKV+ cells in day 60 ROs identified the dysregulation of various immune and viral infection-related responses. The most DEGs on the volcano plots from the same sample set were the immune-related genes ISG15, IFI6, B2M, HLA-A/B, and IFITM1. To understand the expression of those and the role of specific gene players within enriched networks, representative immune genes were expressed in a dot plot of expression between mock, ZIKV-pos, and ZIKV-neg bystander cells from 48-and-96 hpi. Most of the immune genes are represented at a higher amount in

bystanders over ZIKV+ cells, including IFI6, ISG15, IFITM1/3, STAT1, and EIF2AK2, amongst others, although ZIKV+ cells have minimal downregulation. ZIKV+ cells have higher expression of HLA-A/B/C and a lesser amount of IFIT1. B2M is expressed higher in ZIKV+ cells, although bystander levels are closer than other genes (**Fig 2a**).

When the same analysis is applied to the scRNA-Seq samples for HSV1 infected, day 200 ROs, the pattern is unique from ZIKV, where there are large downregulations in most immune genes with mild upregulations for most bystander cells with one major exception where that pattern is flipped is for HLA-B (**Suppl. Fig 1a**). To understand the distribution of the percent ISG by infection status over time using density plots. When the ZIKV expression is plotted against the percent ISG after 24 hpi, the max peak density is lower in bystanders compared to ZIKV+ cells, where the flattening of the curve demonstrates an increase in the percent ISG in bystander cells over time as seen by a rightward shift in the bystander curve on the density plot (**Fig 2b-d**). Sample profiles have a distinct pattern to ZIKV when applied to day 200, HSV1-infected ROs where there is no change in ISG density in bystander populations. In contrast, HSV1+ cells have a bimodal peak with the ISG density building to match bystander curves by 20 hpi before a leftward shift in ISG density at 24 hpi, consistent with transcript degradation by HSV1 (**Suppl. Fig 1b-e**). In summary, scRNA-sequencing can identify distinct mechanisms of immune modulation between ZIKV and HSV1 infections of ROs.

To understand how specific the ISGs identified in the volcano and dot plots like IFI6 (**Fig 2e**) with similar patterns to other bystander genes like ISG15, IFITM1,

and IFITM3 (data not shown) that are overrepresented in bystander populations, the specific ISG expression (blue) is plotted against ZIKV expression (red) for each cell represented as a dot within the UMAP: red cells have high ZIKV alone, blue have high ISG alone, purple when both are high and grey when both are low. The expression profiles for all 4 ISGs against ZIKV are consistent, with little overlap between ZIKV and ISG expression with minimal regions of purple dots. Regions with a high density of ZIKV-positive cells are mainly in a subset of MGCs and most other clusters in a limited capacity. Unlike with ZIKV, there is widespread ISG expression in other subregions of MGCs, PRs, RPCs, and all other clusters. One cluster with high variability and overlap between ZIKV and ISGs is the ISG cluster, which is generated over time. Box plots were employed to quantify the ISG expression between mock, bystander, and ZIKV+ cells at 48-and-96 hpi. The highest expression of any of the ISGs in mock populations is from IFI6 (**Fig 2f**) or, to a lesser extent, ISG15 (**Fig 2g**) and IFITM3 (**Suppl. Fig 1f**), although expression in ZIKV+ cells follows the same trend. In totality, ZIKV infection within the 3D, multicellular context of ROs causes an upregulation of antiviral genes, most prominently IFI6 and ISG15, within uninfected bystander populations over ZIKV+ cells.

Type I Interferons Alpha and Beta Confer an Antiviral Effect to ZIKV in ROs

IFN alpha and beta signaling is the top enriched pathway identified from 48-and-96 hpi ZIKV-infected day 60 ROs (Chapter 3). ROs were treated with those interferons (IFN), alpha and beta, to investigate the antiviral activity of type I IFNs

and mimic bystander stimulation seen in Fig 1. Day 60 ROs were treated with IFNα and IFNβ for 2 hours before ZIKV infection at an MOI of 1 and replaced with IFN-containing media. Tittering of 48hpi RO supernatants demonstrates a nearly complete inhibition of ZIKV production from both IFNα and IFNβ, with IFNβ production just above that (**Fig 3a**). As a proxy for replication, quantification of NS2B staining in whole mounted ROs fixed at 48hpi supports tittering data as the NS2B FU/cell is near the secondary baseline for uninfected, IFNα, and IFNβ treated samples, unlike for mock-treated ROs (**Fig 3b**). In addition to inhibiting viral replication, overall RO health was improved, seen by viability with Hoechst and PI staining and metabolism via alamarBlue at 48hpi. Mock-treated samples are around 7.5% PI positive, significantly reduced to about 4% from IFNα and 2% from IFNβ treatment (**Fig 2c**). Metabolism by alamarBlue fluorescence increases from ZIKV infection but is rescued from a significant reduction to ~0.9 FC of uninfected in IFNα treated samples and to about baseline from IFNβ (**Fig 3d**).

Discussion

In summary, we have shown (1) scRNA-Seq identified upregulations for individual players in the type I antiviral signaling pathway in bystander cell populations. (2) High bystander expression of *IFI6* and *ISG15* support antiviral roles in ROs. (3) Type I interferon alpha and beta (IFNα and IFNβ) treatments ameliorate ZIKV titers, and (4) rescue RO health.

The specific genes overrepresented in bystander cells include *IFI6, ISG15, IFITM1, IFITM3, MX1, EIF2AK2,* and *STAT1*, whereas only a few genes like *B2M* and *HLA-A/B/C* are skewed towards ZIKV+ cells. Previously, the expression of

many innate immune genes was reduced in younger ZIKV-infected iRSC cultures [129]. scRNA-seq of ZIKV infection in dendritic cells highlights bystander activation for type I interferons [227]. Similarly, at a single cell level, infection in ROs results in high stimulation in bystander cells, with little to no decrease in ZIKV+ populations, although bulk assay likely mutes the effect and ignores bystander restriction. Our data expands the knowledge of immune responses to ZIKV and HSV1 in organoid modeling and into the mechanisms underlying infection as RO differentiation (and by proxy development) progresses.

Pathway enrichment analysis on the significant DEGs between ZIKV+ and ZIKV-neg samples highlight type I IFNα/β signaling. Honing on those, we demonstrate the strong antiviral effect of IFNα and IFNβ to ZIKV in ROs as seen by near complete inhibition of ZIKV titers and NS2B in IHC at 48hpi. Generally, our RO data parallels that seen in ZIKV-infected brain organoids where type I IFN treatment results in a significant reduction in ZIKV levels and rescue of transcriptional changes, suggesting they have conserved antiviral effects and paralleling mechanisms across neural organoid models [104]. Although similar, in brain organoids, the effect was more prominent for IFNβ, whereas for us, the reduction in titer was slightly more considerable for IFNα, highlighting the nuances between the models. In the future, it is imperative to investigate the contrasting immune profiles between HSV1 and ZIKV in our data. Critically, for HSV1 in brain organoids, unlike with ZIKV, IFNα improved structure and suppressed HSV1 levels better than IFNβ; therefore, interferon responsiveness will likely vary between the two in ROs. IFN-λ has also conferred a similarly decisive antiviral role to ZIKV in primary human

vaginal and cervical epithelial cells (as did IFNα and IFNβ) [228]. IFN-λ effectively blocks HSV1 and ZIKV in human corneal explants [229]. Although IFNα and IFNβ confer a robust antiviral effect on ZIKV in ROs, future experiments comparing IFN-λ on ZIKV and HSV1 in ROs will help bridge our understanding of retinal and corneal infections and to those in other immune-privileged reservoirs.

Of the expressing immune DEGs, *IFI6* and *ISG15* are two of the highest differentially expressed genes identified for ZIKV-infected ROs in Chapter 3. IFI6 and ISG15 are a couple of emerging antiviral immune factors. In summary and at nauseum: IFI6 is budding as an antiviral factor for flaviviruses and many other families of viruses, including hepatitis B (HBV), Kaposi's sarcoma-associated herpesvirus (KSHV), human immunodeficiency virus (HIV), and coxsackie virus (CAV), amongst other [220, 221, 224, 225]. It is heavily conserved for flaviviruses as the antiviral effect has extended to ZIKV, DENV, WNV, Yellow Fever (YFV), Japanese encephalitis virus (JEV), and Chikungunya virus (CHIKV) in various modeling [220-225]. In addition to IFI6, ISG15 is implicated as an antiviral for flaviviruses (JEV, DENV, YFV, and WNV) and broadly across a multitude of viruses as well including HSV1, Chikungunya virus (CHIKV), coxsackie virus (CAV), Human immunodeficiency virus (HIV), ebola virus (EBV), avian sarcoma leukovirus (ASLV), and Kaposi's sarcoma-associated herpesvirus (KSHV), Kunjin virus (KUNV) [224-226].

The role of ISG15 in establishing ZIKV infections, immune evasion, or inhibition of cell death within the context of human retinal organoids is unknown. Our scRNA-seq has identified bystander ISG15 activation supports an antiviral role

in human stem cell-derived retinal organoid modeling. Our data are congruent with other ocular modeling where ISG15 stimulation in primary or stem cell-derived RPE and human corneal explants supports ISG15 antiviral activity to ZIKV [128, 230]. Furthermore, ISG15 deficiency in murine modeling reduces the effectiveness of the antiviral response, with phenotypes paralleling clinical manifestations like chorioretinitis with increased retinal cell death and higher replication levels [52]. ZIKV infection also induces ISG15 and other type I IFN responses stem cell-derived and primary RPE. One exception is a proviral role for ISG15 for hepatitis C virus (HCV) in patient samples and cellular modeling, suggesting that could be the case for some viruses or between cell types [231, 232]. Our experiments showcasing the protective effects of IFNα and IFNβ pretreatment suggest a vital antiviral role in ROs, as pretreatment mimicking a bystander effect would stimulate ISG15, supporting an antiviral against ZIKV. To confirm an antiviral role, an ISG15 reporter can be used to sort stimulated cells (produced after infection or from IFN treatment). A subsequent infection in those cells against ISG15-negative cells would test that directly.

Future experiments utilizing ROs differentiation from stable and inducible ISG15 and IFI6 KO or overexpression stem cell lines would allow vital comparisons of their antiviral effects in human retinal models [233]. Those lines would simulate either bystander activation priming or infectious disconnection of ISG15 and IFI6 and their particular role in ZIKV infection and replication. The potential for differential roles is exemplified by ISG15 knockdown inhibiting ZIKV replication, although it did not affect the viral binding or entry in multiple cell lines, suggesting

distinct antiviral mechanisms [234]. Parallel modeling with RPE differentiated from the same modified stem cell lines would be critical for directly comparing the differential pathogenesis mechanisms with and to wider-ranging implicated cell lines prevalent in literature. In addition, repeating the same interferon treatment experiments in RPE would be advantageous in understanding the interplay with ROs similar to the development of the neural retina in utero.

Although *ISG15* and *IFI6* are upregulated in bystander cells in our ROs, unlike *ISG15*, which has slight upregulation in ZIKV+ cells, *IFI6* has a slight downregulation in ZIKV+ cells. The ER remodeling, critical for establishing viral replication factories, is one of the ways ZIKV is insulated from the immune system [235]. A CRISPR activation screen with ZIKV infection revealed that IFI6 is an ER-localized membrane effector of the IR against ZIKV through the stabilization of BIP [222]. That supports the idea of an antiviral IFI6 activity in ROs by preventing ER membrane invaginations, playing a prophylactic role against replication factory establishment, as proposed by Richardson et al. 2018 [insert citation #]. We expect a correlation between the expression profiles in our scRNA-seq data for IFI6 and BIP stabilization having a bystander antiviral role. Unlike bystander *IFI6* upregulation (little change ZIKV+), *HSPA5* is heavily downregulated in ZIKV+ cells (with increased expression in ZIKV-neg cells), suggesting they may have similar relative expression profiles relative to mock. Immunofluorescence or stable reporters for BIP, IFI6, ZIKV, and ER proteins could be used to determine the interplay in ROs by comparing ZIKV-infection levels and changes in expression

patterns from interferon treatment, BIP inhibition, and genetic perturbations against BIP and IFI6.

A key backbone of the antiviral defense against dsRNA is the interplay between protein kinase regulated by RNA (PKR; *EIF2AK2*) with adenosine deaminase acting on RNA (ADAR) as a critical throttle for the broader immune response. PKR is one of four kinases feeding the intrinsic stress response (ISR) that activates in response to dsRNA and leads to global translational arrest. In some cases, ZIKV replication depends on PKR, seen by a loss in replicative potential for ZIKV in cells with impaired PKR, independently of type I interferon or NF-kB signaling and cell viability [236]. We have demonstrated bystander activation of *EIF2AK2*, supporting an antiviral function for PKR in ROs. Rapid responses to pathogens require rapid, robust, and largely indiscriminate signal expansion, but unregulated amplification would lead to autoimmune damage to the host. The ADAR family of proteins includes three members (ADAR1-3) that are RNA unwindases. However, most specifically, ADAR1 and ADAR2 express enzymes with adenosine deaminase A-to-I editing activity that destabilize RNA structures (viral and host), dampening these responses to prevent autoimmune damage. In doing so, ADAR is acting in a proviral capacity harnessed by ZIKV for evasion from PKR and antiviral aspects of the immune system, specifically [237, 238]. Interestingly, moderate ADAR stimulation is consistent between bystander and ZIKV+ cell populations (Chap. 4 Fig 2a). These results could be explained by the duality of ADAR activity where in bystander primed cells, it plays an antiviral role (with PKR

stimulation) while instead destabilizing PKR to promote infection in ZIKV+ cells, as seen from our scRNA-seq.

One of the outstanding questions from our scRNA-seq data is how bystander stimulation occurs, as there is little to no expression of any *IFNA* or *IFNB1* (data not shown). PKR plays a vital role as a positive effector that amplifies the production of IFN [239]. High PKR levels in bystander cells of ROs suggest that PKR activity may drive bystander stimulation and perpetuate antiviral effects on neighboring cells. Utilizing a live PKR reporter in combination with a reporter for ZIKV could demonstrate PKR activation in and around regions of infection in real time [181]. Stimulation of type I IFN production and release is downstream of STING and RIG-I/MAVs activation, which could also affect bystander responses [218]. Initially, to determine if any immunoprotective molecules that could confer a bystander effect are released by conditioning media in ZIKV-infected ROs or RPE before viral inactivation use as a treatment on new, uninfected ROs or RPE. If there is a responsiveness from treatment, or even if the stimulated phenotype is too dilute to have an effect from media conditioning, it could be identified with an enzyme-linked immunosorbent assay (ELISA) along with changes in any other immune signaling during infection.

Immune signaling and viral evasion mechanisms depend on changes at the proteomic and phosphorylation level. A pitfall of scRNA-sequencing for interrogating signaling pathways in general and immune pathways in particular is their dependence on proteomic and phosphorylation changes. Therefore, investigating that activation in ROs would help understand dysregulated networks and if or how

those are specific to ZIKV infection. Ideally, comparing expression profiles on the protein level from single-cell proteomics with the scRNA-seq data would identify differential regulation and timing between changes on the initial RNA level and the efficacy of downstream translation of those factors. Additionally, quantitative and site-specific phosphoproteomic analysis would demonstrate how these pathways are activated. Finally, comparing those in combination with ELISA assays for released factors as the actual cellular response would gain insight into immune responses to and modulation from ZIKV in ROs across all levels of regulation and signaling. By combining these techniques with the previous IFN treatment and single-gene perturbations, the broader role of those IFNs and specific roles of IFI6 and ISG15 individual human retinal cell types in a heterogeneous organoid population.

Figures

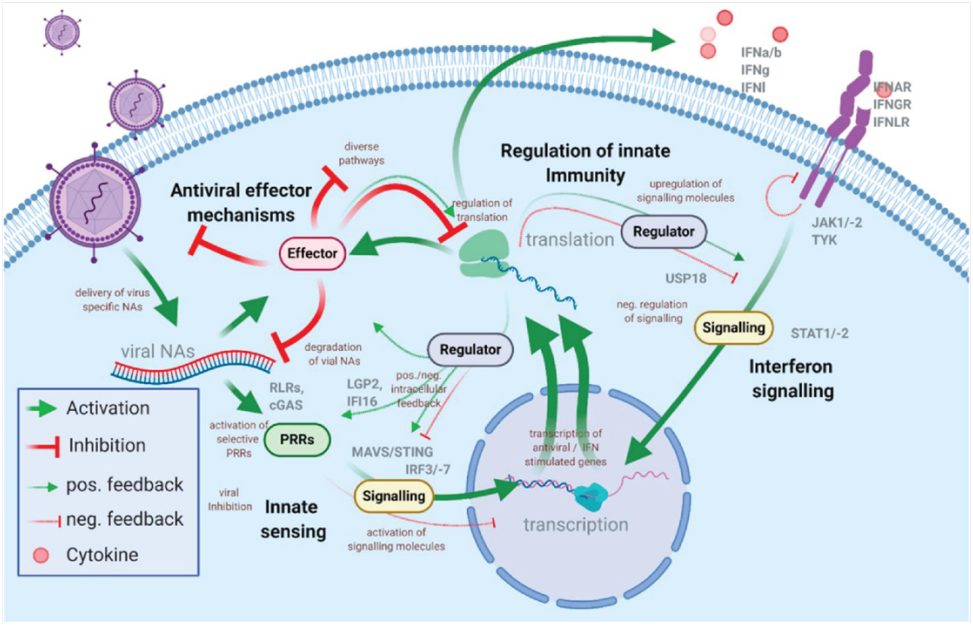


Figure 1. Antiviral Immune Responses. The antiviral immune response requires the harmonization of pathogen-detection triggering complex cascades of regulators and effectors. Those effectively result in paracrine and autocrine interferon signaling, ultimately priming the cell into an antiviral state. (Taken from Krey et al., *Viruses* 2020 [240]).

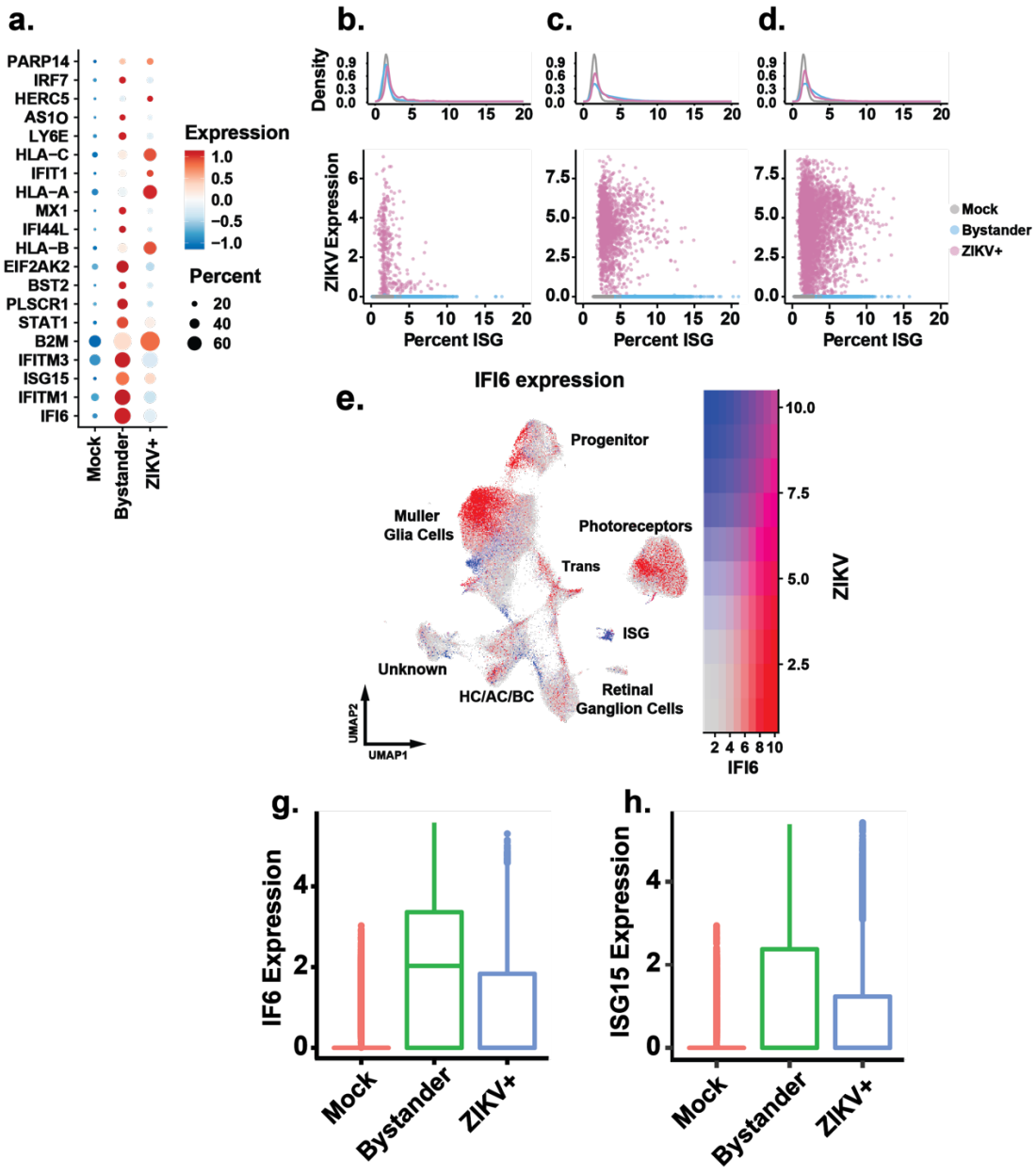


Figure 2. ZIKV induces strong bystander antiviral immune signaling. a. Dot plots for immune stimulated genes based on ZIKV infection status. **b-d.** Two-way plots of ZIKV against ISG expression with respective density plots based on infection status at 24 (**b**), 48 (**c**), and 96 hpi (**d**). **e.** Co-expression plots for the correlation of 2 factors overlayed on UMAP clustering for IFI6 expression against ZIKV. **f,g.** Box plots for IFI6 (**f**) and ISG15 (**g**) expression levels by ZIKV infection status.

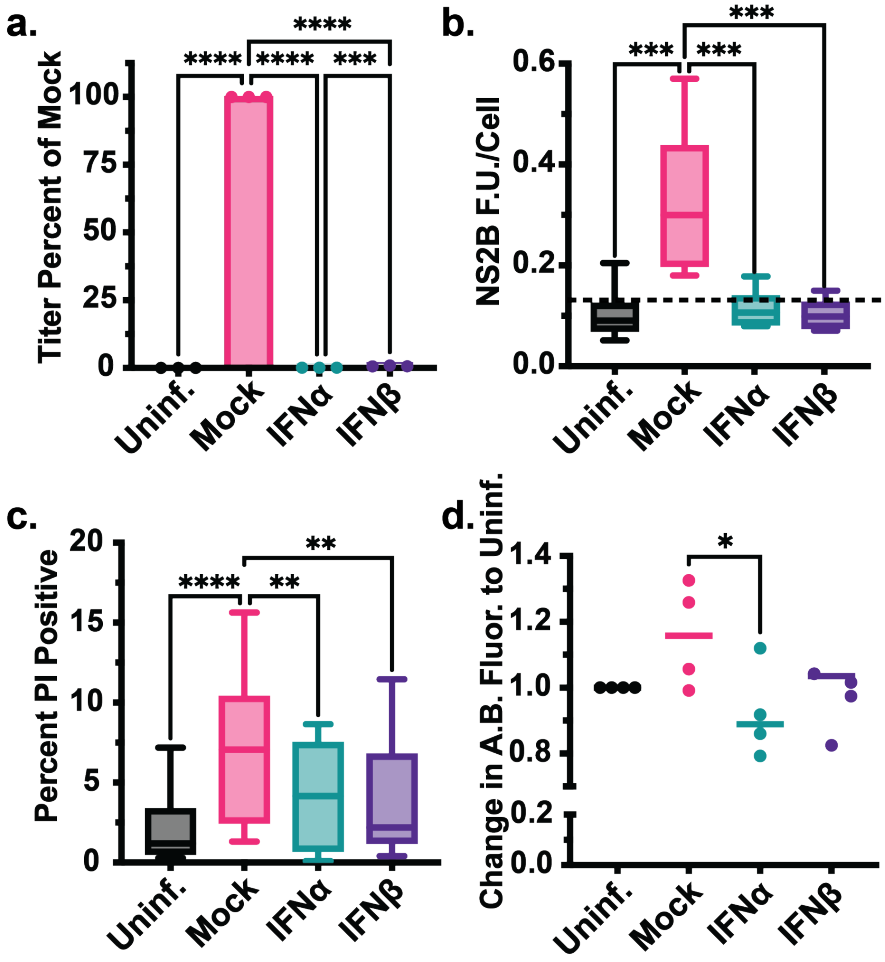
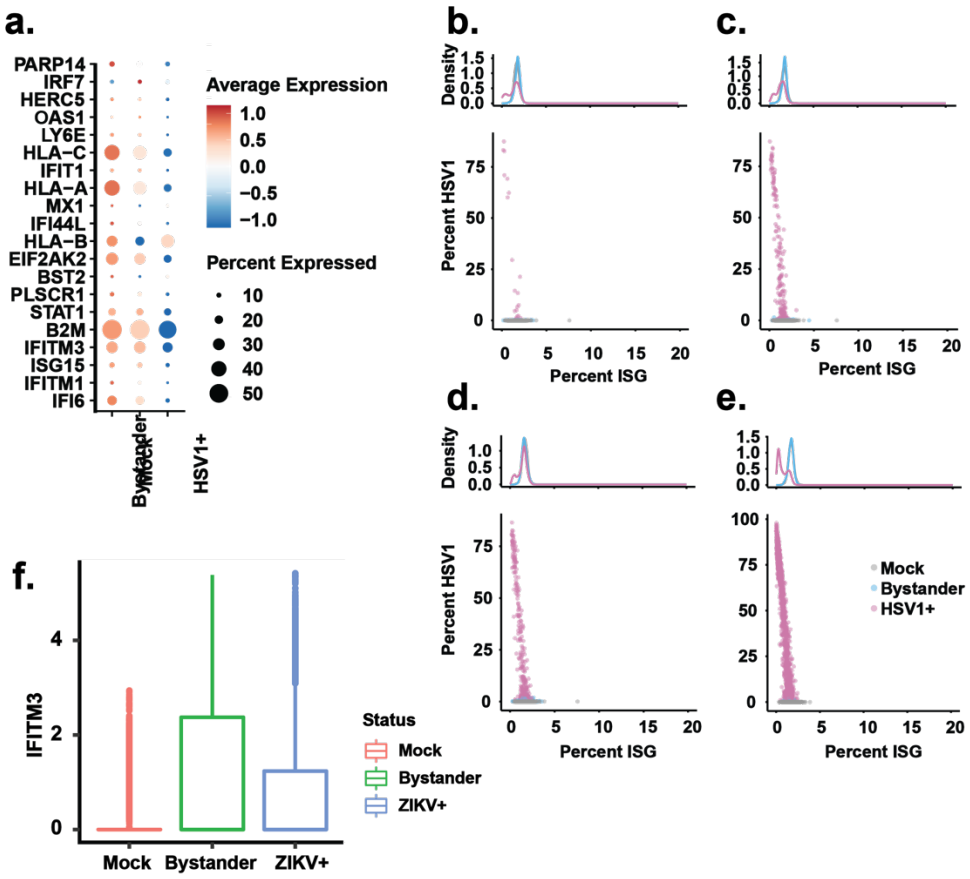


Figure 3. Interferon alpha and beta ameliorate ZIKV infection in ROs. a. Analysis of ZIKV titers as a percent of Mock for IFN-treated, day 60 RO supernatants at 48 hpi (n=3 from 8 RO. **** is a pValue <0.0001; 2way ANOVA). **b.** Quantification of ZIKV NS2B fluorescence units per cell from IFN-treated in whole mounted day 60 ROs (n=6 regions from 2 RO. p=0.0007 uninfected vs Mock; p=0.0009 Mock vs IFNα; p=0.0005 Mock vs IFNβ; 2way ANOVA). Dashed line is secondary control fluorescence level. **c.** Quantification of the percent propidium iodide positive cells in IFN-treated ROs infected with ZIKV at 48hpi (n=11 regions from 4 ROs. p=0.0021 Mock vs IFNα; p=0.0061; **** is a pValue <0.0001; 2way ANOVA). **d.** Quantification of the fold change in alamarBlue fluorescence for individual, UPR inhibited day 60 ROs compared to Mock (n=4 RO. p=0.0410 Mock vs IFNα; 2way ANOVA). All ZIKV infections were at an MOI of 1. Data in this figure are shown as the mean ± s.d.



Suppl. Figure 1. a. Dot plots for immune stimulated genes based on HSV1 infection status. **b-e.** Two-way plots of HSV1 against ISG expression with respective density plots based on infection status at 8 (**b**), 16 (**c**), 20 (**d**), and 24 hpi (**e**). **f.** Box plots for IFITM3 expression.

Chapter 6. Concluding Remarks

From the initial isolation of Zika virus (ZIKV) in Uganda in 1947, sporadic ZIKV outbreaks highlight the worldwide spread before the explosion of cases between 2015 and 2016 in the Americas [1]. It is imperative to continue studying ZIKV as the crossover from zoonic reservoirs will likely cause the next global pandemic, and ZIKV is one of the viruses on the WHO list with the greatest public health risk [241]. Furthermore, shifting symptomology and reservoirs in the Americas could dramatically affect the severity of future outbreaks, as seen between the 2004 SARS and the 2019 SARS-CoV-2 outbreaks. The implications for ZIKV infections in the eye remain paramount for future outbreaks, as retinal screening is a better diagnostic indicator of CZS than head circumference [48]. Although infections early in utero have a worse prognosis, there is a high variability in symptomology in Congenital Zika Syndrome cases, with a diversity of consequences across a wide range of tissues. These are particularly apparent with brain and retinal manifestations where diverse clinical pathologies can arise from similar in-utero infection timings. Neural and eye development is highly complex, with differentiation, organization, and maturation extending beyond birth. The same pathways (like UPR) altered from ZIKV infection in adults are often utilized in different contexts during development , adding an additional layer of complexity to *in-utero* infections as demonstrated by the widespread manifestation in ocular pathologies.

Our work in ROs has been critical for contextualizing the current understanding of retinal ZIKV infections from other models in human cell-derived

contexts. Directly, our work demonstrated high susceptibility of RPC populations in day 60 ROs, compounding previous work in human stem cell-derived retinal cells in younger organoid cultures [129]. Uniquely, our work suggests RPC fate loss from infection, offering mechanistic support behind severe pathologies. In those same ROs, for the first time, we reported ZIKV infection in RGCs, supporting the fidelity of ROs for bridging clinical pathologies and other retinal modeling. Infection of those critical cell types at day 60 and permissiveness persistence out to day 200 ROs supports the fidelity of ROs for modeling retinal Zika virus infections. Our parallel work with HSV1 bolsters ROs and adds to the growing list of viruses modeled in ROs, bolstering the efficacy of ROs across all retinal targeting viruses.

We utilized single-cell RNA sequencing to untangle some of the nuances underlying infection in the complexity of ROs by cell type and infection status. We confirmed that all prospective transcriptionally clustered cell types are permissive to ZIKV. We further uncovered broadly and differentially dysregulated networks in bystander and ZIKV+ cells revolving around cellular stress and type I antiviral immune responses that our further modeling surrounds. The differential activation by infection status seen in our data demonstrates a drawback of bulk assays on infection heterogeneity, especially in models with higher complexities (like organoids). Cellular stress responses play essential roles in neural development and ZIKV infections, although model variability suggests discrepancies between species and cell types. Our work in ROs demonstrates that inhibition of ISR components has far-reaching consequences for ZIKV infection in ocular modeling,

as suggested by the rescues to 14dpi RO metabolism from a lack of translational arrest from ISRIB treatment, amongst others.

Initially, scRNA-seq revealed ISR modulation encompassing all three branches of the UPR and whose activation is dramatically biased towards ZIKV+ cells, with upregulations, especially in effectors, and a downregulation in BIP. It revealed upregulations to the UPR death effector CHOP, supporting its role as one of the cell death mechanisms in ROs. BIP modulation is highly bimodal between models, with growing camps demonstrating activation or repression during infection. We are positing another case of BIP repression in a highly specialized and more human-relevant retinal model. Our results support patterns of UPR activity congruent to primary fetal or mouse CZS brains.

Furthermore, for the first time, the consequences of pharmacological inhibition of specific UPR components on ZIKV infection and pathogenesis were investigated in the retinal systems. Proper IRE1, ATF6, BIP, and PKR signaling is imperative for ZIKV replication as their inhibition reduces ZIKV titers. That is not seen during PERK inhibition from ISRIB treatment. Unlike tittering, all inhibitor treatments rescued cell viability loss, with the most dramatic rescue from PKR inhibition. Together, we demonstrate that all branches of the UPR play a role in ZIKV pathogenesis in ROs, and likely, those pathways have some level of crosstalk during infection.

Another avenue of our work focused on the immune modulation from ZIKV infections, particularly bystander immune signaling. Broadly, scRNA-seq identified the activation of type I antiviral interferon alpha and beta signaling stimulated in

uninfected bystander cells. At a granular level, two of the strongest candidates are budding antiviral factors, IFI6 and ISG15. Although previously unreported in ROs, it is consistent with the antiviral roles against ZIKV in various models and tissues. Specifically, ISG15 in bystander cells of ROs is consistent with the anti-ZIKV role of ISG15 in RPE (primary or stem cell-derived) and corneal explants, suggesting conservation within ocular modeling [52, 128, 229, 230]. We provide the first report on the protective role of interferon-alpha or beta treatment in ocular modeling. In ROs, IFN stimulation leads to a massive reduction in ZIKV production and significant rescue of cell viability. High congruency to ZIKV-infected brain organoids suggests that the antiviral immune activation seems to be conserved across organoid modeling of the immune-privileged, neurological reservoirs. In totality, we were able to further the understanding of the antiviral immune response to ZIKV, specifically supporting previously identified antiviral roles as specific bystander responses to ZIKV infection within the higher compositional and architectural complexities of ROs.

Modeling for the high complexity and interplay from the diversity of utilized pathways, their roles between cell types, and the differential modulation of those in the human developmental space are beyond the capabilities of current stem cell-derived modeling (even ignoring the additional layer of complexity caused by the dysregulation of those as would occur from *in utero* infections). That complexity extends into ocular models, too, due to the high order of complexity in the mature eye alone. So far, ROs have been the most complex human stem cell-derived system for modeling the ocular consequences of ZIKV. Although powerful for

retinal-specific pathologies, retinal development occurs within the context of other cells whose signaling is indispensable for proper retinogenesis. As those tissues are susceptible to ZIKV, RO modeling alone ignores those contributions to pathogenesis. From a pure modeling standpoint, combining multiple stem cell-derived ocular systems with increasing levels of complexity is appealing.

The primary cell types presented in this thesis and implicated in CZS pathologies are RPE, RPCs, and RGCs. Others with a lesser role than those mentioned or responsible for other parallel pathogenesis include microglia, choriocapillaris, lens fiber cells, and corneal cells. The easiest would be mimicking inner blood-retinal-barrier pathogenesis by co-culturing ROs on top of an RPE monolayer, as demonstrated by Akhtar et al., *Stem Cell Res.* 2019 [161]. Co-culturing RPE and choriocapillaris (with or without ROs) would improve our understanding of the mechanisms behind the inner blood-retinal-barrier crossing from the bloodstream during the viremia phase in systems with complex human components corroborating animal modeling. Broder visual dysfunction to retinal-to-visual stimuli reception could be achieved from the fusion of retinal, thalamic, and cortical organoids, creating mature RGC axons responsive to environmental cues [242]. Those could model signaling and connectivity disruptions in the visual system and could theoretically be used to measure the consequences of ZIKV on proper RGC firing. Beyond that, RGC-like projections extending off seeded ROs could be grown through neuronal guiding channels to create a more physiologically relevant optic nerve-like connection to thalamic and cortical organoids in another chamber. Increased orders of tissue complexity would require a multi-tissue chip platform like

those developed for blood-brain-barrier modeling, known as a CUBE device [243]. A CUBE device system could layer a greater level of blood-retinal-barrier components or could be adapted to model-independent ocular cell types to include stem cell-derived lens fiber or corneal cells [210, 244]. Introducing microglia is enticing, as it unveils a final layer of pathogenesis as infected microglia are the physiological infection mechanism for ZIKV infiltration into immune-privileged sites [195]. Stem cell-derived microglia could be differentiated, infected, and then introduced into other culturing conditions, revealing the interplay of cell type-specific microglial interactions to ZIKV-pathogenesis [245]. Combining several stem cell-derived differentiations reduces person-to-person variability underlying any of the differences seen. Although out of the current scope of the field, advancements in organoid complexity in modeling human disease postulated for a virological focus.

Chapter 7. Materials and Methods

Cell Lines and Retinal Organoid Differentiation

All cell lines were cultured at 37 °C with 5% CO2 (vol/vol). Vero (monkey epithelial) and H4 (neuroglioma) were cultured in DMEM containing 10% FBS (vol/vol), 2 mM L-glutamine, and 100 U/mL penicillin/streptomycin. H9 stem cell derived-retinal pigment epithelial (RPE) cells (previously differentiated by Leah Foltz) were expanded with Rho-GTPase (ROCK) inhibition and banked as previously described by Croze et al., *Cells Transl. Med.* 2014 [246]. RPE cells were thawed onto Matrigel-coated plates and cultured in XVIVO-10. Human embryonic H9 and MC166 induced pluripotent stem cells cultured in mTeSR plus on growth factor reduced Matrigel-coated plates. Retinal organoids were generated using a modified version of the Zhong et al. protocol (Chapter 1, Figure 8) [102]. Stem cells were cultured in Aggrewell plates, forming embryoid bodies, rapidly transitioned from mTeSR to NIM, and seeded for 2D culture on day 5. Cultures are sustained in NIM until day 20 when it is changed to retinal differentiation media 1 (RDM1), and until the manual dissection of neural retina domains is done on day 27. Dissected NR domains self-organize in suspension culture, remaining in RDM2 until day 42. ROs were transitioned to RDM3 with the addition of FBS to support long-term culture. The list of cell culture reagents is in **Table 1,** and the media compositions are in **Table 2**.

Zika Virus Propagation and Tittering

ZIKV strain PRVBC59 (isolated Puerto Rico, 2015) was propagated in Vero cells infected at a multiplicity of infection (MOI) of 0.01 and collected 96 HPI with the

addition of 100 mM HEPES. Supernatants were clarified by centrifugation at 350Xg for 5 min, filtered through 45um PVDF membrane syringe filters (Genesee #25-242), and concentrated by about 3X using Amicon Ultra- 15 Centrifugal Filters (Millipore #UCF910096) spun at 1.5xg/10 minutes. Titers were determined by focus assays performed on Vero cells, and 30 HPI was processed using Zika virus envelop antibody staining. Experimentally, viral stocks were diluted in cell-specific media and inoculated at an MOI of 0.1 or 1 for 1 hour in cell cultures and 2 hours for ROs.

Pharmacological Treatment

Pharmacological inhibitor or recombinant interferon treatment stocks were diluted in respective vehicles to the listed concentration (**Table 3**). Pharmacological pretreatments were for 1 hour in cell culture or 24 hours in ROs. Recombinant interferon treatments were for 24 hours in ROs. Post-infection, viral media was replaced with fresh treatment-containing media. All treatments were performed at a 1:1000 dilution from stocks to minimize DMSO toxicity unless otherwise specified. Inhibitory antibodies against AXL or GAS6 were reconstituted as 2X stocks in PBS. H4 cells were treated with GAS6 antibody at 50 or 100 uM for 1 hour in media with or without FBS. RPE and ROs were treated for 1-or-2 hours with an AXL-function blocking antibody or a Goat IgG control at 100ug/mL before infection with ZIKV (MOI 1). After infection, the virus was replaced with basal media before supernatant collection and fixation.

Sample Preparation and Staining

Samples were fixed in 4% paraformaldehyde (PFA). PFA was diluted in cold PBS before a 15-minute fixation for cell cultures. Fixed cells were blocked for 1 hour in PBS with 0.1% Triton-X100 and 3% bovine serum albumin (BSA). Primary antibodies were diluted in a 3% BSA and PBS solution (primary antibody dilution factor is listed in each figure legend), and samples were treated for 2 hours at room temperature (RT). Secondary staining was 1 hour at RT with antibodies diluted in PBS alone.

Retinal organoid fixation was for a minimum of 4 hours in 4% PFA diluted in RDM3. Fixed ROs were stored at 4°C before processing in one of three ways: whole mounts, cryosections, or paraffin-embedded. After fixation, (1) whole-mounted ROs were stained in Eppendorf tubes. Blocking was with 5% BSA, 1% Triton-X100, and PBS solution for 2 hours at RT. Primary antibodies were diluted in the same buffer with overnight staining at 4°C. ROs were bathed in secondary antibodies for 2 hours at RT. Immunostained ROs were transferred to a shallow chamber on 24 mm x 60 mm cover glass created from 5-7 layers of nail polish to make chamber slides. Those are mounted between another smaller cover glass with ProlongGold Antifade Reagent to allow imaging through both halves of the RO. Alternatively, organoids were processed for sectioning and fluorescent immunohistochemistry.

For (2) cryosectioning, ROs are cryoprotected via sucrose penetration before transitioning to optimal cutting temperature compound (OCT): 15% sucrose, 30% sucrose, 100% OCT, all at RT overnight or until RO sinking. ROs were frozen in 100% OCT on a metal block equilibrated to a mixture of dry ice and 100% ethanol

for 30-60 seconds. Long-term storage of blocks was at -20°C. Sections were cut at a 5° angle and 16°C on the Leica CryoStat at 14-20 um onto positively charged slides (VRW #10118-319). Sections were left 48-96 hours at RT and stored at -20°C long-term. Lastly, for (3) paraffin embedding, the fixed ROs are initially embedded in a 2% agarose button. Individual buttons are placed into cassettes for dehydration through 15-minute steps: 65% ethanol (EtOH), 2x 95% EtOH, 2x 100% EtOH, and xylene. After a final quick rinse in xylene, dehydrated ROs are embedded in paraffin for 2x 15-minute rounds. The formalin-fixed paraffin-embedded (FFPE) ROs were sectioned into 4-6 um slices and stored at RT.

Immunostaining protocols for cryo-or-paraffin sections are similar after the initial processing of FFPE sections. FFPE sections are rehydrated oppositely to paraffinization: 2x 10min in xylene, 2x 5min 100% EtOH, 2x 2min 95% EtOH, 2min 65% EtOH, 2min 50% EtOH, before 100% water. Heat-induced antigen retrieval (HIER) was performed for all formalin-fixed, paraffin-embedded tissues using 10mM sodium citrate buffer or Tris-Ethylenediaminetetraacetic acid (EDTA) buffer for 20 min at 100°C. HIER was required in cryosections for specific antigens. After epitope retrieval, the staining process is the same. Slices were incubated in a blocking buffer containing 3% BSA (vol/vol) and 0.1% Triton X-100 in PBS pH 7.4 for 1 hour at RT. Primary antibodies were diluted in 3% BSA (vol/vol) in PBS overnight at 4°C (see **Table 4** for the list of primary antibodies). The appropriate secondary antibodies were diluted in PBS and applied to sections for 2 hours at RT (**Table 5** for the list of stains and secondary antibodies). Slides were washed in PBS with a

final H_2O wash before mounting with ProlongGold Antifade Reagent (Invitrogen Ref. No. P36930). Stained slides were stored at 4°C and protected from light.

Fluorescence Imaging and Quantification

Sections were imaged on a LeicaSP8 Resonant Scanning Confocal microscope. Immunofluorescence image quantification was performed with Imaris (Bitplane) or in ImageJ. After an initial background subtraction based on controls, cell-type marker positivity was quantified by first establishing the total number of cells by the spot generation feature in Imaris for Hoechst nuclei. That assay was repeated for individual marker-positive nuclei, and the colocalization between the two determined the total percent positive. A surface was created against the NS2B signal, and the percentage infected was based on how many of those spots were within or excluded from that region. Relative fluorescence levels were quantified in Fiji based on confocal image z-stacks. Stacks were summed in z project, threshold for positive signal, and then measured for total fluorescence area. When represented on a cellular basis, the fluorescence area was divided by the number of Hoechst-positive nuclei. Final measurements were determined with background subtraction based on secondary controls.

We acknowledge the use of the NRI-MCDB Microscopy Facility and the Resonant Scanning Confocal supported by NSF MRI grant 1625770.

Hoechst and Propidium Iodide Staining

For Hoechst and PI treatment, supernatants were collected or discarded, ROs were washed 2x in PBS, then incubated in Hoechst (10 ug/mL) and Propidium Iodide (1 ug/mL) in RDM3 for 1 hour at 37ºC and 5% CO2. After the incubation,

ROs were washed 2x in warmed PBS and fixed in 4% PFA at room temperature for 4 hours. Organoids were imaged on a LeicaSP8 confocal via whole-mount imaging or through a 35mm glass bottom dish. The percent PI positive was quantified using Imaris (Bitplane). The total cell number was established with the spot generation feature for Hoechst nuclei. This was repeated for PI, and total PI-positivity was determined by the colocalization between the two.

Quantification of 2D Retinal Organoid Surface Area via BF Microscopy

Long-term size change was followed over two weeks by imaging individual ROs with an EchoRevolve microscope (https://discover-echo.com) at 10X magnification. The 2D surface area was determined in ImageJ by converting the images to 8-bit, followed by measurements of a tracing of the outer edge using the freehand selection tool. The change was determined by indexing the individual ROs at each timepoint compared to the initial size measurement.

alamarBlue Reagent Assay

Individual ROs were incubated in 1:100 dilutions of alamarBlue in RDM3 for 4 hours in acute infections (up to 96 HPI) or 24 hours for long-term infections. Metabolism was measured by resorufin fluorescence (excitation at 560 nm and emission at 590 nm) produced by resazurin reduction from cellular metabolism. Metabolism for individual ROs was measured by comparing fluorescence readings at respective timepoints against the T0 readings. Readings were an average technical duplicate of resorufin fluorescence measured on a BioTek Synergy H1 Microplate Reader.

scRNA-Seq Analysis

4-6 ROs for each sample were dissociated with papain to a single cell (sc) suspension. At least 6,000 were collected and processed for scRNA sequencing using the 10X genomics platform sequenced in the NovaSeq system [165]. To capture and amplify the ZIKV transcript, we incorporated two ZIKV-specific primers in the scRNAseq reaction mix (see Chap. 3 Fig 3a). 5% Vero cells were spiked into the final cell suspension for quality control and uninfected cell validation. Exact cell numbers per timepoint and replicate are listed (see Chap. 3 Fig 3b). All sequencing analyses were performed by Dr. Zachary Aralis [159].

Flow Cytometry

2-3 ROs were dissociated and filtered to a single-cell suspension. The cells were resuspended in ice-cold methanol, fixed for 15 minutes, washed 2x in PBS, and then pelleted at 4ºC in PBS. The cells were resuspended in PBS with 0.1% Triton X-100 and 3% BSA for 1 hour at RT. Primary antibody staining was in PBS with 3% BSA following the listed antibody concentrations (**Table 4**) overnight at 4°C. Secondary antibodies were diluted in PBS at 1:2500 and on the cells for 1 hour at RT. After cells were washed and resuspended in PBS, sorting was performed on an Attune NxT Acoustic Focusing Cytometer.

Statistics and Figure Preparation

Statistics were performed using Prism 10 software with the specific statistical tests reported in the figure legends. Plots were generated in Prism 10 or Microsoft Excel. Figures were designed in Adobe Illustrator.

Table 1. List of Reagents for Cell Culture

0.2% Heparin Solution	STEMCELL Technologies	7980
1% N2 supplement (100x)	Thermo Fisher Scientific	17502048
9-cis Retinal	Cayman Chemical Company	21692
alamarBlue	Invitrogen	DAL1100
B27 with Vit A	Thermo Fisher Scientific	17504044
B27 without Vit A	Thermo Fisher Scientific	12587010
Dimethyl Sulfoxide (DMSO) (5x10mL)	VWR	97063-13
DMEM /F12 (1:1) +GlutaMAX	Thermo Fisher Scientific	10565042
DMEM+GlutaMAX	Thermo Fisher Scientific	10566024
DPBS	Thermo Fisher Scientific	14040133
FBS (Fetal Bovine Serum)	ATLAS Biological	EF-0500-A
L-Glutamine 200mM	Gibco	25030-081
hBMP4 (Human recombinant BMP4)	R&D Systems	314-BP-050
Hypure Cell Culture Grade Water (H2O)	VWR	SH30529.02 16750-098
Matirgel	Corning	354277
MEM NEAA (100x)	Thermo Fisher Scientific	11140050
mTeSR+	STEMCELL Technologies	5825
Penicillin – Streptomycin	Cytvia	J210040
Poly-L-lysine solution	Sigma-Aldrich	P4707-50ML
Rock inhibitor (RI) Y-27632	Fisher Scientific	12-541-0
Synth-a- Freeze	gibco	A1254201
Taurine (≥99%)	Sigma-Aldrich	T0625-10
TrypLE	Thermo Fisher Scientific	12563011

Table 2. Media Formulations for Retinal Organoid Differentiation

Media Name	Composition
NIM (Neural Induction Medium)	DMEM /F12 (1:1), 1% N2 supplement, 1x NEAA (MEM Non-Essential Amino Acids Solution), 2ug/mL Heparin
RDM 1 (Retinal Differentiation Medium 1)	DMEM /F12 (3:1), 2%B27 supplement without Vit. A, 1x NEAA, (1% anti-anti)
RDM 2 (Retinal Differentiation Medium 2)	DMEM/F12 (3:1), 2% B27 with Vitamin A, 1x NEAA
RDM 3 (Retinal Differentiation Medium 3)	DMEM/F12 (3:1), 2% B27 with Vitamin A, 1x NEAA, 10% FBS (Fetal Bovine Serum) and 100 uM taurine

Table 3. List of Compounds and Inhibitors

Compound	[Stock] and Vehicle	Final Dilution	Company	Cat. No.	Function
DMSO	N/A	N/A	Fisher	BP231-100	Vehicle
Sterile H20	N/A	N/A	VWR Lifescience	02-0201-0500	Vehicle
4μ8c	50mM in DMSO	50uM	EMD Millipore	412512	IRE1 RNase inhibitor
ISRIB (trans-isomer)	5mM in DMSO	500nM	MedChemExpress	HY-12495	eIF2B stabalizer
Ceapin-A7	5mM in DMSO	6uM	Sigma	40619	ATF6 Inhibitor
HA15	5mM in DMSO	50uM	Fisher	501365915	BiP inhibitor
C16	10mM in DMSO	500nM	ABCAM	Ab144595	PKR inhibitor
IFN-alpha-2b	100 ug/mL (500 IU/uL) in ddH20	500 IU/mL	Enzo	ENZ-PRT	Recombinant active human IFN-alpha-2b
Human IFN-β	10 ug/mL (100 IU/uL) In 0.1% BSA	100 IU/mL	PeproTech	300-02BC-5UG	Recombinant Human IFN-β
Necrostatin 2 Racemate	50mM in DMSO	50 uM	SelleckChem	S7023	Pan-caspase inhibitor
Z-VAD-FMK	50mM in DMSO	50 uM	SelleckChem	S8641	Necrosis Inhibitor
Human AXL Antibody (Goat)	200 ug/mL in PBS	100 ug/mL	R&D Systems	AF154	AXL Function Blocking Antibody
Human Gas6 Antibody (Goat)	200 ug/mL	50-100 ug/mL	R&D Systems	AB885	Gas6 Function Blocking Antibody
Normal Goat IgG Control Antibody	200 ug/mL	100 ug/mL	R&D Systems	AB108-C	Normal Goat IgG Control

Table 4. List of Primary Antibodies Fluorescent Assays

Target	Host	Clonality	Dilution IHC	Company	Cat. No.
ZIKV NS2B	Rabbit	Polyclonal	1:500	GeneTex	GTX133308
ZIKV Envelope Protein	Mouse	Monoclonal	1:500	GeneTex	GTX634155
CHX10/VSX2	Sheep	Polyclonal	1:200	MilliPore	AB9016
Brn3a clone 5A3.2	Mouse	Monoclonal	1:250	SigmaAldrich	MAB1585
J2 dsRNA	Mouse	Monoclonal	1:100	Nordic	10010200
AXL	Rabbit	Monoclonal	1:250	Cell Signaling	8661
Vimentin	Chicken	Polyclonal	1:1000	Millipore	AB5733
GFP	Rabbit	Polyclonal	1:500	Invitrogen	A-11122
Opsin	Mouse	Monoclonal	1:200	SigmaAldrich	04886

Table 5. List of Stains and Secondary Antibodies

Target	Host	Dilution IFA	Concentration IHC	Company	Cat. No.
Hoechst 33342	Stain	1:1000	1:500	Invitrogen	H3570
Propidium Iodide	Stain	N/A	1:1000	Life technologies	P3566
Alexa Fluor® 488 Goat Anti-Mouse IgG (H+L)	Mouse	1:1000	1:500	Invitrogen	A11001
Alexa Fluor® 488 Chicken Anti-Rabbit IgG (H+L)	Rabbit	1:1000	1:500	Invitrogen	A21441
Alexa Fluor® 546 Goat Anti-Mouse IgG (H+L)	Mouse	1:1000	1:500	Invitrogen	A11030
Alexa Fluor® 568 Goat Anti-Rabbit IgG (H+L)	Rabbit	1:1000	1:500	Invitrogen	A11011
Alexa Fluor® 568 Donkey Anti-Sheep IgG (H+L)	Sheep	1:1000	1:500	Invitrogen	A21099
Alexa Fluor® 633 Goat Anti-Rabbit IgG (H+L)	Rabbit	1:1000	1:500	Invitrogen	A21071
Alexa Fluor® 647 Chicken Anti-Mouse IgG (H+L)	Mouse	1:1000	1:500	Invitrogen	A21463

Citations

1. ECDC, S., *Rapid risk assessment: Microcephaly in Brazil potentially linked to the Zika virus epidemic*. 2015.
2. Coelho, K., et al., *Congenital Zika syndrome phenotype in a child born in Brazil in December 2011.* Clin Case Rep, 2018. **6**(11): p. 2053-2056.
3. Krow-Lucal, E.R., B.J. Biggerstaff, and J.E. Staples, *Estimated Incubation Period for Zika Virus Disease.* Emerg Infect Dis, 2017. **23**(5): p. 841-845.
4. Marquezan, M.C., et al., *Ocular effects of Zika virus-a review.* Surv Ophthalmol, 2018. **63**(2): p. 166-173.
5. Arévalo Romero, H., et al., *The Dual Role of the Immune Response in Reproductive Organs During Zika Virus Infection.* Front Immunol, 2019. **10**: p. 1617.
6. Winkler, C.W., et al., *Adaptive Immune Responses to Zika Virus Are Important for Controlling Virus Infection and Preventing Infection in Brain and Testes.* J Immunol, 2017. **198**(9): p. 3526-3535.
7. CDC, *Zika Transmission*, N.C.f.E.a.Z.I.D.N. Center of Disease Control and Prevention, Division of Vector-Borne Diseases (DVBD), Editor. 2019, Center of Disease Control.
8. Lowe, R., et al., *The Zika Virus Epidemic in Brazil: From Discovery to Future Implications.* Int J Environ Res Public Health, 2018. **15**(1).
9. PubMed, *"Zika virus"*, in *1952-2023*. 2024, National Center for Biotechnology Information.
10. PAHO, *Zika suspected and confirmed cases reported by countries and territories in the Americas.* World Health Organization, 2024. **Pan American Health Organization**.
11. CDPH, *CDPH Monthly Update on Number of Zika Virus Infections in California.* California Department of Public Health

Division of Communicable Disease Control, March 1, 2024.

12. CDC, *Zika cases in the United States.* Center for Disease Control and Prevention, 2023. **ArboNET**.
13. Laporta, G.Z., et al., *Global Distribution of Aedes aegypti and Aedes albopictus in a Climate Change Scenario of Regional Rivalry.* Insects, 2023. **14**(1).
14. Haby, M.M., et al., *Prevalence of asymptomatic Zika virus infection: a systematic review.* Bull World Health Organ, 2018. **96**(6): p. 402-413d.
15. Adachi, K. and K. Nielsen-Saines, *Zika clinical updates: implications for pediatrics.* Curr Opin Pediatr, 2018. **30**(1): p. 105-116.
16. Venancio, F.A., et al., *Congenital Zika Syndrome in a Brazil-Paraguay-Bolivia border region: Clinical features of cases diagnosed between 2015 and 2018.* PLoS One, 2019. **14**(10): p. e0223408.
17. Saag, M.S., et al., *High-level viremia in adults and children infected with human immunodeficiency virus: relation to disease stage and CD4+ lymphocyte levels.* J Infect Dis, 1991. **164**(1): p. 72-80.
18. Prendergast, A.J., P. Klenerman, and P.J. Goulder, *The impact of differential antiviral immunity in children and adults.* Nat Rev Immunol, 2012. **12**(9): p. 636-48.

19. Kaler, J., et al., *Respiratory Syncytial Virus: A Comprehensive Review of Transmission, Pathophysiology, and Manifestation.* Cureus, 2023. **15**(3): p. e36342.
20. Zare-Zardini, H., et al., *Coronavirus Disease 2019 (COVID-19) in Children: Prevalence, Diagnosis, Clinical Symptoms, and Treatment.* Int J Gen Med, 2020. **13**: p. 477-482.
21. Ramond, A., et al., *Postnatal symptomatic Zika virus infections in children and adolescents: A systematic review.* PLoS Negl Trop Dis, 2020. **14**(10): p. e0008612.
22. Craig, A.T., et al., *Acute flaccid paralysis incidence and Zika virus surveillance, Pacific Islands.* Bull World Health Organ, 2017. **95**(1): p. 69-75.
23. de Paula Freitas, B., et al., *Zika virus and the eye.* Curr Opin Ophthalmol, 2017. **28**(6): p. 595-599.
24. Ventura, C.V. and L.O. Ventura, *Ophthalmologic Manifestations Associated With Zika Virus Infection.* Pediatrics, 2018. **141**(Suppl 2): p. S161-s166.
25. Salinas, S., et al., *Zika Virus Efficiently Replicates in Human Retinal Epithelium and Disturbs Its Permeability.* J Virol, 2017. **91**(3).
26. Sun, J., et al., *Presence of Zika Virus in Conjunctival Fluid.* JAMA Ophthalmol, 2016. **134**(11): p. 1330-1332.
27. Ventura, L.O., et al., *Visual impairment in children with congenital Zika syndrome.* J aapos, 2017. **21**(4): p. 295-299.e2.
28. Gupta, N. and K. Tripathy, *Retinitis*, in *StatPearls*. 2024, StatPearls Publishing Copyright © 2024, StatPearls Publishing LLC.: Treasure Island (FL).
29. Wang, Y., et al., *The role of apoptosis within the retina of coronavirus-infected mice.* Invest Ophthalmol Vis Sci, 2000. **41**(10): p. 3011-8.
30. Fierz, W., *Age-Related Macular Degeneration: A Connection between Human Herpes Virus-6A-Induced CD46 Downregulation and Complement Activation?* Front Immunol, 2017. **8**: p. 1314.
31. Manangeeswaran, M., et al., *ZIKA virus infection causes persistent chorioretinal lesions.* Emerg Microbes Infect, 2018. **7**(1): p. 96.
32. Croze, R.H. and D.O. Clegg, *Differentiation of pluripotent stem cells into retinal pigmented epithelium.* Dev Ophthalmol, 2014. **53**: p. 81-96.
33. Gely-Rojas, L., et al., *Association of Zika Virus Exposure in Utero with Ocular Phenotypes in a Group of Newborns in Puerto Rico Exposure with ocular phenotypes in newborns in Puerto Rico.* P R Health Sci J, 2018. **37**(Spec Issue): p. S77-s80.
34. Taha, M.J.J., et al., *Ocular manifestations of recent viral pandemics: A literature review.* Front Med (Lausanne), 2022. **9**: p. 1011335.
35. CDC, *Congenital Zika Syndrome & Other Birth Defects*, N.C.f.E.a.Z.I.D.N. Center of Disease Control and Prevention, Division of Vector-Borne Diseases (DVBD), Editor. 2022.
36. Neelam, V., et al., *Outcomes up to age 36 months after congenital Zika virus infection-U.S. states.* Pediatr Res, 2024. **95**(2): p. 558-565.
37. Antoniou, E., et al., *Congenital Zika Syndrome and Disabilities of Feeding and Breastfeeding in Early Childhood: A Systematic Review.* Viruses, 2023. **15**(3).
38. Pomar, L., et al., *Zika virus during pregnancy: From maternal exposure to congenital Zika virus syndrome.* Prenat Diagn, 2019. **39**(6): p. 420-430.

39. Roth, N.M., et al., *Zika-Associated Birth Defects Reported in Pregnancies with Laboratory Evidence of Confirmed or Possible Zika Virus Infection - U.S. Zika Pregnancy and Infant Registry, December 1, 2015-March 31, 2018.* MMWR Morb Mortal Wkly Rep, 2022. **71**(3): p. 73-79.
40. Souza, J.P., et al., *Adverse fetal and neonatal outcomes in pregnancies with confirmed Zika Virus infection in Rio de Janeiro, Brazil: A cohort study.* PLoS Negl Trop Dis, 2021. **15**(1): p. e0008893.
41. Gallo, L.G., et al., *Another piece of the Zika puzzle: assessing the associated factors to microcephaly in a systematic review and meta-analysis.* BMC Public Health, 2020. **20**(1): p. 827.
42. Coelho, A.V.C. and S. Crovella, *Microcephaly Prevalence in Infants Born to Zika Virus-Infected Women: A Systematic Review and Meta-Analysis.* Int J Mol Sci, 2017. **18**(8).
43. Krauer, F., et al., *Zika Virus Infection as a Cause of Congenital Brain Abnormalities and Guillain-Barré Syndrome: Systematic Review.* PLoS Med, 2017. **14**(1): p. e1002203.
44. King, E.L. and N. Irigoyen, *Zika Virus and Neuropathogenesis: The Unanswered Question of Which Strain Is More Prone to Causing Microcephaly and Other Neurological Defects.* Front Cell Neurosci, 2021. **15**: p. 695106.
45. Raeisossadati, R., et al., *Epigenetic regulation of retinal development.* Epigenetics Chromatin, 2021. **14**(1): p. 11.
46. Mannu, G.S., *Retinal phototransduction.* Neurosciences (Riyadh), 2014. **19**(4): p. 275-80.
47. Guevara, J.G. and S. Agarwal-Sinha, *Ocular abnormalities in congenital Zika syndrome: a case report, and review of the literature.* J Med Case Rep, 2018. **12**(1): p. 161.
48. Zin, A.A., et al., *Screening Criteria for Ophthalmic Manifestations of Congenital Zika Virus Infection.* JAMA Pediatr, 2017. **171**(9): p. 847-854.
49. Bhagat, R., G. Kaur, and P. Seth, *Molecular mechanisms of zika virus pathogenesis: An update.* Indian J Med Res, 2021. **154**(3): p. 433-445.
50. Zhao, B., et al., *Structure and function of the Zika virus full-length NS5 protein.* Nat Commun, 2017. **8**: p. 14762.
51. Christian, K.M., H. Song, and G.L. Ming, *Pathophysiology and Mechanisms of Zika Virus Infection in the Nervous System.* Annu Rev Neurosci, 2019. **42**: p. 249-269.
52. Singh, P.K., et al., *Zika virus infects cells lining the blood-retinal barrier and causes chorioretinal atrophy in mouse eyes.* JCI Insight, 2017. **2**(4): p. e92340.
53. Agrelli, A., et al., *ZIKA virus entry mechanisms in human cells.* Infect Genet Evol, 2019. **69**: p. 22-29.
54. Owczarek, K., et al., *Zika virus: mapping and reprogramming the entry.* Cell Commun Signal, 2019. **17**(1): p. 41.
55. Peng, H., et al., *Zika Virus Induces Autophagy in Human Umbilical Vein Endothelial Cells.* Viruses, 2018. **10**(5).
56. Wu, Y., et al., *C19orf66 interrupts Zika virus replication by inducing lysosomal degradation of viral NS3.* PLoS Negl Trop Dis, 2020. **14**(3): p. e0008083.

57. Rodriguez, A.K., et al., *Molecular characteristics and replication mechanism of dengue, zika and chikungunya arboviruses, and their treatments with natural extracts from plants: An updated review.* Excli j, 2019. **18**: p. 988-1006.
58. Sager, G., et al., *Role of Host Cell Secretory Machinery in Zika Virus Life Cycle.* Viruses, 2018. **10**(10).
59. Song, H., et al., *Zika virus NS1 structure reveals diversity of electrostatic surfaces among flaviviruses.* Nat Struct Mol Biol, 2016. **23**(5): p. 456-8.
60. Cortese, M., et al., *Ultrastructural Characterization of Zika Virus Replication Factories.* Cell Rep, 2017. **18**(9): p. 2113-2123.
61. Heinz, F.X. and K. Stiasny, *The Antigenic Structure of Zika Virus and Its Relation to Other Flaviviruses: Implications for Infection and Immunoprophylaxis.* Microbiol Mol Biol Rev, 2017. **81**(1).
62. Kellokumpu, S., *Golgi pH, Ion and Redox Homeostasis: How Much Do They Really Matter?* Front Cell Dev Biol, 2019. **7**: p. 93.
63. Mohd Ropidi, M.I., et al., *Endoplasmic reticulum: a focal point of Zika virus infection.* J Biomed Sci, 2020. **27**(1): p. 27.
64. Kunh, L.o.R.J. *Flaviviruses: Dengue virus, Yellow fever virus, West Nile virus, Zika virus*. [cited 2024 March 31]; Available from: https://www.bio.purdue.edu/lab/kuhn/research.html.
65. Holmes, D., *Reconstructing the retina.* Nature, 2018. **561**(7721): p. S2-s3.
66. Mahabadi, N. and Y. Al Khalili, *Neuroanatomy, Retina*, in *StatPearls*. 2024, StatPearls Publishing
Copyright © 2024, StatPearls Publishing LLC.: Treasure Island (FL).
67. Kaneko, A., *Retinal bipolar cells: their function and morphology.* Trends in Neurosciences, 1983. **6**: p. 219-223.
68. Masland, R.H., *The tasks of amacrine cells.* Vis Neurosci, 2012. **29**(1): p. 3-9.
69. Reichenbach, A. and A. Bringmann, *New functions of Müller cells.* Glia, 2013. **61**(5): p. 651-78.
70. Foltz, L.P. and D.O. Clegg, *Rapid, Directed Differentiation of Retinal Pigment Epithelial Cells from Human Embryonic or Induced Pluripotent Stem Cells.* J Vis Exp, 2017(128).
71. Galan, A., et al., *Neuronal injury external to the retina rapidly activates retinal glia, followed by elevation of markers for cell cycle re-entry and death in retinal ganglion cells.* PLoS One, 2014. **9**(7): p. e101349.
72. Kumar, A., et al., *Muller glia in retinal innate immunity: a perspective on their roles in endophthalmitis.* Crit Rev Immunol, 2013. **33**(2): p. 119-35.
73. Yang, S., S. Qi, and C. Wang, *The role of retinal Müller cells in diabetic retinopathy and related therapeutic advances.* Front Cell Dev Biol, 2022. **10**: p. 1047487.
74. Yang, S., J. Zhou, and D. Li, *Functions and Diseases of the Retinal Pigment Epithelium.* Front Pharmacol, 2021. **12**: p. 727870.
75. Purves D, A.G., Fitzpatrick D, et al.,, *Phototransduction*. Neuroscience. Vol. 2. 2001.
76. Alfano, C., et al., *The Unfolded Protein Response: A Key Player in Zika Virus-Associated Congenital Microcephaly.* Front Cell Neurosci, 2019. **13**: p. 94.
77. Borrell, V., *Recent advances in understanding neocortical development.* F1000Res, 2019. **8**.

78. Mira, H. and J. Morante, *Neurogenesis From Embryo to Adult - Lessons From Flies and Mice.* Front Cell Dev Biol, 2020. **8**: p. 533.
79. Hulme, A.J., et al., *Making neurons, made easy: The use of Neurogenin-2 in neuronal differentiation.* Stem Cell Reports, 2022. **17**(1): p. 14-34.
80. Cvekl, A. and W.L. Wang, *Retinoic acid signaling in mammalian eye development.* Exp Eye Res, 2009. **89**(3): p. 280-91.
81. Fuhrmann, S., *Eye morphogenesis and patterning of the optic vesicle.* Curr Top Dev Biol, 2010. **93**: p. 61-84.
82. Joyal, J.S., M.L. Gantner, and L.E.H. Smith, *Retinal energy demands control vascular supply of the retina in development and disease: The role of neuronal lipid and glucose metabolism.* Prog Retin Eye Res, 2018. **64**: p. 131-156.
83. Quinn, P.M.J. and J. Wijnholds, *Retinogenesis of the Human Fetal Retina: An Apical Polarity Perspective.* Genes (Basel), 2019. **10**(12).
84. Pearson, A.A., *The development of the eyelids. Part I. External features.* J Anat, 1980. **130**(Pt 1): p. 33-42.
85. O'Rahilly, R. and F. Müller, *The development of the neural crest in the human.* J Anat, 2007. **211**(3): p. 335-51.
86. Freddo, T.F. and E. Chaum, *Anatomy of the Eye and Orbit: The Clinical Essentials*. 2017.
87. Kim, H.J., et al., *Comprehensive characterization of fetal and mature retinal cell identity to assess the fidelity of retinal organoids.* Stem Cell Reports, 2023. **18**(1): p. 175-189.
88. Gupta, T., et al., *Mapping the Time Line of Development in Each Layer of Human Foetal Retina.* J Clin Diagn Res, 2016. **10**(3): p. Ac04-7.
89. Ryan, S.J., et al., *Retina*. Vol. 3. 2006: Elsevier.
90. Linger, R.M., et al., *TAM receptor tyrosine kinases: biologic functions, signaling, and potential therapeutic targeting in human cancer.* Adv Cancer Res, 2008. **100**: p. 35-83.
91. Lemke, G., *Biology of the TAM receptors.* Cold Spring Harb Perspect Biol, 2013. **5**(11): p. a009076.
92. Davra, V., et al., *Ligand Activation of TAM Family Receptors-Implications for Tumor Biology and Therapeutic Response.* Cancers (Basel), 2016. **8**(12).
93. Ji, R., et al., *TAM receptors support neural stem cell survival, proliferation and neuronal differentiation.* PLoS One, 2014. **9**(12): p. e115140.
94. Nowakowski, T.J., et al., *Expression Analysis Highlights AXL as a Candidate Zika Virus Entry Receptor in Neural Stem Cells.* Cell Stem Cell, 2016. **18**(5): p. 591-6.
95. Lukowski, S.W., et al., *A single-cell transcriptome atlas of the adult human retina.* Embo j, 2019. **38**(18): p. e100811.
96. Cowan, C.S., et al., *Cell Types of the Human Retina and Its Organoids at Single-Cell Resolution.* Cell, 2020. **182**(6): p. 1623-1640.e34.
97. Murao, N. and H. Nishitoh, *Role of the unfolded protein response in the development of central nervous system.* J Biochem, 2017. **162**(3): p. 155-162.
98. Komarasamy, T.V., et al., *Zika Virus Neuropathogenesis: The Different Brain Cells, Host Factors and Mechanisms Involved.* Front Immunol, 2022. **13**: p. 773191.
99. Li, C., et al., *Zika Virus Disrupts Neural Progenitor Development and Leads to Microcephaly in Mice.* Cell Stem Cell, 2016. **19**(1): p. 120-6.

100. Noguchi, K.K., et al., *Zika Virus Infection in the Developing Mouse Produces Dramatically Different Neuropathology Dependent on Viral Strain.* J Neurosci, 2020. **40**(5): p. 1145-1161.
101. Zhao, Z., et al., *Organoids.* Nat Rev Methods Primers, 2022. **2**.
102. Zhong, X., et al., *Generation of three-dimensional retinal tissue with functional photoreceptors from human iPSCs.* Nat Commun, 2014. **5**: p. 4047.
103. Tresenrider, A., et al., *Single-cell sequencing of individual retinal organoids reveals determinants of cell fate heterogeneity.* bioRxiv, 2023.
104. Krenn, V., et al., *Organoid modeling of Zika and herpes simplex virus 1 infections reveals virus-specific responses leading to microcephaly.* Cell Stem Cell, 2021. **28**(8): p. 1362-1379.e7.
105. Fernando, M., et al., *Differentiation of brain and retinal organoids from confluent cultures of pluripotent stem cells connected by nerve-like axonal projections of optic origin.* Stem Cell Reports, 2022. **17**(6): p. 1476-1492.
106. Ocwieja, K.E., et al., *#33: Single-cell RNA sequencing analysis of Zika virus infection in human stem cell-derived neuroprogenitor cells and cerebral organoids.* Journal of the Pediatric Infectious Diseases Society, 2021. **10**(Supplement_2): p. S11-S12.
107. Depla, J.A., et al., *Human Brain Organoids as Models for Central Nervous System Viral Infection.* Viruses, 2022. **14**(3).
108. Rybak-Wolf, A., et al., *Modelling viral encephalitis caused by herpes simplex virus 1 infection in cerebral organoids.* Nat Microbiol, 2023. **8**(7): p. 1252-1266.
109. D'Aiuto, L., et al., *The Impaired Neurodevelopment of Human Neural Rosettes in HSV-1-Infected Early Brain Organoids.* Cells, 2022. **11**(22).
110. Qian, X., et al., *Brain-Region-Specific Organoids Using Mini-bioreactors for Modeling ZIKV Exposure.* Cell, 2016. **165**(5): p. 1238-1254.
111. Ramani, A., et al., *SARS-CoV-2 targets neurons of 3D human brain organoids.* Embo j, 2020. **39**(20): p. e106230.
112. Krenn, V., L.M. Higa, and P.P. Garcez, *Brain Organoids as a Model to Study Zika Virus and SARS-CoV-2 Infections*, in *Brain Organoid Research*. 2023. p. 173-190.
113. Zhang, X., et al., *Recapitulating influenza virus infection and facilitating antiviral and neuroprotective screening in tractable brain organoids.* Theranostics, 2022. **12**(12): p. 5317-5329.
114. Garcez, P.P., et al., *Zika virus impairs growth in human neurospheres and brain organoids.* Science, 2016. **352**(6287): p. 816-8.
115. Dang, J., et al., *Zika Virus Depletes Neural Progenitors in Human Cerebral Organoids through Activation of the Innate Immune Receptor TLR3.* Cell Stem Cell, 2016. **19**(2): p. 258-265.
116. Zhang, W., et al., *In utero infection of Zika virus leads to abnormal central nervous system development in mice.* Sci Rep, 2019. **9**(1): p. 7298.
117. Rosa-Fernandes, L., et al., *Zika Virus Impairs Neurogenesis and Synaptogenesis Pathways in Human Neural Stem Cells and Neurons.* Front Cell Neurosci, 2019. **13**: p. 64.
118. Tang, H., et al., *Zika Virus Infects Human Cortical Neural Progenitors and Attenuates Their Growth.* Cell Stem Cell, 2016. **18**(5): p. 587-90.

119. Ventura, C.V., et al., *First Locally Acquired Congenital Zika Syndrome Case in the United States: Neonatal Clinical Manifestations.* Ophthalmic Surg Lasers Imaging Retina, 2018. **49**(9): p. e93-e98.
120. Deng, Y.Q., et al., *Intranasal infection and contact transmission of Zika virus in guinea pigs.* Nat Commun, 2017. **8**(1): p. 1648.
121. Siddharthan, V., et al., *Human Polyclonal Antibodies Produced from Transchromosomal Bovine Provides Prophylactic and Therapeutic Protections Against Zika Virus Infection in STAT2 KO Syrian Hamsters.* Viruses, 2019. **11**(2).
122. Adams Waldorf, K.M., et al., *Fetal brain lesions after subcutaneous inoculation of Zika virus in a pregnant nonhuman primate.* Nat Med, 2016. **22**(11): p. 1256-1259.
123. Tongthainan, D., et al., *Seroprevalence of Dengue, Zika, and Chikungunya Viruses in Wild Monkeys in Thailand.* Am J Trop Med Hyg, 2020. **103**(3): p. 1228-1233.
124. Grünert, U. and P.R. Martin, *Cell types and cell circuits in human and non-human primate retina.* Prog Retin Eye Res, 2020: p. 100844.
125. Treuting, P.M., et al., *21 - Special Senses: Eye*, in *Comparative Anatomy and Histology*, P.M. Treuting and S.M. Dintzis, Editors. 2012, Academic Press: San Diego. p. 395-418.
126. FitzGibbon, T., et al., *Analysis of the lateral geniculate nucleus in dichromatic and trichromatic marmosets.* J Comp Neurol, 2015. **523**(13): p. 1948-66.
127. Eldred, K.C. and T.A. Reh, *Human retinal model systems: Strengths, weaknesses, and future directions.* Dev Biol, 2021. **480**: p. 114-122.
128. Simonin, Y., et al., *Zika virus induces strong inflammatory responses and impairs homeostasis and function of the human retinal pigment epithelium.* EBioMedicine, 2019. **39**: p. 315-331.
129. Contreras, D., et al., *Differential Susceptibility of Fetal Retinal Pigment Epithelial Cells, hiPSC- Retinal Stem Cells, and Retinal Organoids to Zika Virus Infection.* Viruses, 2023. **15**(1).
130. Zhao, Z., et al., *Viral Retinopathy in Experimental Models of Zika Infection.* Invest Ophthalmol Vis Sci, 2017. **58**(10): p. 4355–4365.
131. Bringmann, A. and P. Wiedemann, *Müller glial cells in retinal disease.* Ophthalmologica, 2012. **227**(1): p. 1-19.
132. Roach, T. and D.J. Alcendor, *Zika virus infection of cellular components of the blood-retinal barriers: implications for viral associated congenital ocular disease.* J Neuroinflammation, 2017. **14**(1): p. 43.
133. Capiz, D., H.E. Grossniklaus, and S. Yeh, *Pathogenesis of Ocular Findings in Congenital Zika Syndrome.* JAMA Ophthalmol, 2017. **135**(10): p. 1077.
134. Jeon, C.J., E. Strettoi, and R.H. Masland, *The major cell populations of the mouse retina.* J Neurosci, 1998. **18**(21): p. 8936-46.
135. Mustafi, D., A.H. Engel, and K. Palczewski, *Structure of cone photoreceptors.* Prog Retin Eye Res, 2009. **28**(4): p. 289-302.
136. Hussey, K.A., S.E. Hadyniak, and R.J. Johnston, Jr., *Patterning and Development of Photoreceptors in the Human Retina.* Front Cell Dev Biol, 2022. **10**: p. 878350.
137. Capowski, E.E., et al., *Reproducibility and staging of 3D human retinal organoids across multiple pluripotent stem cell lines.* Development, 2019. **146**(1).

138. Völkner, M., et al., *Optimized Adeno-Associated Virus Vectors for Efficient Transduction of Human Retinal Organoids.* Hum Gene Ther, 2021. **32**(13-14): p. 694-706.
139. Menuchin-Lasowski, Y., et al., *SARS-CoV-2 infects and replicates in photoreceptor and retinal ganglion cells of human retinal organoids.* Stem Cell Reports, 2022. **17**(4): p. 789-803.
140. Sridhar, A., et al., *Single-Cell Transcriptomic Comparison of Human Fetal Retina, hPSC-Derived Retinal Organoids, and Long-Term Retinal Cultures.* Cell Rep, 2020. **30**(5): p. 1644-1659.e4.
141. Zanini, F., et al., *Single-cell transcriptional dynamics of flavivirus infection.* Elife, 2018. **7**.
142. Rato, S., et al., *Exploring viral infection using single-cell sequencing.* Virus Res, 2017. **239**: p. 55-68.
143. Wang, H., et al., *Single-Cell Analysis of Foot-and-Mouth Disease Virus.* Front Microbiol, 2020. **11**: p. 361.
144. Fang, L., et al., *A Simple Cloning-free Method to Efficiently Induce Gene Expression Using CRISPR/Cas9.* Mol Ther Nucleic Acids, 2019. **14**: p. 184-191.
145. Yin, Y., et al., *Single-Cell Sequencing and Organoids: A Powerful Combination for Modelling Organ Development and Diseases.* Rev Physiol Biochem Pharmacol, 2021. **179**: p. 189-210.
146. Uzquiano, A., et al., *Single-cell multiomics atlas of organoid development uncovers longitudinal molecular programs of cellular diversification of the human cerebral cortex.* bioRxiv, 2022: p. 2022.03.17.484798.
147. Liang, Q., et al., *A multi-omics atlas of the human retina at single-cell resolution.* Cell Genom, 2023. **3**(6): p. 100298.
148. Collin, J., et al., *Deconstructing Retinal Organoids: Single Cell RNA-Seq Reveals the Cellular Components of Human Pluripotent Stem Cell-Derived Retina.* Stem Cells, 2019. **37**(5): p. 593-598.
149. Saleh, D., S.N.S. Yarrarapu, and S. Sharma, *Herpes Simplex Type 1*, in *StatPearls*. 2024, StatPearls Publishing
Copyright © 2024, StatPearls Publishing LLC.: Treasure Island (FL).
150. Medicine, J.s.H., *Herpes: HSV-1 and HSV-2 Overview*, J.s.H. Medicine, Editor.
151. WHO, G., *Globally, an estimated two-thirds of the population under 50 are infected with herpes simplex virus type 1*. 2015, World Health Organization.
152. Bagga, B., et al., *Herpes simplex infection of the eye: an introduction.* Community Eye Health, 2020. **33**(108): p. 68-70.
153. UK, N., *Herpes simplex eye infections*, N.H.S.U. Kingdom, Editor. 2023.
154. Hoogewoud, F., et al., *Acute retinal necrosis: A mini review.* Frontiers in Ophthalmology, 2022. **2**.
155. Zhong, P., et al., *Herpes simplex virus type 1 related acute retinal necrosis following an encephalitis illness: a case report.* BMC Neurol, 2021. **21**(1): p. 49.
156. Bergstrom, R. and K. Tripathy, *Acute Retinal Necrosis*, in *StatPearls*. 2024, StatPearls Publishing
Copyright © 2024, StatPearls Publishing LLC.: Treasure Island (FL).

157. Fan, S., et al., *Type I Interferon Signaling Is Critical During the Innate Immune Response to HSV-1 Retinal Infection.* Invest Ophthalmol Vis Sci, 2022. **63**(13): p. 28.
158. Banfield, B.W., et al., *A chicken embryo eye model for the analysis of alphaherpesvirus neuronal spread and virulence.* J Virol, 1998. **72**(6): p. 4580-8.
159. Aralis, Z., *PhD Thesis: SARS-CoV-2 Pandemic Diagnotics and HSV1 in Retinal Organoids *currently unpublished.* Open Access Disserations, 2024.
160. Strange, D.P., et al., *Axl Promotes Zika Virus Entry and Modulates the Antiviral State of Human Sertoli Cells.* mBio, 2019. **10**(4).
161. Akhtar, T., et al., *Accelerated photoreceptor differentiation of hiPSC-derived retinal organoids by contact co-culture with retinal pigment epithelium.* Stem Cell Res, 2019. **39**: p. 101491.
162. Zhang, Y., et al., *Host cytoskeletal vimentin serves as a structural organizer and an RNA-binding protein regulator to facilitate Zika viral replication.* Proc Natl Acad Sci U S A, 2022. **119**(8).
163. Wells, M.F., et al., *Genetic Ablation of AXL Does Not Protect Human Neural Progenitor Cells and Cerebral Organoids from Zika Virus Infection.* Cell Stem Cell, 2016. **19**(6): p. 703-708.
164. Chen, S., et al., *Synergistic Utilization of Necrostatin-1 and Z-VAD-FMK Efficiently Promotes the Survival of Compression-Induced Nucleus Pulposus Cells via Alleviating Mitochondrial Dysfunction.* Biomed Res Int, 2020. **2020**: p. 6976317.
165. 10xGenomics, *Chromium Single Cell 5' Reagent Kits User Guide (v2 Chemistry Dual Index).* 2022.
166. Waickman, A.T., et al., *Temporally integrated single cell RNA sequencing analysis of PBMC from experimental and natural primary human DENV-1 infections.* PLoS Pathog, 2021. **17**(1): p. e1009240.
167. Sanborn, M.A., et al., *Analysis of cell-associated DENV RNA by oligo(dT) primed 5' capture scRNAseq.* Sci Rep, 2020. **10**(1): p. 9047.
168. Zhou, Y., et al., *Metascape provides a biologist-oriented resource for the analysis of systems-level datasets.* Nat Commun, 2019. **10**(1): p. 1523.
169. Wise, E.L., J. Samolej, and G. Elliott, *Herpes Simplex Virus 1 Expressing GFP-Tagged Virion Host Shutoff (vhs) Protein Uncouples the Activities of RNA Degradation and Differential Nuclear Retention of the Virus Transcriptome.* J Virol, 2022. **96**(14): p. e0192621.
170. Harkness, J.M., M. Kader, and N.A. DeLuca, *Transcription of the herpes simplex virus 1 genome during productive and quiescent infection of neuronal and nonneuronal cells.* J Virol, 2014. **88**(12): p. 6847-61.
171. Straface, G., et al., *Herpes simplex virus infection in pregnancy.* Infect Dis Obstet Gynecol, 2012. **2012**: p. 385697.
172. Dauber, B., J. Pelletier, and J.R. Smiley, *The herpes simplex virus 1 vhs protein enhances translation of viral true late mRNAs and virus production in a cell type-dependent manner.* J Virol, 2011. **85**(11): p. 5363-73.
173. Hernandez, S., et al., *Challenges and Opportunities for Immunoprofiling Using a Spatial High-Plex Technology: The NanoString GeoMx(®) Digital Spatial Profiler.* Front Oncol, 2022. **12**: p. 890410.

174. Kishi, J.Y., et al., *Light-Seq: light-directed in situ barcoding of biomolecules in fixed cells and tissues for spatially indexed sequencing.* Nat Methods, 2022. **19**(11): p. 1393-1402.
175. Delorey, T.M., et al., *COVID-19 tissue atlases reveal SARS-CoV-2 pathology and cellular targets.* Nature, 2021. **595**(7865): p. 107-113.
176. Wright, M.T. and L. Plate, *Revealing functional insights into ER proteostasis through proteomics and interactomics.* Exp Cell Res, 2021. **399**(1): p. 112417.
177. McLaughlin, T., et al., *Cellular stress signaling and the unfolded protein response in retinal degeneration: mechanisms and therapeutic implications.* Mol Neurodegener, 2022. **17**(1): p. 25.
178. Schwarz, D.S. and M.D. Blower, *The endoplasmic reticulum: structure, function and response to cellular signaling.* Cell Mol Life Sci, 2016. **73**(1): p. 79-94.
179. Walter, P. and D. Ron, *The unfolded protein response: from stress pathway to homeostatic regulation.* Science, 2011. **334**(6059): p. 1081-6.
180. Karagöz, G.E., D. Acosta-Alvear, and P. Walter, *The Unfolded Protein Response: Detecting and Responding to Fluctuations in the Protein-Folding Capacity of the Endoplasmic Reticulum.* Cold Spring Harb Perspect Biol, 2019. **11**(9).
181. Zappa, F., et al., *Signaling by the integrated stress response kinase PKR is fine-tuned by dynamic clustering.* J Cell Biol, 2022. **221**(7).
182. Lewy, T.G., J.M. Grabowski, and M.E. Bloom, *BiP: Master Regulator of the Unfolded Protein Response and Crucial Factor in Flavivirus Biology*. Yale J Biol Med, 2017. **90**(2): p. 291-300.
183. Mufrrih, M., B. Chen, and S.W. Chan, *Zika Virus Induces an Atypical Tripartite Unfolded Protein Response with Sustained Sensor and Transient Effector Activation and a Blunted BiP Response.* mSphere, 2021. **6**(3): p. e0036121.
184. Tan, Z., et al., *ZIKV infection activates the IRE1-XBP1 and ATF6 pathways of unfolded protein response in neural cells.* J Neuroinflammation, 2018. **15**(1): p. 275.
185. Gladwyn-Ng, I., et al., *Stress-induced unfolded protein response contributes to Zika virus-associated microcephaly.* Nat Neurosci, 2018. **21**(1): p. 63-71.
186. Firtina, Z. and M.K. Duncan, *Unfolded Protein Response (UPR) is activated during normal lens development.* Gene Expr Patterns, 2011. **11**(1-2): p. 135-43.
187. Bond, S., et al., *The Integrated Stress Response and Phosphorylated Eukaryotic Initiation Factor 2α in Neurodegeneration.* J Neuropathol Exp Neurol, 2020. **79**(2): p. 123-143.
188. Crespillo-Casado, A., et al., *PPP1R15A-mediated dephosphorylation of eIF2α is unaffected by Sephin1 or Guanabenz.* Elife, 2017. **6**.
189. Hayashi, A., et al., *The role of brain-derived neurotrophic factor (BDNF)-induced XBP1 splicing during brain development.* J Biol Chem, 2007. **282**(47): p. 34525-34.
190. Söderpalm, A.K., et al., *Retinoic acid produces rod photoreceptor selective apoptosis in developing mammalian retina.* Invest Ophthalmol Vis Sci, 2000. **41**(3): p. 937-47.
191. Yang, J., et al., *UPR Activation and the Down-Regulation of α-Crystallin in Human High Myopia-Related Cataract Lens Epithelium.* PLoS One, 2015. **10**(9): p. e0137582.
192. Kondo, S., et al., *Activation of OASIS family, ER stress transducers, is dependent on its stabilization.* Cell Death Differ, 2012. **19**(12): p. 1939-49.

193. Chiang, W.J., et al., *Pathomechanisms of ATF6-Associated Cone Photoreceptor Diseases.* Adv Exp Med Biol, 2019. **1185**: p. 305-310.
194. Miyagi, H., et al., *Transcriptional regulation of VEGFA by the endoplasmic reticulum stress transducer OASIS in ARPE-19 cells.* PLoS One, 2013. **8**(1): p. e55155.
195. Xu, P., et al., *Role of microglia in the dissemination of Zika virus from mother to fetal brain.* PLoS Negl Trop Dis, 2020. **14**(7): p. e0008413.
196. Li, Y., et al., *Zika virus induces neuronal and vascular degeneration in developing mouse retina.* Acta Neuropathol Commun, 2021. **9**(1): p. 97.
197. Willoughby, C.E., et al., *Anatomy and physiology of the human eye: effects of mucopolysaccharidoses disease on structure and function – a review.* Clinical & Experimental Ophthalmology, 2010. **38**(s1): p. 2-11.
198. Mesnard, C., et al., *Ocular manifestations in Congenital Zika syndrome: About a case of torpedo maculopathy.* Am J Ophthalmol Case Rep, 2020. **18**: p. 100626.
199. Mulfaul, K., et al., *Stepwise differentiation and functional characterization of human induced pluripotent stem cell-derived choroidal endothelial cells.* Stem Cell Res Ther, 2020. **11**(1): p. 409.
200. Hillary, R.F. and U. FitzGerald, *A lifetime of stress: ATF6 in development and homeostasis.* J Biomed Sci, 2018. **25**(1): p. 48.
201. Labib, B.A. and D.I. Chigbu, *Pathogenesis and Manifestations of Zika Virus-Associated Ocular Diseases.* Trop Med Infect Dis, 2022. **7**(6).
202. Marneros, A.G., et al., *Vascular endothelial growth factor expression in the retinal pigment epithelium is essential for choriocapillaris development and visual function.* Am J Pathol, 2005. **167**(5): p. 1451-9.
203. Schultz, V., et al., *Zika Virus Infection Leads to Demyelination and Axonal Injury in Mature CNS Cultures.* Viruses, 2021. **13**(1).
204. Magoon, E.H. and R.M. Robb, *Development of Myelin in Human Optic Nerve and Tract: A Light and Electron Microscopic Study.* Archives of Ophthalmology, 1981. **99**(4): p. 655-659.
205. Hernandez-Moreno, L., et al., *Absent Foveal Pit, Also Known as Fovea Plana, in a Child without Associated Ocular or Systemic Findings.* Case Rep Ophthalmol Med, 2018. **2018**: p. 2146826.
206. Skorczyk-Werner, A., et al., *Autosomal recessive cone-rod dystrophy can be caused by mutations in the ATF6 gene.* Eur J Hum Genet, 2017. **25**(11): p. 1210-1216.
207. Allen, E.H., et al., *Keratin 12 missense mutation induces the unfolded protein response and apoptosis in Meesmann epithelial corneal dystrophy.* Hum Mol Genet, 2016. **25**(6): p. 1176-91.
208. de Oliveira, D.R., et al., *Glaucoma Workup in Congenital Zika Syndrome.* J Glaucoma, 2019. **28**(4): p. 313-317.
209. Miner, J.J., et al., *Zika Virus Infection in Mice Causes Panuveitis with Shedding of Virus in Tears.* Cell Rep, 2016. **16**(12): p. 3208-3218.
210. Joseph, R., et al., *Lens epithelial cells-induced pluripotent stem cells as a model to study epithelial-mesenchymal transition during posterior capsular opacification.* Biochem Biophys Rep, 2019. **20**: p. 100696.
211. Solley, S.C., *Roles of the Unfolded Protein Response in the Mammalian Cell Cycle.* UC Santa Barbara Electronic Theses and Dissertations, 2020.

212. da Silva, M.H.M., et al., *Innate immune response in patients with acute Zika virus infection.* Med Microbiol Immunol, 2019. **208**(6): p. 703-714.
213. Alberts B, J.A., Lewis J, et al., *Innate Immunity*. Molecular Biology of the Cell. Vol. 4th edition. 2002, New York: Garland Science.
214. Skapenko, A., et al., *The role of the T cell in autoimmune inflammation.* Arthritis Res Ther, 2005. **7 Suppl 2**(Suppl 2): p. S4-14.
215. Ngono, A.E. and S. Shresta, *Immune Response to Dengue and Zika.* Annu Rev Immunol, 2018. **36**: p. 279-308.
216. Paulis, A. and E. Tramontano, *Unlocking STING as a Therapeutic Antiviral Strategy.* Int J Mol Sci, 2023. **24**(8).
217. Ren, Z., et al., *Regulation of MAVS Expression and Signaling Function in the Antiviral Innate Immune Response.* Front Immunol, 2020. **11**: p. 1030.
218. Ezeonwumelu, I.J., E. Garcia-Vidal, and E. Ballana, *JAK-STAT Pathway: A Novel Target to Tackle Viral Infections.* Viruses, 2021. **13**(12).
219. Cesaro, T. and T. Michiels, *Inhibition of PKR by Viruses.* Front Microbiol, 2021. **12**: p. 757238.
220. Sajid, M., et al., *The Functional and Antiviral Activity of Interferon Alpha-Inducible IFI6 Against Hepatitis B Virus Replication and Gene Expression.* Front Immunol, 2021. **12**: p. 634937.
221. Villamayor, L., et al., *Interferon alpha inducible protein 6 is a negative regulator of innate immune responses by modulating RIG-I activation.* Front Immunol, 2023. **14**: p. 1105309.
222. Richardson, R.B., et al., *A CRISPR screen identifies IFI6 as an ER-resident interferon effector that blocks flavivirus replication.* Nat Microbiol, 2018. **3**(11): p. 1214-1223.
223. Qin, L., et al., *Swine IFI6 confers antiviral effects against Japanese encephalitis virus in vitro and in vivo.* J Gen Virol, 2023. **104**(4).
224. Zhang, M., et al., *ISGylation in Innate Antiviral Immunity and Pathogen Defense Responses: A Review.* Front Cell Dev Biol, 2021. **9**: p. 788410.
225. Freitas, B.T., et al., *How ISG15 combats viral infection.* Virus Res, 2020. **286**: p. 198036.
226. Lenschow, D.J., et al., *IFN-stimulated gene 15 functions as a critical antiviral molecule against influenza, herpes, and Sindbis viruses.* Proc Natl Acad Sci U S A, 2007. **104**(4): p. 1371-6.
227. Moore, K.M., et al., *Single-cell analysis reveals an antiviral network that controls Zika virus infection in human dendritic cells.* J Virol, 2024: p. e0019424.
228. Caine, E.A., et al., *Interferon lambda protects the female reproductive tract against Zika virus infection.* Nat Commun, 2019. **10**(1): p. 280.
229. Miner, J.J., et al., *HSV-1 and Zika Virus but Not SARS-CoV-2 Replicate in the Human Cornea and Are Restricted by Corneal Type III Interferon.* Cell Rep, 2020. **33**(5): p. 108339.
230. Singh, P.K., et al., *Interferon-stimulated gene 15 (ISG15) restricts Zika virus replication in primary human corneal epithelial cells.* Ocul Surf, 2019. **17**(3): p. 551-559.

231. Chen, L., et al., *ISG15, a ubiquitin-like interferon-stimulated gene, promotes hepatitis C virus production in vitro: implications for chronic infection and response to treatment.* J Gen Virol, 2010. **91**(Pt 2): p. 382-8.
232. Broering, R., et al., *The interferon stimulated gene 15 functions as a proviral factor for the hepatitis C virus and as a regulator of the IFN response.* Gut, 2010. **59**(8): p. 1111-9.
233. Chen, Y., et al., *Engineering Human Stem Cell Lines with Inducible Gene Knockout using CRISPR/Cas9.* Cell Stem Cell, 2015. **17**(2): p. 233-44.
234. Wang, Y., et al., *Interferon stimulated gene 15 promotes Zika virus replication through regulating Jak/STAT and ISGylation pathways.* Virus Res, 2020. **287**: p. 198087.
235. Scutigliani, E.M. and M. Kikkert, *Interaction of the innate immune system with positive-strand RNA virus replication organelles.* Cytokine Growth Factor Rev, 2017. **37**: p. 17-27.
236. Ricciardi-Jorge, T., et al., *PKR-mediated stress response enhances dengue and Zika virus replication.* mBio, 2023. **14**(5): p. e0093423.
237. Lamers, M.M., B.G. van den Hoogen, and B.L. Haagmans, *ADAR1: "Editor-in-Chief" of Cytoplasmic Innate Immunity.* Front Immunol, 2019. **10**: p. 1763.
238. Zhou, S., et al., *Double-stranded RNA deaminase ADAR1 promotes the Zika virus replication by inhibiting the activation of protein kinase PKR.* J Biol Chem, 2019. **294**(48): p. 18168-18180.
239. Pfaller, C.K., et al., *Protein kinase PKR and RNA adenosine deaminase ADAR1: new roles for old players as modulators of the interferon response.* Curr Opin Immunol, 2011. **23**(5): p. 573-82.
240. Krey, K., A.W. Babnis, and A. Pichlmair, *System-Based Approaches to Delineate the Antiviral Innate Immune Landscape.* Viruses, 2020. **12**(10).
241. Neumann, G. and Y. Kawaoka, *Which Virus Will Cause the Next Pandemic?* Viruses, 2023. **15**(1).
242. Fligor, C.M., et al., *Extension of retinofugal projections in an assembled model of human pluripotent stem cell-derived organoids.* Stem Cell Reports, 2021. **16**(9): p. 2228-2241.
243. Koh, I. and M. Hagiwara, *Modular tissue-in-a-CUBE platform to model blood-brain barrier (BBB) and brain interaction.* Commun Biol, 2024. **7**(1): p. 177.
244. Foster, J.W., K.J. Wahlin, and S. Chakravarti, *A Guide to the Development of Human CorneaOrganoids from Induced Pluripotent Stem Cells in Culture.* Methods Mol Biol, 2020. **2145**: p. 51-58.
245. Guttikonda, S.R., et al., *Fully defined human pluripotent stem cell-derived microglia and tri-culture system model C3 production in Alzheimer's disease.* Nat Neurosci, 2021. **24**(3): p. 343-354.
246. Croze, R.H., et al., *ROCK Inhibition Extends Passage of Pluripotent Stem Cell-Derived Retinal Pigmented Epithelium.* Stem Cells Transl Med, 2014. **3**(9): p. 1066-78.